Editorial corner – a personal view

Water glass – an alternative precursor for sol-gel derived silica nanofiller in polymer composites?

*J. Karger-Kocsis**

MTA–BME Research Group for Composite Science and Technology and Department of Polymer Engineering, Faculty of Mechanical Engineering, Budapest University of Technology and Economics, Műegyetem rkp. 3., H-1111 Bp., Hungary

Nowadays silica containing polymer nanocomposites are preferentially produced by the sol-gel route. This implies the conversion of suitable precursors, notably alkoxysilane derivatives, to silica nanoparticles through subsequent hydrolysis and polycondensation reactions. This organosilane based sol-gel chemistry is widely practiced to produce nanoscale dispersed silica particles in thermoplastics, thermoset resins and rubbers.

Unlike using preformed silica nanoparticles as fillers, their in situ generation via this bottom-up sol-gel synthesis is not associated with health risk. On the other hand, this is quite costly procedure as the alkoxysilane precursors are highly priced fine chemicals.

Is there any chance to use a cheaper precursor? Possibly, yes, one potential candidate is namely water glass. Water glass is the common name for water soluble silicate compounds which have been known and used for centuries. The alkaline and neutral solutions of water glass products are stable. In acidic solution, however, the different alkali silicates form (poly)silicic acids which may undergo polycondensation resulting in silica nanoparticles. Accordingly, the 'roasting', 'silicification' of water glass follow a sol-gel scheme and may result in the desired nanoscale silica. This has been explored already for some polymer nanocomposites, such as polyethylene (DOI: 10.1002/polb.10391), polymethyl methacrylate (DOI: 10.1002/pat.1226) and phenolic resin (DOI: 10.1002/app.29770). Organosilane may be dosed additionally to improve the interfacial adhesion between the matrix (polyamide) and the silica (DOI: 10.1002/pi.1520).

Water glass can be turned into silica particles whereby avoiding the (poly)silicic acid formation. This may happen upon reaction of water glass with carbon dioxide which can be formed also in situ, for example through the reaction between isocyanate and water. This reaction is exploited in various polyurea-based thermosets produced from polyisocyanate/water glass combinations in presence of suitable emulsifiers which may be coreactive compounds, as well (DOI:10.1016/j.eurpolymj.2007.01.010; DOI 10.1007/s10853-009-4145-9). Note that the inevitable byproducts of this chemical pathway are inorganic carbonates.

Polymer nanocomposites are often referred to as inorganic/organic systems. Though water glass is a rather complex, not well defined system, it may meet the role of silica precursor in several applications. One just has to acquire the necessary knowledge from inorganic chemists and learn how to make use of water glass for this purpose. Trials with water glass may open a new horizon for the production of polymer nanocomposites, and especially for thermoset resin-based ones. So, why not to start with exploratory experiments?

Prof. Dr. Dr. h.c. József Karger-Kocsis
Editor-in-Chief

*Corresponding author, e-mail: karger@pt.bme.hu

Role of surfactant molecular weight on morphology and properties of functionalized graphite oxide filled polypropylene nanocomposites

Y. Wang[*]*, J-C. Wang, S-Z. Chen*

Department of Chemical and Materials Engineering Tunghai University, 407 Taichung, Taiwan, Republic of China

Abstract. Various surfactants of different molecular weights, including alkylamine, poly(oxypropylene) diamine (POP), and maleic anhydride grafted polypropylene (PPgMA) oligomers, were used for simultaneous funtionalization and reduction of graphite oxide (fGO). In this study, the effect of molecular weight and compatibility of the surfactants on the morphology and properties of the nanocomposites are reported. Wide-angle X-ray diffraction (WAXD) exhibited a definite interlayer thickness for GOA (alkylamine intercalated GO), however, the diffraction peaks were nearly suppressed for fGOs combining ODA with either POP (GOAP) or PPgMA (GOAE). The uniform dispersion of the fGO flakes in the polypropylene matrix resulted in the significant increase in both the degradation temperature and the crystallization temperature. A single characteristic melting peak of monoclinic (α) crystalline phase was observed from DSC traces, which was consistent with WAXD results. Dynamic mechanical analysis clearly indicated increase in both the storage modulus and the glass transition temperature of the nanocomposites due to the enhanced affinity between fGO and the polypropylene matrix. However, GOAP composite showed lower E' and T_g than GOAE because POP is less compatible with the matrix than PPgMA oligomer. Dielectric analysis also showed significant increase in both dielectric permittivity and dielectric loss at low frequency regimes with GOAE showing maximum dielectric properties. The finely dispersed GOAE and its compatibility with polymer matrix manifested the interfacial polarization, which gave rise to much greater ε' and ε'' than other nanocomposites.

Keywords: nanocomposites, maleated polypropylene, graphite oxide, functionalization

1. Introduction

Conductive polymer composites have aroused wide interests from both academia and industry in the field of functional materials. Addition of diverse conducting fillers such as carbon black [1, 2], graphite [3], and metal fiber or powder [4] into thermoplastic polymers through melt mixing is an effective approach to fabricate conductive composites. Because a great amount of the fillers, generally greater than 15 wt% [5], were required for the host polymer to become conductive, resulting in both poor processability and inferior mechanical properties, the practical applications of these conventional composites were largely restricted. On the other hand, commercial exploitation of isotactic polypropylene has been expanded rapidly due to its attractive characters of low cost, low weight, heat distortion above 100°C, and extraordinary versatility in terms of properties, applications and recycling. The introduction of nanoscopic fillers of high anisotropy enhances a wide range of performance of the polypropylene nanocomposites, such as mechanical, thermal and conductive properties, at a relatively small loading [6].

Graphite is a layered mineral composed of weakly bonded graphene sheets with a large aspect ratio.

Traditionally, oxidation of the graphite yields expandable graphite oxide (GO), which is able to be ultrasonically exfoliated in an aqueous solution or polar solvents. As demonstrated recently by various research groups [7–10], exfoliated graphite nanoplatelets, which combine the lower price and layered structure of clays with the superior thermal and electrical properties of carbon nanotubes, can be an effective alternative to both nanoclays and nanotubes. The straightforward and easily upscalable liquid-phase exfoliation of GO under mild temperatures offers a practical way to large scale graphene production [11]. While delamination of GO in aqueous media is well characterized [12], the dispersion of GO in organic solvents has not been well explored. Only with organically intercalated GO, is it possible to form monolayer colloidal dispersion in organic solvents, which would help in the preparation of GO composites with polymer species that are insoluble in water. Furthermore, the plentiful oxygen-containing groups on GO provide active sites for chemical modification of GO surface [13–17]. Chemicals with long alkyl chains [13, 16, 18–21], such as octadecylamine (ODA), have been used to make hydrophilic GO hydrophobic. It is clear that ODA was mainly used as a surface modifier to improve the dispersion of GO in non-polar polymers; however, to improve the electrical conductivity of ODA-functionalized GO (GOA), chemical reduction agents, such as hydrazine and hydroquinone, were often incorporated.

Note that GO is an electrically insulating material, and the reduction of GO is necessary for restoring the electrical conductivity of the parent graphite [22, 23]. Indeed we have demonstrated an efficient approach through ultrasonication for fast functionalizion and *in situ* reduction of GO with ODA without the addition of conventional chemical reducing agents [24]. The polypropylene nanocomposites filled with GOA exhibited a sharp transition from insulating to conducting with a low percolation threshold at ca. 0.2 vol.% (GOA).

Past research focused primarily on the GO intercalation with various amino acids or series of primary amines [20, 25, 26]. Multiple amines such as alkyl diamine and triamine are also effective intercalating agents [14, 27]. In all cases, there is a systematic increment of the basal spacing, which can only achieve the maximum spacing of around 3 nm with a chain length of C_{18} (ODA), compared to 0.8 nm of the parent GO. Briefly speaking, the low-molecular-weight surfactants are inadequate for dispersing the layered materials into most polymers [28]. On the other hand, high-molecular weight oligomeric intercalants are seldom used for GO functionalization. ODA functionalized GO has been successfully dispersed in polyethylene glycol oligomer of 4000 DA, and the obtained nanocomposites showed markedly improved properties [29]. Unfortunately PEG is water soluble and incompatible with non-polar polypropylene. Thus a dual-functional surfactant with hydrophobic backbone and telechelic amines would be an ideal molecular architecture needed to intercalate GO with interlayer enlargement. Here we shall reveal the preparation of layered GO with much greater *d* spacing by incorporating telechelic POP-diamine of Jeffamine® amines, which had been successfully used in enlarging silicate interlayer spacing [30].

Despite great stride made for the incorporation of GO into polar polymer matrices [22, 23, 31], the nonpolar matrices such as polypropylene (PP) and polyethylene (PE) still pose a significant challenge to achieve homogenous and stable dispersion of graphene [32, 33]. Though the effective dispersion of graphene throughout the polymer matrix is critical in order to take full advantage of the unique properties of graphene-based nanocomposites, predominant graphene aggregations is common in polyolefins because they tend to interact poorly with graphene-structured materials due to low interaction energy between them.

In addition, the melt blending technique is widely used for the preparation of graphene/PP composites [34–37]. However, a generally poor dispersion of graphene and a risk of degradation of the polymer matrix often result from melt blending. An alternative to prepare nanoscale dispersed graphene/PP composites via *in-situ* Ziegler-Natta polymerization in the presence of graphene supported catalyst has been reported [38], but its industrial application is limited by the requirement of sophisticated polymerization techniques. The graphene/PP composites with good filler dispersion can also be prepared through a solution mixing manner [39–41]. In most studies, PPgMA was used either as the matrix polymer [24, 42] or as the compatibilizer for PP/functionalized graphite oxide (fGO) nanocomposites [39, 41]. But the effect of the molecular weight of PPgMA was rarely discussed, and it is apparent that

a timely study is needed. A commercial PPgMA of low molecular weight and high grafting degree is used in this work. It will be shown that the combination of low molecular weight PPgMA with ODA greatly improve the dispersion and the properties of the PPgMA/GO nanocomposites.

In view of the success of the layered nanocomposites of POP-diamine and PPgMA modified clay [30, 43] or graphite [44, 45], we attempted in this study to prepare the conducting polypropylene nanocomposites of ODA intercalated graphite oxide in combination with the two different types of oligomers via solution blending. The goal of this research is to explore the effect of surfactant molecular weight on the thermal, mechanical, and conductive properties, of the nanocomposites. The present study serves two simultaneous purposes of accommodating graphene sheets at the molecular level and furnishing the highly desirable interfacial bonding with the nonpolar matrix. High degree of dispersion means higher area per volume and better bonding means efficient use of filler presence in the matrix to improve composite properties. Direct impact of higher quality dispersion and interfacial bonding on the mechanical and conductive properties are shown to be greatly enhanced by surfactant combinations compared to single ODA surfactant. The results presented here are thermal and mechanical properties from both differential scanning calorimetry (DSC) and dynamical mechanical analysis (DMA). The dielectric properties and the electric conductivity are studied with a dielectric analyzer (DEA).

2. Experimental
2.1. Materials
Maleated polypropylene (PB3150, Chemtru USA), abbreviated as PB, M_w = 330 000 as the polymer matrix. Surfaced Enhanced Flake Graphite (FG, 3775, Asbury USA). 90% octadecylamine (ODA, Acros USA), poly(propylene glycol) bis (2-aminopropyl ether) under the trade name Jeffamine® amines with number average molecular weight of 4000 (POP4000, Huntsman USA), and maleated polypropylene, M_w = 9100 (E43, Eastman USA) as GO modifiers. Certified 99.8% p-xylene (Tedia, USA), sulfuric acid synthesis grade (Scharlau Spain), potassium permanganate regent grade (Showa Japan), and hydrogen peroxide regent grade (Showa Japan) were used as received. All aqueous solutions

were prepared in deionized water obtained by purification with a Sartorius Arium 611 system.

2.2. Chemical oxidation of graphite
The method due to Hummers and Offeman [19] was adopted to prepare graphite oxide (GO) from graphite flakes through chemical oxidation [20] in the presence of concentrated sulfuric acid and potassium permanganate. The solid GO was separated by centrifugation, washed repeatedly with deionized water and acetone until sulphate could not be detected with $BaCl_2$ and dried overnight in an airoven at 65°C. The dried GO powder is mainly composed of layered, but compactly fastened nanoplatelets of graphite.

2.3. Intercalation of GO with combined surfactants
Based on previous investigations [14–16], the neutral amine surfactants, ODA and POP, and the PPgMA oligomer, E43, were used in this study. In each case, a sample of 100 mg of GO was dispersed in 200 mL of p-xylene in a glass beaker, followed by the addition of 400 mg of ODA. Upon amine addition the GO solid swelled instantly, and the suspension was sonicated for 3 h. Proper amount of POP or E43 was then added based on the amine content and the mixture was again soincated for another 3 h. The ultrasonic processor VCX750 (Sonics & Materials), frequency 20 kHz, 750 watts, equipped with a medium probe made of high grade titanium alloy was used for preparing the organically modified GO. The stable dispersion of amine surfactant intercalated graphite oxide (GOA) was observed over 24 h. The code names are GOA for ODA only intercalated GO; and GOAP and GOAE for ODA+POP and ODA+E43, respectively.

2.4. Solution-blended PB/graphite nanocomposites
Appropriate amount of PB3150 were completely dissolved in p-xylene in a 250 mL glass beaker upon heating to 105°C, and subsequently the heated GOS suspension was added dropwise. After sonication for 4 h, a significant portion of p-xylene was removed under vacuum, and the well dispersed blend was cooled to 70°C. The separation of the resulting derivatives was achieved with a suction filter in order to remove the excess surfactants and p-xylene. Finally, the precipitate was washed well with acetone, and

then dried *in vacuo* at 100°C for 48 h. The resulting loose powder was hot pressed to produce the testing specimens. The composition of each composite was confirmed by thermal gravimetric analysis at 5 wt% of graphite filler. The choice of 5 wt% loading is based on our previous results, in which the calculated ionic conductivity was 10^{-5} S/m (30°C) at 5% loading of GOA, which was well above the percolation threshold.

2.5. Characterization

Wide-angle X-ray diffraction (WAXD) patterns of different samples were recorded on a Shimadzu XRD-6000 (40 kV/40 mA) diffractometer using Cu Kα radiation to characterize the nano-graphite dispersion and the crystalline structure of PB3150. Infrared spectra were recorded on a Shimadzu FT-IR spectrometer (Prestige-21) to identify the chemical groups of graphite due to oxidation and intercalation. The samples were measured in the form of KBr pellets. SEM images of the morphology of GO and functionalized GO powders were observed by field-emission scanning electron microscope (FESEM) JSM-6400 (JEOL, Japan) with accelerating voltage of 12 kV and working distance of 15 mm. The dispersion of graphite particles within the PPgMA matrix was also studied by SEM. The cryo-fractured sample surfaces were metallized with platinum using an ion coater IB-3 (Giko, Japan). Transmission electron microscopy (TEM) JEM-1200EX (JEOL, Japan) was used for direct observation of the intercalated lamellar structure of graphite oxide in the nanocomposites. Ultrathin samples were obtained by microtoming the sample plates.

The nonisothermal degradation behavior of PB3150 and its composites with fGOs was characterized by using a thermogravimetric analyzer (TGA Q500, TA Instrument). All measurements were performed under a nitrogen atmosphere from room temperature to 800°C at a heating rate of 20°C/min. Thermal properties of the composites were characterized using a Perkin-Elmer DSC Pyris 1 (Perkin Elmer, Boston, MA). The specimens were first heated to 200°C and held for 5 mins to ensure complete melting. The cooling traces were recorded with a cooling rate of 10°C/min from 200 to 0°C; and the melting traces were recorded by heating again to 200°C with a heating rate of 10°C/min. Dynamic mechanical analyzer (DMA), Perkin–Elmer 7e, was used to assess the mechanical performance of the composites. For the dielectric measurements of the pristine PB3150 and the nanocomposites covering the temperature range from 30 to 130°C and the frequency range from 1 to 10^4 Hz were carried out with a TA high-performance dielectric spectrometer DEA 2970. Note that compression molded specimens for both DMA and DEA were prepared on a hot press with a preheated mold at 180°C and 100 psi (about 0.7 MPa) for 10 min.

3. Results and discussion
3.1. Morphological characterization of functionalized graphite oxide

We first carried out the characterization of the nano-filler. The structure of the filler was investigated under a scanning electron microscope, shown in Figures 1a–1d for the graphite flakes of GO, GOA, GOAP and GOAE, respectively, after the sonicated dispersion dried on a glass for 24 hrs. It can be seen from Figure 1 that most graphite flakes were fragmented under extensive oxidation and ultrasonication, and produced graphite sheets with diameters ranging from about 1 to 10 μm. The starting material is the flake of graphite oxide (GO) in the form of thick plate as shown in Figure 1a with a magnification of 5000×. The arithmetic means of the particle dimensions were obtained by averaging at least 20 particles from the micrographs taken at different regions of the same specimen. Note that the micrographs of functionalized GO flakes are imaged with a magnification of 10 000×. The GOA flake (Figure 1b), with the thickness at ca. 80 nm, is apparently thinner than that of GO due to amine intercalation. Furthermore, the intercalating effect of oligomeric surfactants can be clearly seen in Figure 1c and 1d, where the stack of graphite sheet was exfoliated into thin plates, whose average thickness was around 50 nm for GOAP and 30 nm for GOAE, were generally thinner than that of GOA.

The powder X-ray diffraction (pXRD) patterns of GOS, the as prepared alkylamine intercalated GOA, GOAP, and GOAE are compared with that of unmodified GO in Figure 2. As expected, GO has a prominent, characteristic peak at $2\theta = 11.4°$, corresponding to an inter-graphene sheet spacing of 0.81 nm. However, the diffraction peak of GOA shifted to the left of GO due to the effect of alkylamine intercalation. There is an apparent increase of the d_{001} value up to 2.32 nm for GOA. The increased value confirms the incorporation of the ODA molecules in the
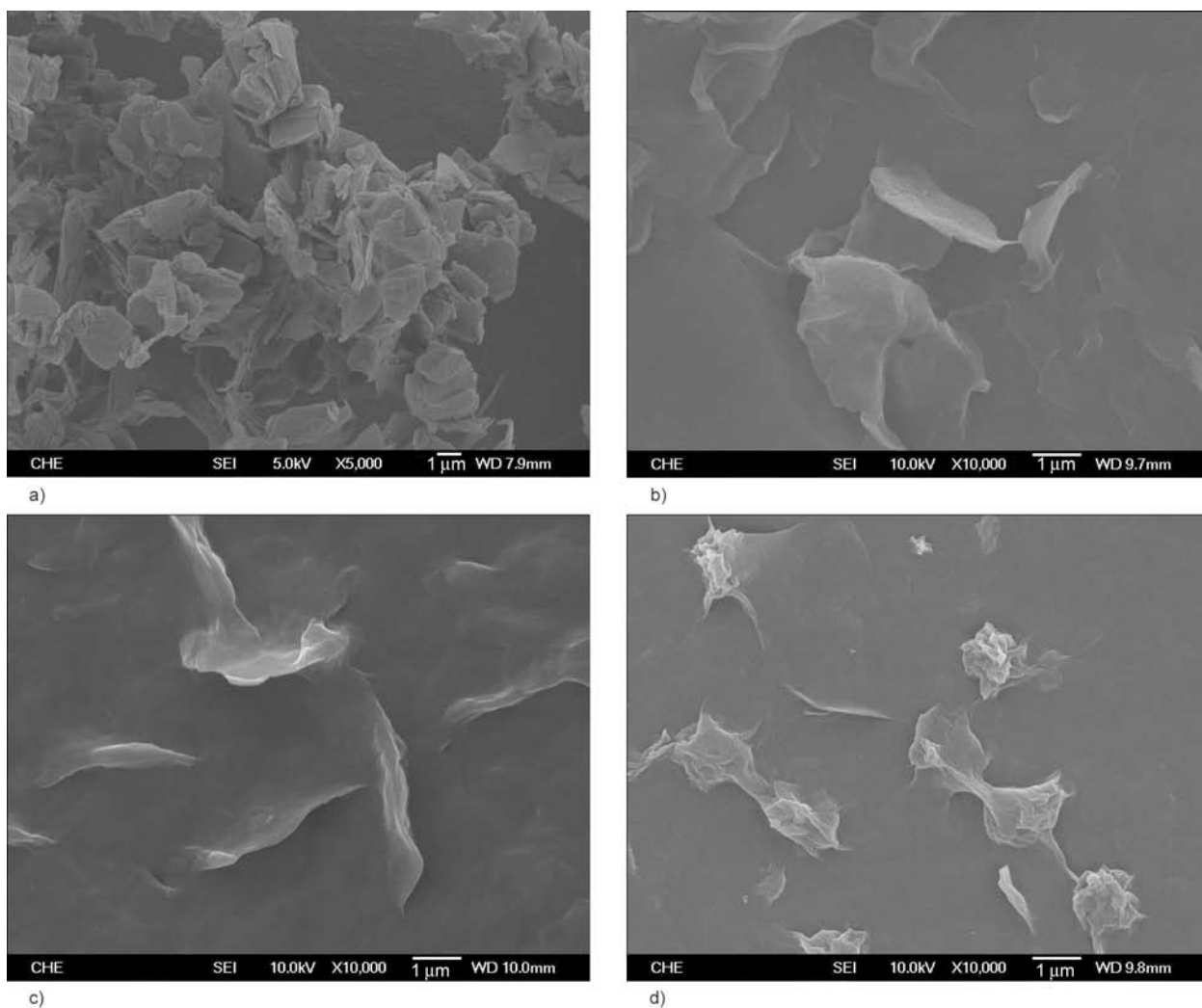
Figure 1. SEM micrographs of functionalized graphite oxide. (a) GO (5000×); (b) GOA; (c) GOAP; and (d) GOAE (10 000×).
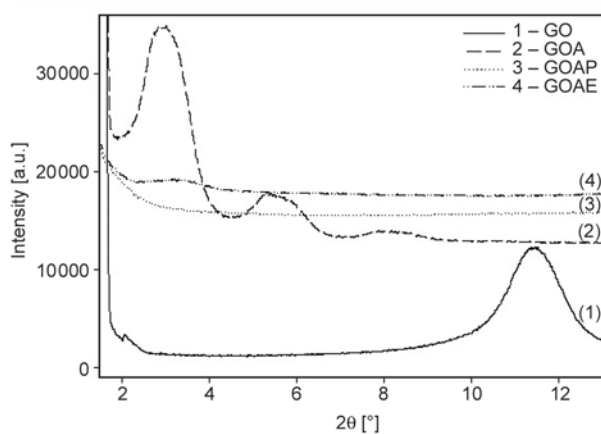

Figure 2. WAXD diffractograms of GO, GOA, GOAP, and GOAE

interlayer space of GO. Further, the intercalation by POP or E43 is even more significant. Compared to the starting GOA, in the POP and E43 intercalated samples the diffraction peak almost disappeared.

The amine or the maleic anhydride groups could be inserted in the interlayer zone of GOA either by hydrogen bonding interactions between the functional molecules and oxygen containing functional groups of GO or by exchange of protons of the acidic groups of GO with alkylamine or anhydride [15].

The intercalation of GO was also confirmed by infrared spectroscopy. FTIR spectra of GO, GOA, GOAP and GOAE are presented in Figure 3. As expected, the spectrum of GO is in good agreement with previous works [15, 16]. The broad band at 3400 cm^{-1} is attributed to stretching of the O–H bond of CO–H or water. The band at 1720 cm^{-1} is associated with stretching of the C=O bond of carbonyl or carboxyl groups. The band present at 1623 cm^{-1} is attributed to deformations of the O–H bending vibration. Stretching vibrations of the C–O bond is observed as the intense band present at 1043 cm^{-1}. In addition to the disappearance of the
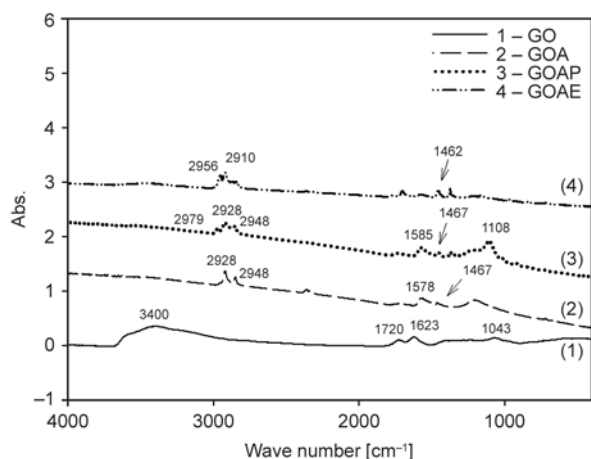
Figure 3. FTIR spectra of GO, GOA, GOAP, and GOAE

absorption bands at 3400 and 1623 cm^{-1}, the FTIR spectra of GOA differ from that of GO in the signals observed at 1043, 1467, 1578, 2848, and 2928 cm^{-1}. The intensity of the first peak is reduced significantly. The next two peaks are assigned to the bending vibration of –CH$_2$–, and vibration of the N–H groups of the intercalants, respectively. The strongest signals, observed at higher frequencies, are attributed to asymmetric (2928 cm^{-1}) and symmetric (2848 cm^{-1}) stretching of the methylene group of the alkylamine. For GOAP spectra, it shows one additional band relative to that of GOA. The band at 1108 cm^{-1} is assigned to the C–O vibrations along the POP backbone. Further, the reduction in interlayer water content in GOA and GOAP is also confirmed from the fact that the intensities of the peaks at 3400 and 1623 cm^{-1} clearly decrease compared to that of GO. Finally, for GOAE spectra, besides the disappearance of both bands at 3400 and 1623 cm^{-1}, the band at 1720 cm^{-1} is assigned to the carbonyl vibration in carboxylic acid. The absorption bands in the region of 2848 to 2956 cm^{-1} are related to the characteristic of the methyl group and the methylene unit on the polypropylene backbone. Further, the disappearance of the bands at 3400 and 1623 cm^{-1} (due to O–H stretching and bending, respectively), and at 1043 cm^{-1} (due to C–O stretching) strongly indicated the reduction of GO during functionalization. In addition, though the results are not presented here, we also observed the color change of the GO suspension from light brown before sonication to deep black (color of parent graphite) after suspension.

3.2. Possible intercalation/exfoliation mechanism

Now let us consider the intercalation/exfoliation mechanism of the GO with various surfactants. The intercalation of ODA into the graphene layers has been well studied [18–21]. Figure 4 presents a schematic representation of the intercalation/exfoliation process of the three surfactants, i.e., ODA, POP, and E43, with GO. In the first stage the strong interaction of hydrogen bonding between the amino groups of ODA and the oxygen groups of the graphite oxide opened up the interlayer spacing of GO, and the attraction among the graphite layers should be weakened. Next the ODA modified GO (GOA) further intercalated/exfoliated with the oligomers POP diamine (upper route) and E43 (lower route). We acknowledge that the chemistry of POP and E43 with GO is different. Nonetheless its effect is insignificant because both surfactants are able to react with the dominant oxidation groups of GO [15] as seen in Figure 4. Hence the molecular weight (chain length) of the oligomers is responsible for the improved dispersion of fGO in the composites. Since the miscibility of E43 (PPgMA oligomer) with polypropylene is good enough to blend at the molecular level, it will form uniformly dispersed fGO nanocomposite in the polypropylene matrix. On the other hand, since the miscibility between POP diamine and polypropylene is poor, the phase separation occurs within the nanocomposite (see later discussion). Therefore, it is quite reasonable to say not only the intercalation ability of the oligomers but also the miscibility should be a very important factor to achieve the exfoliated homogeneous dispersion of the fGOs in this novel approach using oligomers as a compatibilizer.
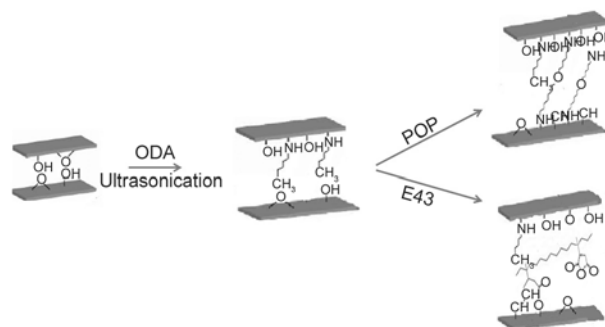

Figure 4. Schematic of the synthetic mechanism of organically modified graphite oxide

3.3. Morphology and properties of polymer/graphite nanocomposites

We first studied the thermal stability and determined the composition of the fGO composites by the thermogravimetric analysis (TGA). Figure 5 shows TGA thermograms (Figure 5a) and their derivative weight curves (Figure 5b). The enlarged graphs in the range from 350–500°C were inserted in the lower left or upper-right corners of Figures 5a and 5b, respectively, to see clearly the difference among various hybrids. Those are the measurements of neat PB and PB/GOA, GOAP, and GOAE nanocomposites with 5 wt% graphite contents. Thermal degradation profiles of the nanocomposites displayed that thermal stability of the nanocomposites was improved with the increasing fGO content. For the quantitative comparison of thermal stabilities among the tested specimens, the maximum thermal degradation temperatures, T_d, evaluated from the peak value of DTG curves were summarized in Table 1, together with the weight fractions of graphite and the surfactant of each specimen. Note that the weight fractions of amine content and hence the polymer content were determined from the TGA results of the GOA powders, and the graphite contents were confirmed by the residual weights in Figure 5a. As listed in Table 1, the PB content decreased from 88 to 44 wt% as the surfactant content increased

from 7.5 to 50 wt% with increasing dose of oligomeric surfactants.

Next, the T_d of unfilled PB was determined to be about 450.8°C. And the T_d's of the composites increased from ca. 18°C of GOA (the lowest) to ca. 24°C of GOAE (the highest) against the unfilled matrix. This improved thermal stability of the nanocomposites is believed to originate from the fact that graphite nanoplatelets of GOAs, which were dispersed homogeneously in the PB matrix, serve as the mass transfer barriers against the volatile pyrolized products in the PB matrix, eventually retarding thermal degradation of the nanocomposites. Next, it can be clearly seen that only the DTG curve of the PB/GOAP composite showing a small shoulder at ca. 406°C, which may arise from the incompatibility between POP and PB matrix. The incompatible PB-POP pair will be further elucidated in DMA analysis. Finally, we also noticed that the onset of thermal decomposition was earlier for the nanocomposites compared to pure PB. The free surfactant and other small molecule impurities may cause the nanocomposites decompose earlier than the pure PB. However, after decomposition of the volatile components, the functionalized graphene nanosheets played the major role in enhancing the degradation temperatures of the nanocomposites.

Figures 6a, 6c, and 6e are the images of the cryogenically fractured surfaces of GOA, GOAP and GOAE composites at 5 wt% loading, respectively, with low magnification of 5000×; and Figures 6b, 6d, and 6f at high magnification of 30 000×. As can be seen in the low magnification images, with the filler addition, the fractured surfaces become rough with few microcracks near the fGO flakes, consistently with the hypothesis of heterogeneous nucle-

Table 1. Onset and peak degradation temperatures and char content of PB/fGOs

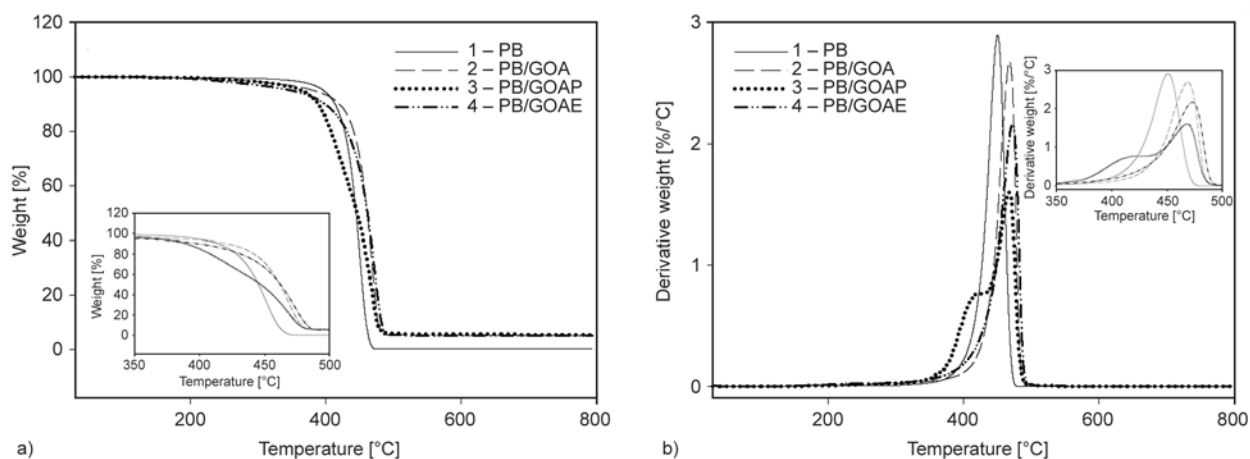| Sample code	T_{onset}	T_d	Matrix	Modifiers	Char
	[°C]		[wt%]	[wt%]	[wt%]
PB	273.3	450.8	100	–	0.3
PB/GOA	262.8	468.3	87.6	7.4	5.1
PB/GOAP	259.4	472.4	71.2	23.8	5.1
PB/GOAE	261.5	474.3	43.8	51.2	5.1

Figure 5. TGA thermograms of neat PB and nanocomposites. (a) weight loass curves; (b) derivative weight loss curves.
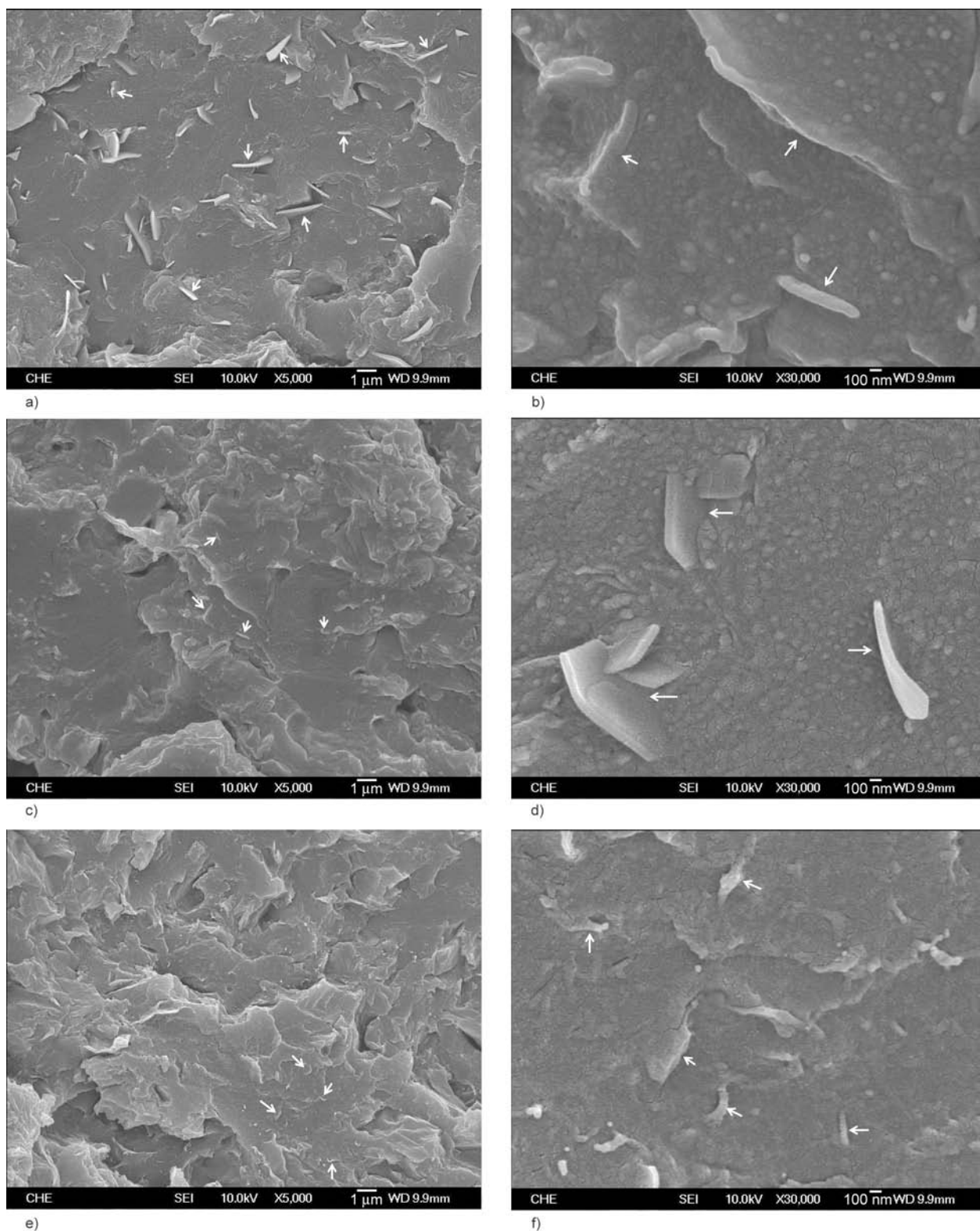
Figure 6. SEM micrographs of the cryogenically fractured surfaces of the nanocomposites at 5 wt% loading. (a) PB/GOA; (c) PB/GOAP; (e) PB/GOAE at 5000×; (b) PB/GOA; (d) PB/GOAP; (f) PB/GOAE at 30 000×.

ation by graphite. It can also be seen that the fractured surfaces of all specimens exhibit uniform dispersion of fGO nanoplatelets particles. The images of the fGO flakes appear much brighter than the surrounding PB matrix, and many platelets are pro-

truded from the fractured surface due to weak interfacial adhesion. However, as marked by the arrows in Figures 6c and 6e, most of the GOAP and GOAE flakes are embedded in the PB matrix. The intercalated or exfoliated graphite nanoplatelets not only

are uniformly dispersed in the nanocomposites, but exhibit good adhesion between the organic-inorganic constituents. The edge-on view of the nanoplatelets of the organically modified fGOs can be clearly seen from the high magnification images of 30 000× in Figures 6b, 6d and 6f, which show the thickness of the flakes is about the same order as that shown in Figure 1 of the images of the fGO powders. Note that the interfaces remain intact hardly seeing any microcracks or defects due to strong interfacial adhesion between fGO flakes and PB matrix.

We also employed XRD to further characterize graphite dispersion in the composites samples. In nanocomposites containing organoclay, increasing exfoliation is associated with a reduction of the peak intensity in XRD characteristic of the repeated layer spacing. We apply the same principle in graphite-based samples. As seen in Figure 7, the X-ray diffractograms of neat PB3150 and the PB-graphite hybrids made by solution blending. Neat PB3150 has several XRD peaks between $2\theta = 14.0$
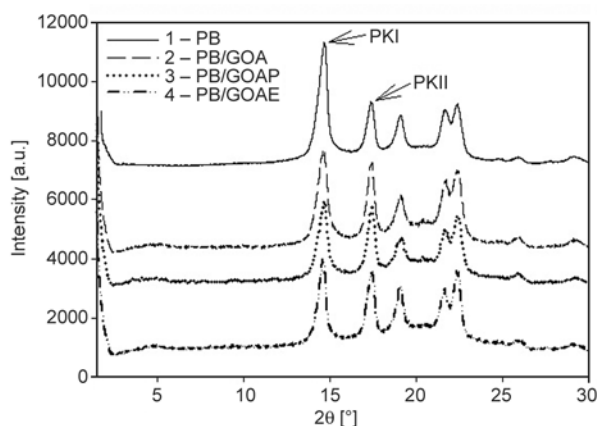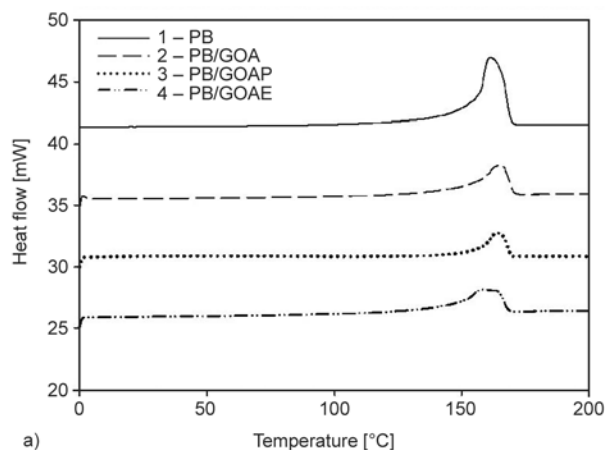
and 28.3°, consistent with the PP crystal unit cell [19, 20]. All the composite systems exhibit peaks associated with neat PP, although the peak intensities are decreased in the hybrid. The pristine grahite exhibits a diffraction peak at 26.6°, associated with the inter-graphene sheet spacing, which is almost totally suppressed in the PB/fGO samples. This strongly suggests that significant exfoliation/dispersion of the GOA and GOAE and GOAP flakes was achieved under ultrasonication. The X-ray diffraction results supplement the morphological observations from electronic microscopy. In addition, the relative intensities of PkI and PkII changed in the diffractogram of PB/GOA. The intensity ratio of PkII/PkI was considerably more intense for polypropylene/fGO composites than the unfilled matrix. It has been reported [19] that the high relative intensities of PkII to PkI in the presence of graphite was attributed to the strong preferential growth of PP crystallites along the b-axis during nucleation, since the PkII corresponds to (040) reflection of α-form of crystalline PP. Furthermore, the high intensity of PkII suggests high degree of crystallinity. It can be clearly seen that the intensity of PkII of PPgMA/graphite nanocomposites is in the descending order GOA>GOAP>GOAE. Note that with the same graphite content at 5 wt% for each composite, the PB content decreases from 88 wt% in PB/GOA to 44 wt% in PB/GOAE due to the incorporation of oligomeric surfactants. The nucleating effect of fGOs on PB matrix was further investigated in the crystallization and melting behavior of PB/fGO with differential scanning calorimetry (DSC).

Figure 8 shows the DSC cooling (Figure 8a) and heating (Figure 8b) curves of PB and the PB composites. In Table 2 we summarized the values of the
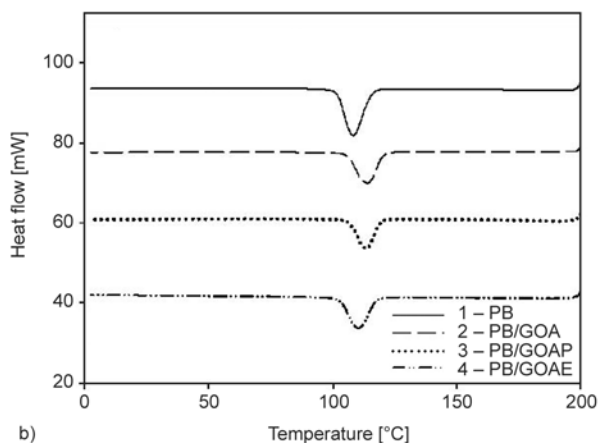

Figure 7. WAXD diffractograms of neat PB3150 and composites at 5 wt% loading

Figure 8. DSC thermograms of PB3150 and nanocomposites (a) cooling curves and (b) heating curves at 5 wt% loading

Table 2. Crystallization, melting temperatures and enthalpies of PB/fGOs

Sample code	T_m [°C]	ΔH_m (normalized) [J/g]	T_c [°C]	ΔH_c (normalized) [J/g]
PB	157.5	89.2	108.2	90.6
PB/GOA	164.7	97.8	113.9	101.3
PB/GOAP	164.2	94.3	113.2	99.2
PB/GOAE	160.3	96.6*	110.2	95.8*

*Note: ΔH_m and ΔH_c of PB/GOAE hybrid was normalized to the total weight fraction of PB and E43 (87.6 wt%).

temperature and enthalpy of crystallization and melting. The values of ΔH_c and ΔH_m were normalized by the weight content of PB in the composite. We first take a look at the T_c values of all the PB composites, which increased about 10°C compared with that of neat PB. This was due to the nucleating effect of graphite on the PB crystallization. And the PB/GOA composite showed the greatest increase in T_c. Further, it clearly showed that, from the DSC cooling curves of the PB composites, the crystallization of PB in PB/GOAP was faster than in PB/GOAE, as the DSC peak temperature for the former was a little higher than those of the latter. It was because the high content of E43 (44 wt% in the composite PB/GOAE), which is fully compatible with PB matrix as seen from DMA measurements, may interfere with the PB crytallization. Accordingly, the normalized degree of crystallinity (ΔH_c and ΔH_m) of PB in the composites is in the descending order as follows: PB/GOA>GOAP>GOAE. The high enthalpies and the high T_c observed in the PB/organically functionalized GO composites point to the apparent effect of nucleation, which could be probably attributed to the enhanced interfacial interaction between PB and fGO resulting from the great increase in the

specific surface area of fGO after dispersion/exfoliation in the sonication bath.

The dynamic mechanical behavior of unfilled PB and PB/graphite nanocomposites are presented in Figures 9a and 9b with 5 wt% of graphite. The storage (or elastic) moduli (E') are presented in Figure 9a. The E' values of all the samples at nominated temperatures are listed in Table 3. From the E' curves it is apparent that, in the presence of graphite fillers, the E' of the composites was greater than that of unfilled PB throughout the temperature range. The maximum of the glassy E' of filled PB at –50°C and –10°C was observed for PB filled with GOAP. It increased from 723 MPa (unfilled PB) to 1041 MPa (PB/GOAP) at –50°C, which is higher than that of PB filled with GOAE (924 MPa). Note that the PB content is ca. 57 wt% in the PB/GOAP composite, and the high content of E43 oligomer at ca. 40 wt% is responsible for the low E' of the PB/GOAE composite. However, above room temperature (around 30°C), the E' of the PB/GOAE hybrid became the highest among the tested samples. The incompatibility between POP and the PB matrix may lead to the drop in E' at high temperature regime.

Whilst the E' of filled PB increased with subsequent additions fGO, it was found that the reinforcing

Table 3. Dynamic storage moduli and glass transition temperature of unfilled PB and PB/fGOs at nominal temperatures

Sample code	E' [MPa]			T_g [°C]
	–50°C	–10°C	30°C	
PB	732.9	638.8	390.1	1.2
PB/GOA	806.0	720.6	504.6	1.0
PB/GOAP	1041.7	844.9	470.1	1.3
PB/GOAE	923.9	792.5	525.5	2.3
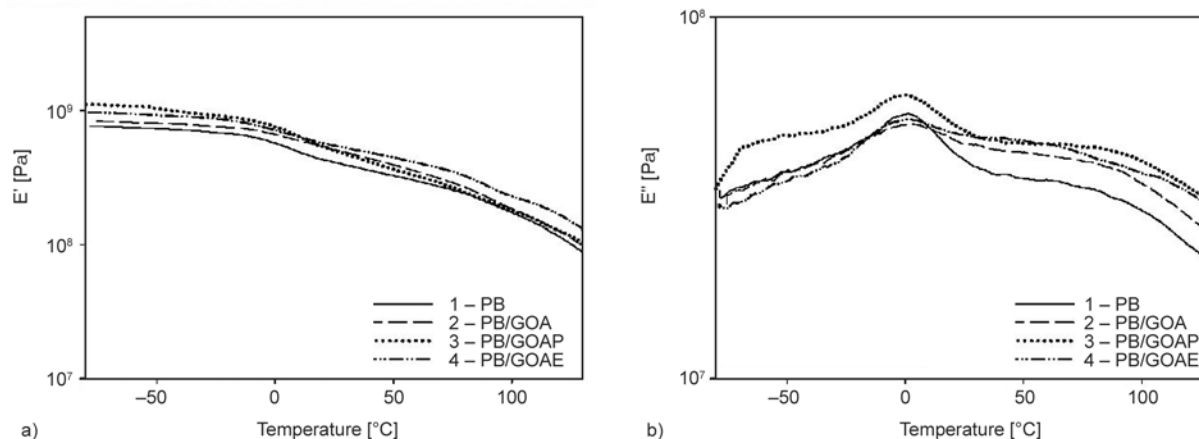
Figure 9. (a) Storage modulus and (b) loss modulus curves of neat PB and nanocomposites at 5 wt% loading as a function of temperature

effect is more prominent in mixed surfactants modified GO than in ODA alone. The lower E' of PB/GOA is believed to be attributed to the greater concentration of graphite stacks (as a result of mild intercalation) than that of PB/GOAP and GOAE. This overabundance of GOA stacks resulted in some filler particles likely unable to bond to POP or MA substituents, which in turn limited the improvement in the composite mechanical properties. The glass transition (T_g), which is the viscoelastic transition of a material, is often drawn from the maxima of E'' curve as shown in Figure 9b. In this case the E'' curves were used to obtain the T_g. The T_g of the unfilled PB is approximately 1.2°C. It can be clearly seen that the T_g's of the nanocomposites are generally higher than that of unfilled PB except the GOA hybrid. Similar to the trend of E' above T_g, the T_g of PB/GOAE is the highest at 2.3°C, followed by both PB/GOAP at 1.3°C and PB/GOA at 1.0°C. The increase in T_g is ascribed to a decrease in mobility of the polymer chains, due to the strong interactions, hydrogen bonding between the polar groups of PB and fGO. This observation is also consistent with the behavior of other filled polymeric systems [21]. Finally, the T_g of POP oligomer is also clearly seen form E'' curve of PB/GOAP at –67.7°C, while the PB/E43 system only showed single T_g representing a fully compatible blend.

The dielectric measurements of the PB/fGO nanocomposites, extending over a frequency range from 10^0 to 10^5 Hz at 110°C, are shown in Figure 10a and 10b. As can be seen form Figure 10a, the dielectric constant, ε', of PB/fGO hybrids (at ca. 10^3) is much higher than the unfilled matrix (not shown here) due to the interfacial polarization around the exfoliated GO nanoplatlets [46]. Note that the neat matrix

maintains a constant ε' at 2.2 without dielectrically active relaxation process. Moreover, as expected, the ε' decreased with increasing frequency, and the PB/GOAE composite displays the greatest ε' among the composites because of the high degree of exfoliation of the fGO in the hybrid.

The dielectric loss, ε'', of the PB/fGO composites at 110°C were presented in Figure 10b. As expected, the ε'' of PB/GOAE is about twice that of PB/GOAP, and about four times that of PB/GOA through the experimental temperature range. The functionalization of GO through the intercalation of various surfactants increased the interlayer spacing of the intercalated graphite layered stacks, and facilitated the exfoliation of the graphite nanolayers in the composites. Note that the molecular interaction between the polymer chain segments and nanolayers is greatly enhanced in the PB/GOAE hybrids due to enormous increase in the interfacial area [47] arising from extensive exfoliation by E43 oligomer which is fully compatible with the PB matrix. Hence, in this configuration, the heterogeneous graphite nanolayer inclusions often cause dielectric polarization as a result of the accumulation of charge carriers at the interface of two media with different permittivities or conductivities. Therefore, it can form an effective nanosized capacitor structure [47, 48], and provide increased values of bulk permittivity and loss factor in such a nanostructured morphology.

Figure 11 show the changes of the ac conductivities at 110°C of PB/fGO composites as a function of frequency with the graphite content at 5 wt.%. Note that the ac conductivity σ_{ac} was calculated from ε'' with the Equation (1) [46]:

$$\sigma_{ac} = \omega \cdot \varepsilon_0 \cdot \varepsilon'' \tag{1}$$
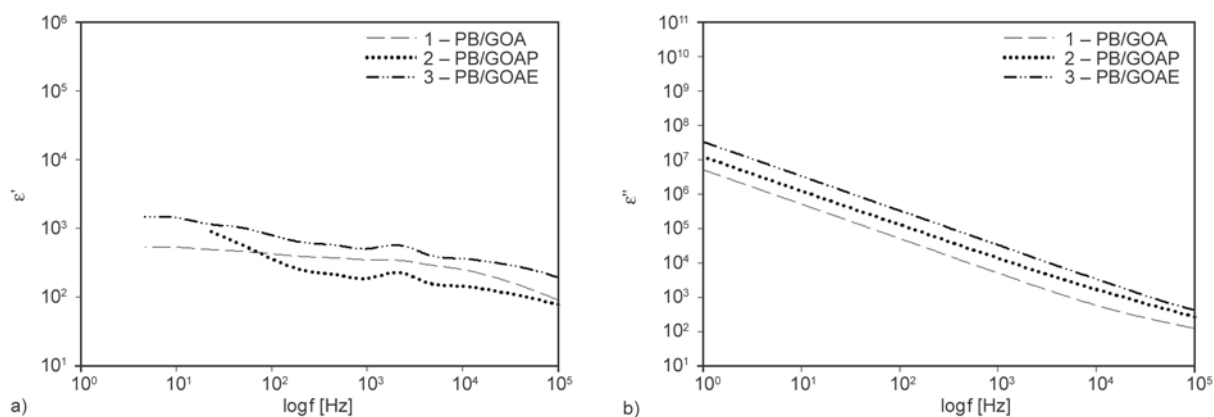

Figure 10. Frequency sweep curves of (a) dielectric permittivity and (b) dielectric loss at 110°C for PB nanocomposites of 5 wt%
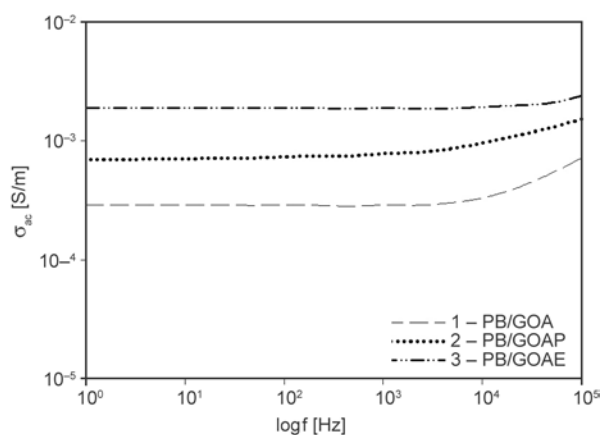
Figure 11. Ionic conductivities vs frequency at 110°C for PB nanocomposites of 5 wt%

where ω is the angular frequency, ε_0 is the absolute permittivity of free space, and ε'' is the dielectric loss. It is clearly seen that σ_{ac} changes drastically with frequency. At low frequency a plateau where σ_{ac} is frequency independent can be observed clearly in the plots. At higher frequencies, σ_{ac} increases rapidly with increasing frequency. The transition region from *dc* (frequency-independent ionic conductivity) to *ac* (frequency-dependent) conductivity shifts to higher frequencies with GOAP and GOAE filled composites. Note that the ionic conductivity of neat PB is evaluated to be in the order of 10^{-13} S·m^{-1}, which is not shown here. We believe that the significant increase in ionic conductivity for both hybrids is associated with the homogeneous dispersion of GOAP and GOAE in the polymer matrix. Furthermore, the ionic conductivity of the PB/GOAE composite was close to 10^{-3} S·m^{-1} with only 5 wt% graphite content. It is apparent that the greater degree of exfoliation/dispersion of GOAE in the PB matrix also gave rise to the higher ionic conductivity than the other modified fGOs. It is noticeable that the ionic conductivity of PB/GOAE composite is enough to attain the electrostatic dissipation and/or partial electromagnetic dissipation for thermoplastics, fibers, and films.

4. Conclusions

Three different surfactants with two high-molecular weight oligomers were investigated for modifying GO. The ultrasonication was demonstrated to be an efficient approach to simultaneously functionalize and reduce GO without the use of any chemical agents. The functionalization of GO with organic oligomeric surfactans make the hydrophilic GO

hydrophobic and thus improves the dispersion of fGO in PB matrix. The morphological and the spectroscopic characterizations indicated that fGO was well intercalated/exfoliated in the polymer matrix. In particular, GOAE showed greater degree of dispersion than GOAP in the composites due to the compatibility between E43 and the polymer matrix. In summary, reduction of exfoliated graphite oxide sheets in organic solvent via ultrasonication results in a material with graphitic characteristics that are comparable to those of pristine graphite. On the nanoscale, this carbon-based material consists of thin graphene-based sheets and possesses a high specific surface area, enhancing the interfacial interaction in the fGO nanocomposites. The further improvement in both the thermal and dielectric properties will be pursued in the future by optimizing the compatibility and adhesion at the fGO–PB interface, and by improving the dispersion and orientation of the graphite nanoplatelets through proper choice of long chain surfactant.

Acknowledgements

References

[1] Tan H., Liu Z. Y., Piao J. H., Chen X. F., Lou X. F., Li S. H.: Electrical behavior of carbon black-filled polymer composites: Effect of interaction between filler and matrix. Journal of Applied Polymer Science, **51**, 1159–1164 (1994).
DOI: 10.1002/app.1994.070510701

[2] Tchoudakov R., Breuer O., Narkis M., Siegmann A.: Conductive polymer blends with low carbon black loading: Polypropylene/polyamide. Polymer Engineering and Science, **36**, 1336–1346 (1996).
DOI: 10.1002/pen.10528

[3] Nagata K., Iwabuki H., Nigo H.: Effect of particle size of graphites on electrical conductivity of graphite/polymer composite. Composite Interfaces, **6**, 483–495 (1998).
DOI: 10.1163/156855499X00161

[4] Sun J-S., Gokturk H. S., Kalyon D. M.: Volume and surface resistivity of low-density polyethylene filled with stainless steel fibres. Journal of Materials Science, **28**, 364–366 (1993).
DOI: 10.1007/BF00357809

[5] Zweifel Y., Plummer C. J. G., Kausch H-H.: A microscopic investigation of conducting filled polymers. Journal of Materials Science, **33**, 1715–1721 (1998).
DOI: 10.1023/A:1004316229497

[6] Gibson A. G.: Processing and properties of reinforced polypropylene. in 'Polypropylene Structure, blends and composites' (ed.: J. Karger-Kocsis) Chapman and Hall, London, Vol. 3, 71–112 (1995).

[7] Wakabayashi K., Pierre C., Dikin D. A., Ruoff R. S., Ramanathan T., Brinson L. C., Torkelson J. M.: Polymer–graphite nanocomposites: Effective dispersion and major property enhancement via solid-state shear pulverization. Macromolecules, **41**, 1905–1908 (2008).
DOI: 10.1021/ma071687b

[8] Kim H., Macosko C. W.: Morphology and properties of polyester/exfoliated graphite nanocomposites. Macromolecules, **41**, 3317–3327 (2008).
DOI: 10.1021/ma702385h

[9] Kalaitzidou K., Fukushima H., Drzal L. T.: A new compounding method for exfoliated graphite–polypropylene nanocomposites with enhanced flexural properties and lower percolation threshold. Composites Science and Technology, **67**, 2045–2051 (2007).
DOI: 10.1016/j.compscitech.2006.11.014

[10] Wong S-C., Sutherland E. M., Uhl F. M.: Materials processes of graphite nanostructured composites using ball milling. Materials and Manufacturing Processes, **21**, 159–166 (2006).
DOI: 10.1081/AMP-200068659

[11] Park S., Ruoff R. S.: Chemical methods for the production of graphenes. Nature Nanotechnology, **4**, 217–224 (2009).
DOI: 10.1038/nnano.2009.58

[12] Li D., Müller M. B., Gilje S., Kaner R. B., Wallace G. G.: Processable aqueous dispersions of graphene nanosheets. Nature Nanotechnol, **3**, 101–105 (2008).
DOI: 10.1038/nnano.2007.451

[13] Kuila T., Bose S., Hong C. E., Uddin M. E., Khanra P., Kim N. H., Lee J. H.: Preparation of functionalized graphene/linear low density polyethylene composites by a solution mixing method. Carbon, **49**, 1033–1037 (2011).
DOI: 10.1016/j.carbon.2010.10.031

[14] Tang X-Z., Li W., Yu Z-Z., Rafiee M. A., Rafiee J., Yavari F., Koratkar N.: Enhanced thermal stability in graphene oxide covalently functionalized with 2-amino-4,6-didodecylamino-1,3,5-triazine. Carbon, **49**, 1258–1265 (2011).
DOI: 10.1016/j.carbon.2010.11.044

[15] Stankovich S., Piner R. D., Nguyen S. T., Ruoff R. S.: Synthesis and exfoliation of isocyanate-treated graphene oxide nanoplatelets. Carbon, **44**, 3342–3347 (2006).
DOI: 10.1016/j.carbon.2006.06.004

[16] Cao Y. W., Feng J. C., Wu P. Y.: Alkyl-functionalized graphene nanosheets with improved lipophilicity. Carbon, **48**, 1683–1685 (2010).
DOI: 10.1016/j.carbon.2009.12.061

[17] Bao R-Y., Cao J., Liu Z-Y., Yang W., Xie B-H., Yang M-B.: Towards balanced strength and toughness improvement of isotactic polypropylene nanocomposites by surface functionalized graphene oxide. Journal of Material Chemistry A, **2**, 3190–3199 (2014).
DOI: 10.1039/c3ta14554a

[18] Wang G., Shen X., Wang B., Yao J., Park J.: Synthesis and characterisation of hydrophilic and organophilic graphene nanosheets. Carbon, **47**, 1359–1364 (2009).
DOI: 10.1016/j.carbon.2009.01.027

[19] Lin Z., Liu Y., Wong C-P.: Facile fabrication of superhydrophobic octadecylamine-functionalized graphite oxide film. Langmuir, **26**, 16110–16114 (2010).
DOI: 10.1021/la102619n

[20] Bourlinos A. B., Gournis D., Petridis D., Szabó T., Szeri A., Dékány I.: Graphite oxide: Chemical reduction to graphite and surface modification with primary aliphatic amines and amino acids. Langmuir, **19**, 6050–6055 (2003).
DOI: 10.1021/la026525h

[21] Niyogi S., Bekyarova E., Itkis M. E., McWilliams J. L., Hamon M. A., Haddon R. C.: Solution properties of graphite and graphene. Journal of the American Chemical Society, **128**, 7720–7721 (2006).
DOI: 10.1021/ja060680r

[22] Kim H., Abdala A. A., Macosko C. W.: Graphene/polymer nanocomposites. Macromolecules, **43**, 6515–6530 (2010).
DOI: 10.1021/ma100572e

[23] Kuilla T., Bhadra S., Yao D., Kim N. H., Bose S., Lee J. H.: Recent advances in graphene based polymer composites. Progress in Polymer Science, **35**, 1350–1375 (2010).
DOI: 10.1016/j.progpolymsci.2010.07.005

[24] Wang Y., Tsai H-B.: Thermal, dynamic-mechanical, and dielectric properties of surfactant intercalated graphite oxide filled maleated polypropylene nanocomposites. Journal of Applied Polymer Science, **123**, 3154–3163 (2012).
DOI: 10.1002/app.34976

[25] Matsuo Y., Niwa T., Sugie Y.: Preparation and characterization of cationic surfactant-intercalated graphite oxide. Carbon, **37**, 897–901 (1999).
DOI: 10.1016/S0008-6223(98)00226-7

[26] Nethravathi C., Rajamathi M.: Delamination, colloidal dispersion and reassembly of alkylamine intercalated graphite oxide in alcohols. Carbon, **44**, 2635–2641 (2006).
DOI: 10.1016/j.carbon.2006.04.018

[27] Herrera-Alonso M., Abdala A. A., McAllister M. J., Aksay I. A., Prud'homme R. K.: Intercalation and stitching of graphite oxide with diaminoalkanes. Langmuir, **23**, 10644–10649 (2007).
DOI: 10.1021/la0633839

[28] Alexandre M., Dubois P.: Polymer-layered silicate nanocomposites: Preparation, properties and uses of a new class of materials. Materials Science and Engineering R: Reports, **28**, 1–63 (2000).
DOI: 10.1016/S0927-796X(00)00012-7

[29] Zhang S-P., Song H-O.: Supramolecular graphene oxide-alkylamine hybrid materials: variation of dispersibility and improvement of thermal stability. New Journal of Chemistry, **36**, 1733–1738 (2012).
DOI: 10.1039/c2nj40214a

[30] Lin J-J., Cheng I-J., Wang R., Lee R-J.: Tailoring basal spacings of montmorillonite by poly(oxyalkylene) diamine intercalation. Macromolecules, **34**, 8832–8834 (2001).
DOI: 10.1021/ma011169f

[31] Potts J. R., Dreyer D. R., Bielawski C. W., Ruoff R. S.: Graphene-based polymer nanocomposites. Polymer, **52**, 5–25 (2011).
DOI: 10.1016/j.polymer.2010.11.042

[32] Zheng Q., Xue Q., Yan K., Hao L., Li Q., Gao X.: Investigation of molecular interactions between SWNT and polyethylene/polypropylene/polystyrene/polyaniline molecules. Journal of Physical Chemistry C, **111**, 4628–4635 (2007).
DOI: 10.1021/jp066077c

[33] Lv C., Xue Q., Xia D., Ma M., Xie J., Chen H.: Effect of chemisorption on the interfacial bonding characteristics of graphene–polymer composites. Journal of Physical Chemistry C, **114**, 6588–6594 (2010).
DOI: 10.1021/jp100110n

[34] Kalaitzidou K., Fukushima H., Drzal L. T.: Mechanical properties and morphological characterization of exfoliated graphite–polypropylene nanocomposites. Composites Part A: Applied Science and Manufacturing, **38**, 1675–1682 (2007).
DOI: 10.1016/j.compositesa.2007.02.003

[35] Song P., Cao Z., Cai Y., Zhao L., Fang Z., Fu S.: Fabrication of exfoliated graphene-based polypropylene nanocomposites with enhanced mechanical and thermal properties. Polymer, **52**, 4001–4010 (2011).
DOI: 10.1016/j.polymer.2011.06.045

[36] Xu J-Z., Chen C., Wang Y., Tang H., Li Z-M., Hsiao B. S.: Graphene nanosheets and shear flow induced crystallization in isotactic polypropylene nanocomposites. Macromolecules, **44**, 2808–2818 (2011).
DOI: 10.1021/ma1028104

[37] An J. E., Jeon G. W., Jeong Y. G.: Preparation and properties of polypropylene nanocomposites reinforced with exfoliated graphene. Fibers and Polymers, **13**, 507–514 (2012).
DOI: 10.1007/s12221-012-0507-z

[38] Huang Y., Qin Y., Zhou Y., Niu H., Yu Z-Z., Dong J-Y.: Polypropylene/graphene oxide nanocomposites prepared by *in situ* Ziegler–Natta polymerization. Chemistry of Materials, **22**, 4096–4102 (2010).
DOI: 10.1021/cm100998e

[39] Hsiao M-C., Liao S-H., Lin Y-F., Wang C-A., Pu N-W., Tsai H-M., Ma C-C. M.: Preparation and characterization of polypropylene-*graft*-thermally reduced graphite oxide with an improved compatibility with polypropylene-based nanocomposite. Nanoscale, **3**, 1516–1522 (2011).
DOI: 10.1039/c0nr00981d

[40] Yun Y. S., Bae Y. H., Kim D. H., Lee J. Y., Chin I-J., Jin H-J.: Reinforcing effects of adding alkylated graphene oxide to polypropylene. Carbon, **49**, 3553–3559 (2011).
DOI: 10.1016/j.carbon.2011.04.055

[41] Wang D., Zhang X., Zha J-W., Zhao J., Dang Z-M., Hu G-H.: Dielectric properties of reduced graphene oxide/polypropylene composites with ultralow percolation threshold. Polymer, **54**, 1916–1922 (2013).
DOI: 10.1016/j.polymer.2013.02.012

[42] Pagé D. J. Y. S., Gopakumar T. G.: Properties and crystallization of maleated polypropylene/graphite flake nanocomposites. Polymer Journal, **38**, 920–929 (2006).
DOI: 10.1295/polymj.PJ2006020

[43] Wang Y., Huang S-W.: Solution intercalation and relaxation properties of maleated polypropylene/organoclay nanocomposites. Polymer-Plastics Technology and Engineering, **46**, 1039–1047 (2007).
DOI: 10.1080/03602550701522377

[44] Shen J-W., Chen X-M., Huang W-Y.: Structure and electrical properties of grafted polypropylene/graphite nanocomposites prepared by solution intercalation. Journal of Applied Polymer Science, **88**, 1864–1869 (2003).
DOI: 10.1002/app.11892

[45] Cerezo F. T., Preston C. M. L., Shanks R. A.: Morphology, thermal stability, and mechanical behavior of [poly(propylene)-grafted maleic anhydride]-layered expanded graphite oxide composites. Macromolecular Materials and Engineering, **292**, 155–168 (2007).
DOI: 10.1002/mame.200600303

[46] Böhning M., Goering H., Fritz A., Brzezinka K-W., Turky G., Schonhals A., Schartel B.: Dielectric study of molecular mobility in poly(propylene-graft-maleic anhydride)/clay nanocomposites. Macromolecules, **38**, 2764–2774 (2005).
DOI: 10.1021/ma048315c

[47] Wang Y., Huang S-W., Guo J-Y.: The state of clay dispersion in maleated polypropylene/organoclay nanocomposites via dielectric spectroscopy measurements. e-Polymers, **8**, 881–896 (2008).
DOI: 10.1515/epoly.2008.8.1.881

[48] Williams E. P. M., Seferis J. C., Wittman C. L., Parker G. A., Lee J. H., Nam J-D.: Dielectric nanocapacitance effect of thermoset polymeric matrix nanocomposites. Journal of Polymer Science Part B: Polymer Physics, **42**, 1–4 (2004).
DOI: 10.1002/polb.10663

Polyaniline integrated carbon nanohorn:
A superior electrode materials for advanced energy storage

S. Maiti, B. B. Khatua[*]

Materials Science Centre, Indian Institute of Technology, 721302 Kharagpur, India

Abstract. Fiber-like polyaniline (PANI)/carbon nanohorn (CNH) composites (PACN composites) were prepared as electrode materials for supercapacitor by simple method that involves *in-situ* polymerization of aniline in the presence of CNH in acidic (HCl) medium with noteworthy electrochemical performances. Thus, the prepared PACN composites show high specific capacitance value of ≈ 834 F/g at 5 mV/s scan rate compared to ≈ 231 F/g for pure PANI and CNH (≈ 145 F/g) at same scan rate of 5 mV/s. CNHs are homogeneously dispersed throughout the matrix and coated successfully. Thus, it provides more active sites for nucleation and electron transfer path. In addition, the composites show high electrical conductivity in the order of $\approx 6.7 \cdot 10^{-2}$ S·cm^{-1} which indicates the formation of continuous interconnected conducting network path in the PACN composites. Morphological study of the PACN composites was carried out by high resolution transmission electron microscopy (HRTEM) and field emission scanning electron microscopy (FESEM).

Keywords: nanocomposites, supercapacitor, polyaniline, carbon nanohorn, electrical conductivity

1. Introduction

Presently, various motor vehicles and portable electronic devices have increased the requirement of energy storage devices. Thus, high performance supercapacitors and different batteries (Li-ion, Pb-acetate etc) have been attracted in the various fields of applications. Recently, supercapacitors have been a major source for huge amount of energy in a very small period of time and make them essential for surge power delivery. Supercapacitors have been considered most promising materials for alternative energy sources in the different device and electronics applications due to their rapid charging-discharging rates, high power density and long cycle life (>100 000 cycles) [1–3]. Thus, they have been taken as more important components for all electric cars and cars based on fuel cells like hydrogen fuel cell and direct methanol fuel cell (DMFC) in the modern generation [4, 5]. In general, supercapacitors have

been greatly used as complementary devices to different fuel cells and batteries due to their high energy densities but unable to supply a high power during short time period. The electrochemical capacitors have high-power sources and have been used also for digital communication devices [6–9]. Depending on the charge-storage mechanism, supercapacitors have been categorized into two different types [10, 11]: (a) electrical double-layer capacitors (EDLCs) for carbon-based active materials with high surface area, the capacitance value is obtained due to the charge separation at the electrode-electrolyte interface. The charge storage mechanism for EDLCs is of non-Faradic type; electrical charge builds up at the electrode-electrolyte interface. Generally, EDLCs have high power density but major disadvantage is low capacitance and low rate capability. In the case of EDLCs, the charge can be stored electrostatically or non-Faradaically (in case of carbon nanomateri-

als) like conventional capacitors and charge transfer does not occur between the electrode and the electrolyte, and (b) others are pseudocapacitors which develop fast and reversible surface or near surface reactions for charge storage. For pseudocapacitors, electrode materials may be metal oxides (NiO, MnO_2 etc) or conducting polymers and Faradic reactions occur at the electrode-electrolyte interface. The charge is stored Faradaically through charge transfer between electrolyte and electrode. This process is completed through electro-sorption, reduction–oxidation reactions, and intercalation processes. Among them, pseudo-capacitors could be the source of higher specific capacitance. However, major drawback of pseudo-capacitors is that they are very costly and show low conductivity. Hence, the energy storage performance of the capacitors needs to be improved for their broad potential applications under the current requirements. The high electrical conductivity, high surface area and a fast cation intercalation/de-intercalation process play a crucial role to obtain high energy and power densities for capacitors. In the case of carbon-based EDLCs, the charge storage mechanism occurs via electrostatic forces and fast faradaic redox reactions are the reason behind the storage mechanism for pseudo-capacitors.

Transition metal oxides play a key role as potential electrode materials for the preparation of supercapacitors due to their charge storage mechanisms [12, 13]. Among the different metal oxides, RuO_2 shows high capacitance value for its redox transitions. However, the major problem of Ru metal is its high cost which reduces its commercial value as a potential electrode material. Currently, the preparation of cost-effective electrode materials has become great challenge for supercapacitor applications. Cheap metal oxides such as oxides of Co, Ni, Mn, In, Fe, Sn, Pb [14, 15] and so forth are being investigated to improve the capacitance value of the capacitors. The conducting polymers are also used as electrode materials for supercapacitors for its excellent electrochemical properties and low cost. Among the several conducting polymers such as polyaniline (PANI), polythiophene (PTH), polypyrrole (PPy) and their derivatives, PANI has been considered more useful material for supercapacitors due to its redox reversibility, high electrical conductivity, easy synthesis procedure, good environmental stability and of course its low cost [16]. However, chemically synthesized electrically conducting polymers are generally powdery and behave like an insulating material in their undoped states. Thus, carbon-based nanomaterials have been considered most promising materials for supercapacitors due to their high surface area, high aspect ratio, nano-size and very high electrical conductivity [17]. In this regard, different carbon based nanomaterials such as carbon nanotube (CNT), graphene and carbon nanohorn (CNH) have been chosen as substrate for metal oxide nanoparticles or conducting polymers for supercapacitor applications. This carbon based conducting nanomaterials help to enhance the electron transfer rate during Faradaic charge transfer reactions in the composites and increase the value of specific capacitance [18]. Single-walled carbon nanohorns (SWCNHs) are dahlia flower like spherical superstructure of aggregated nano-sized graphitic tubes [19–21]. Due to the high surface area, considerable internal nanospace, excellent porosity and high electrical conductivity, they have been broadly used in the various filed of applications such as supercapacitors, hydrogen storage, fuel cells, drug delivery and biosensors, etc. Moreover, CNHs possess high purity and also high absorbability compared with others carbon based nanomaterials due to their large surface area, high aspect ratio and inherent micropores at interstitial sites.

Several research groups have been developed PANI composites based on metal oxides, graphene or CNH for supercapacitors. For instance, Wu *et al*. [22] showed the large electrochemical capacitance of ≈ 210 F/g at a discharge rate of 0.3 A/g in composite films of chemically converted graphene (CCG) and polyaniline nanofibers (PANI-NFs) prepared by vacuum filtration of the mixed dispersions of both the components. Deshmukh and Shelke [23] synthesized Fe_3O_4-SWCNH nanocomposites and reported specific capacitance value of the nanocomposites was ≈ 377 F/g at current density of 1 A/g. Wang *et al*. [24] prepared one-dimensional and layered parallel folding of cobalt oxalate nanostructures and reported the maximum specific capacitance of ≈ 202.5 F/g at a current density of 1 A/g with a voltage window from 0 to 0.40 V. Kumar *et al*. [25] have prepared conducting polyaniline-grafted reduced graphene oxide (PANi-g-rGO) composite via acyl chemistry and reported the capacitance of ≈ 250 F/g with electrical conductivity as high as ≈ 8.66 S/cm.

In this study, we have prepared PACN composites through cost effective method which involves *in-*

situ polymerization of aniline in the presence of CNH. Thus, prepared PACN composites show very high specific capacitance value ($\approx$ 834 F/g) at scan rate of 5 mV/s which is higher than the specific capacitance ($\approx$ 231 F/g at 5 mV/s) of pure PANI and CNH ($\approx$ 145 F/g) at same scan rate of 5 mV/s. So, specific capacitance value of the pure PANI is greatly affected in the presence of CNH in the PACN composites. Due to homogeneous coating of conducting CNH in the PACN composites, it forms a conducting electron transfer path and provides more active sites for nucleation [26] and increases the capacitance value of the composites. Additionally, the synthesized PACN composites showed electrically conducting behavior and obtained electrical conductivity of the composites is $\approx$ 6.7·10^{-2} S/cm which indicates the possible formation of conducting network structure in the PACN composites.

2. Experimental
2.1. Materials details
Aniline, hydrochloric acid (HCl) and potassium chloride were purchased from Merck, Germany. Single-layer carbon nanohorn (CNH, carbon purity: >99%, horn diameter: 3~5 nm, horn length: 30~50 nm, cluster diameter: 60~120 nm, density: 1.1 g/cm^3, surface area: 250~300 m^2/g) was procured from J. K. Impex, Mumbai, India. Cetyl trimethylammonium bromide (CTAB) and ammonium persulfate (APS) [(NH$_4$)$_2$S$_2$O$_8$] were purchased from Loba Chemie Pvt. Ltd. India.

2.2. Preparation of the PACN composites
100 mL of 1.5 (M) HCl was taken in a 500 mL beaker and 30 mg of CNH and CTAB were added to this acid solution. Then, the mixture was ultra-sonicated for 1 h for homogeneous dispersion of CNH in the acid media, followed by vigorous stirring for 30 min with magnetic stirrer at room temperature. After that, 1 mL aniline was added to this acidic solution of CNH and continued the stirring for another 10 min. Furthermore, ammonium persulfate (APS) solution (which was prepared through dissolving 2 mg APS in 100 mL 1.5 (M) HCl) was added into the reaction mixture as an oxidizing agent for polymerization of aniline and the stirring was continued. After 4 h of stirring, the solution became green and precipitation was observed. Then, the green solution was filtered and washed with de-ionized (DI) water for several times to make neutral solution. Thus, the obtained

residue was air dried for 24 h for further characterizations. Polyaniline (PANI) was also prepared by the same procedure in the presence of CTAB.

3. Characterizations
3.1. Field emission scanning electron microscope (FESEM)
The morphology of the PACN composites was studied using PACN pellets (prepared by pressing at room temperature) through FESEM (FE-SEM, Carl Zeiss-SUPRA™ 40), with an accelerating voltage of 5 kV. The samples were coated with a thin of layer gold (approx ~ 5 nm) to avoid the electrical charging during scanning. This gold coated composites sample was scanned in the vacuum order of 10^{-4} to 10^{-6} mm Hg.

3.2. High resolution transmission electron microscope (HRTEM)
The TEM analysis of the PACN composites was carried out by HRTEM (HRTEM, JEM-2100, JEOL, JAPAN), operated at an accelerating voltage of 200 kV. A small amount of the PACN composites was dispersed in acetone through sonication. Then, the dispersed suspension of PACN composites was dropped on the copper (Cu) grid for HRTEM analysis.

3.3. Electrochemical characterization
Electrochemical analysis of as-synthesized PACN composites, pure PANI and CNH was performed by cyclic voltammetry (CV) with a CH instrument electrochemical analyzer. A three-electrode system was employed for all measurements where PACN composites coated glassy carbon electrode, Pt wire and Ag/AgCl served as working, counter and reference electrodes, respectively. Cyclic voltammogram was recorded at different scan rates from 5 mV/s to 100 mV/s within potential windows from –0.4 to +0.8 V in 1 (M) KCl.

The electrochemical impedance spectroscopic (EIS) measurement was carried out in the frequency range of 100 mHz–10 MHz. The specific capacitances (C_{sp}) of PACN composites at different scan rates were calculated by using Equation (1) [27]:

$$C_{sp} = \frac{\int I\,dV}{vmV} \tag{1}$$

where I is the response current density, V is the potential [V], v is the potential scan rate [mV/s] and

m is the mass of the PACN composite in the electrodes.

3.4. Electrical conductivity

The DC electrical conductivity of the PACN composites was measured by four probe method. The electrical conductivity of the samples was calculated with the help of Equations (2) and (3) [28]:

$$\text{Resistivity } (\rho) \ [\Omega \cdot \text{cm}] = \frac{\pi t}{In \cdot 2 \dfrac{V}{I}} \tag{2}$$

$$\text{Conductivity } (\sigma) \ [\text{S} \cdot \text{cm}^{-1}] = \frac{1}{\rho} \tag{3}$$

where *V* is the measured voltage, *I* is the applied current. The thickness of the samples is represented by *t*. Minimum of five tests were performed for each specimen and the data was averaged.

The frequency dependent AC conductivity of the PACN composites (disc type sample with thickness 0.3 cm and area $1.88 \cdot 10^{-1}$ cm^2) were obtained using a computer controlled precision impedance analyzer (Agilent 4294A) by applying an alternating electric field (amplitude 1000 volt) across the sample cell in the frequency region of 50 Hz to 1 MHz. A parallel plate configuration was used for all the electrical measurements. A sample holder using Pt probe was used for all the electrical measurements.

The parameters like dielectric permittivity (ε') and dielectric loss tangent ($\tan \delta$) were obtained as a function of frequency. The AC conductivity (σ_{ac}) was calculated from the dielectric data using the Equation (4):

$$\sigma_{ac} = \omega \varepsilon_0 \varepsilon' \tan \delta \tag{4}$$

where ω is equal to $2\pi f$ (*f* is the frequency), and ε_0 is vacuum permittivity. The dielectric permittivity (ε') was determined with Equation (5):

$$\varepsilon' = \frac{C_p}{C_0} \tag{5}$$

where C_p is the observed capacitance of the sample (in parallel mode), and C_0 is the capacitance of the cell. The value of C_0 was calculated using the area (*A*) and thickness (*d*) of the sample, following the Equation (6):

$$C_0 \approx \frac{\varepsilon_0 \cdot A}{d} \tag{6}$$

4. Results and discussion
4.1. Electrochemical analysis
4.1.1. Cyclic voltammetry (CV) analysis

Figure 1a shows the plot of capacitive performances for PACN composites at different scan rates (5, 10, 20, 30, 50, 60, 80 and 100 mV/s) in a three-electrode configuration with applied potential. The capacitive performance was characterized by cyclic voltammetry (CV) in 1 (M) KCl solution to obtain the value of specific capacitance (C_{sp}) of the composites. The cathodic reduction and the anodic oxidation process are the reason behind the development of negative and positive current in the cyclic voltammogram. In general, the ideal capacitor behavior of the composites was shown when ideal rectangular shape of the cyclic voltamogram was observed. However, PACN composite shows deviation of the ideality of the curve in Figure 1a which concludes its pseudo-capacitive nature. The reason behind the deviation from the ideality of the curve is that the interaction between electrode and electrolyte is reduced [29]. The specific capacitance of the PACN composites can be estimated using Equation (1) [27], the obtained specific capacitance value of PACN composite is ≈ 834 F/g at a constant scan rate of 5 mV/s. This high specific capacitance value of the PACN composites was obtained due to the contributions of both components such as PANI and CNH in the composites. In the PACN composites, PANI coated CNH increased the intimate interaction between them (PANI and CNH) that facilitate to enhance the charge transfer among the components with high electrical conductivity. Thus, the effective charge transfers in the electrode takes part a crucial role to enhance the specific capacitance value as well as rate capability of the composites [30, 31]. The well-ordered nanostructure in the PACN composites can reduce the ionic diffusion path, facilitate ionic motion to the inner part, and improve utilization of electrode materials. Effective anchoring of the CNH on the PANI helps for easy and fast ion transport in the electrode material and increases the capacitance value of the composites. Moreover, the additional Faradaic charge transfer involved at the electrode-electrolyte interface in the presence of CNH which also plays a key role to enhance the specific capacitance value in the PACN composites. Figure 1b shows the capacitive performances plot for pure PANI. The specific capacitance value for pure PANI is ≈ 231 F/g at 5 mV/s and Figure 1c shows specific
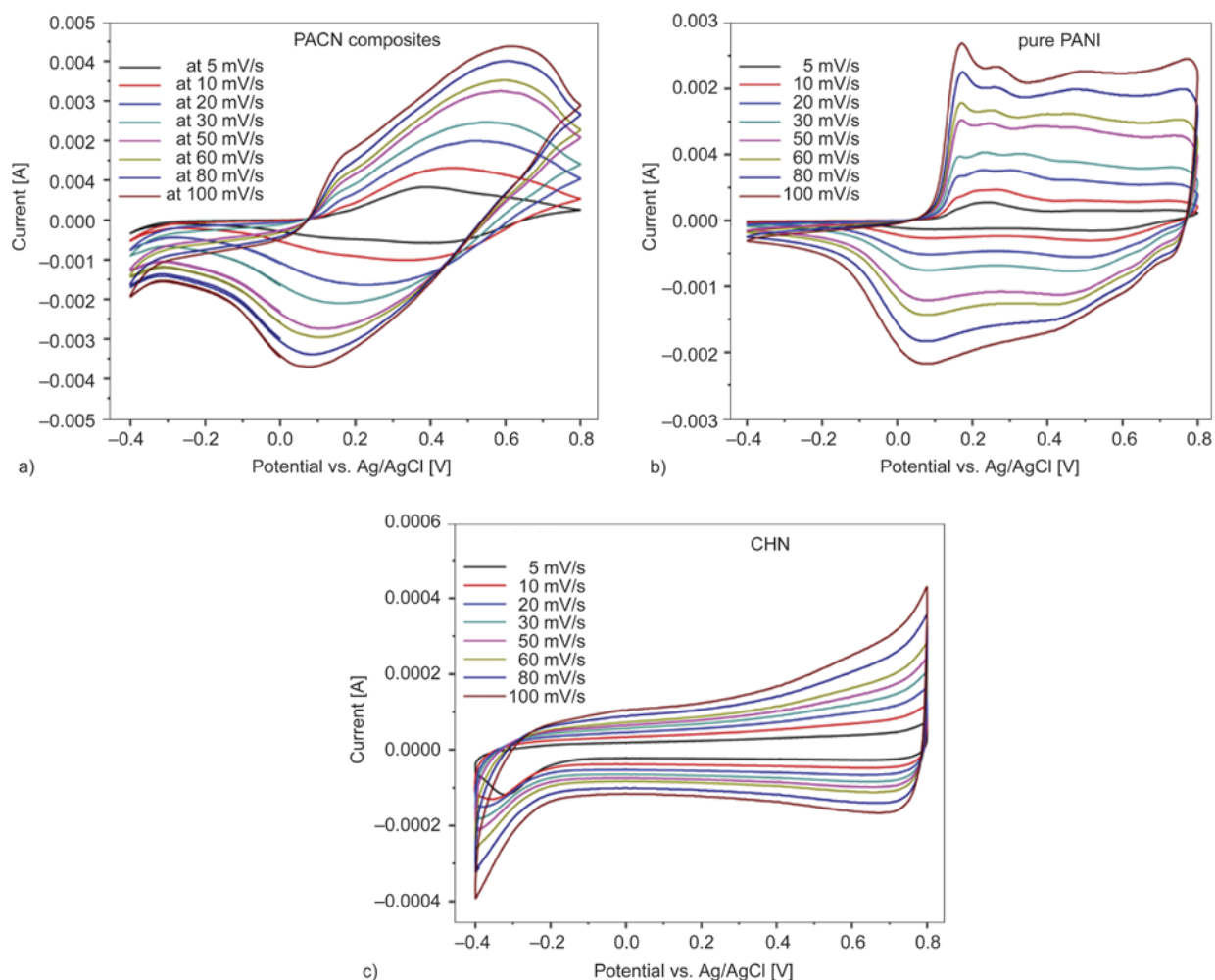
Figure 1. Cyclic voltammogram of (a) PACN composites, (b) pure PANI and (c) CNH at different scan rates

capacitance curve of CNH and capacitance value of ≈ 145 F/g was obtained at same scan rate of 5 mV/s for CNH. Many researchers [32, 33] have reported that the capacitance value of the composites can increase due to the deposition of metal oxides or metal salts [RuO$_2$ or Ni(OH)$_2$] on reduced graphene oxide (RGO) sheets or by preparing thin films of PANI fibers and RGO sheets [34]. This high capacitance value of the composites is obtained due to contributions of the conducting RGO sheets and the pseudo-capacitance of the metal oxides or conducting polymer.

Figure 2 shows the variation of specific capacitance of the PACN composites and pure PANI with scan rate. Cyclic voltammetry of the PACN composites and pure PANI was done at various scan rates of 5, 10, 20, 30, 50, 60, 80 and 100 mV/s. From the figure, it is clearly seen that the specific capacitance value of the PACN composites and PANI strongly depends on the scan rate and it decreases with increasing the scan rate [2]. As can be seen, the spe-
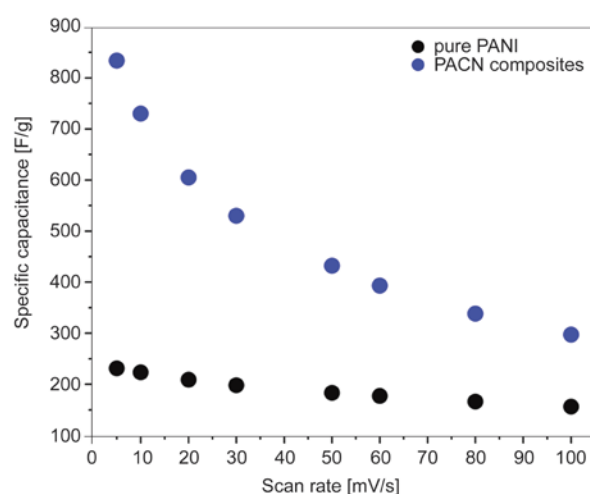
Figure 2. Plot of Specific capacitance vs. Scan rate for PACN composites and pure PANI

cific capacitance of the composites strongly depends on the scan rate and it gradually decreases for the PACN composites at a higher scan rate, as shown in Figure 2. At high scan rate, high diffusion resistance and large electrochemical polarization affect the

electrode material which reduced the capacitive behavior of the composites [35]. This suggested the high degree of sustainability of capacitance even at a higher scan rate. The coating of PANI on CNH increases the π-π stacking interaction between CNH and PANI chains, which may facilitate the electron transfer and plays a synergistic effect to the electrochemical properties of the hybrid composites [36]. This may be attributed to decreasing internal resistance as compared to the PANI electrode.

4.1.2. Constant current charging/discharging (CCD) analysis

The constant current charging/discharging (CCD) analysis of the PACN composites is shown in Figure 3 which is performed at a constant current density of 5 A/g. A triangular shaped symmetric charge/discharge curve is obtained for PACN composites which unambiguously indicate the ideal capacitive behavior of the composites. The specific capacitance (C_{sp}) value of the PACN composites was calculated from the CCD curve using Equation (7) [37]:

$$C_{sp} = \frac{I \cdot \Delta t}{\Delta V \cdot m} \qquad (7)$$

where I represents applied current, ΔV signifies the voltage and Δt stands for average time in seconds and m is the mass of the PACN composites, respectively. Thus, the calculated specific capacitance value of the PACN composites is ≈ 857 F/g.
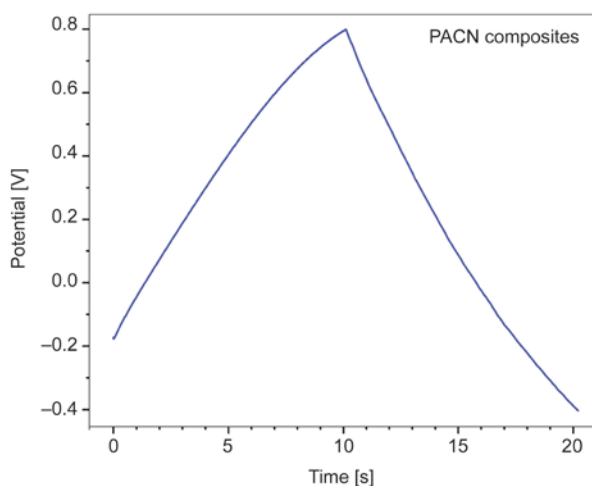
Figure 3. Cyclic charge/discharge curve of PACN composites

4.1.3. Cycle-life stability test

The variation of specific capacitance of PACN composites with cycle number is shown in Figure 4. The cycle stability of the composites has been estimated through repeating the cyclic voltammetry (CV) in 1 (M) KCl electrolyte and it is carried out at a scan rate of 10 mV/s for 500 cycles. As observed, the PACN composites remain 84% specific capacitance value after 500 cycles. In addition, the specific capacitance value of the PACN composites gradually decreases with increasing cycle number. Cho *et al.* also studied the electrochemical performance of PANI thin films. They have also measured the cyclic stability up to 500 cycles [38]. The π-π interaction and intermolecular interaction among the PANI and CNH resist the changing of regular network structure in the PACN composites and help to improve the cyclic stability of PACN composites. Thus, the regular network structure plays a key role in the PACN composites for enhancing the cyclic stability.
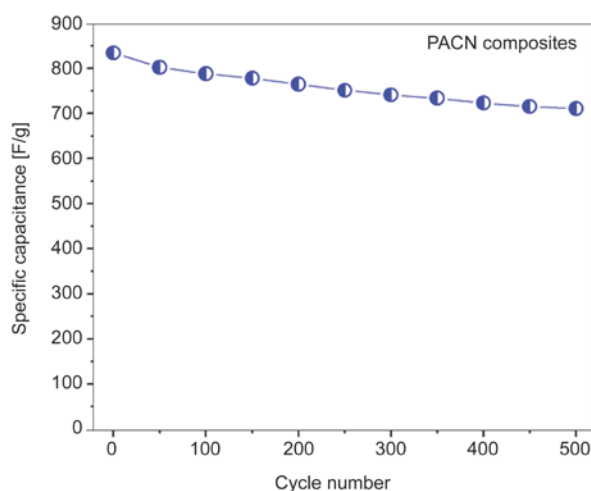

Figure 4. Specific capacitance vs. cycle number of PACN composites in 1 (M) KCl solution

4.1.4. Electrochemical impedance spectroscopic (EIS) analysis

The Nyquist plot of impedance and their fitting circuit for the PACN composites are shown in Figure 5. The electrochemical impedance behavior of the composites is known from the Nyquist plot of impedance which is performed in the frequency region from 100 mHz to 10 MHz (Figure 5a). The Nyquist plot of impedance represents two components, one

is the real component (Z') and other is imaginary component (Z''). The real component (Z') of the composites gives ohmic properties and the imaginary component (Z'') stands for the capacitive properties [39]. An ideal supercapacitor will show three frequency dependent regions in the Nyquist plot [40]. The supercapacitor behaves like a pure resistor at high frequency region. At medium frequency region, the electrode porosities can be observed. The electrolyte penetrates deeper and deeper into the porous structure of the electrode for decreasing the frequency from the very high frequency region and resulted a huge numbers of electrode surface for ion adsorption. The medium frequency region in the Nyquist plot of impedance is well known as Warburg curve. The low frequency region of the Nyquist plot shows the pure capacitive behavior. At low frequency region, the imaginary part sharply increases and a vertical line is obtained. However, ideal supercapacitor in real world is impossible. Solution resistance (R_s) of the composites can be obtained from the intercepts in highest frequency of the curves at real axis. The depressed semicircle at the higher frequency region in the Nyquist plots indicates the charge transfer resistance (R_{ct}). Warburg resistance (W) of the composites is observed at intermediate frequency region. Generally, the constant phase element (CPE) is used to express the non-ideal behavior of the supercapacitor and it is denoted by 'n'
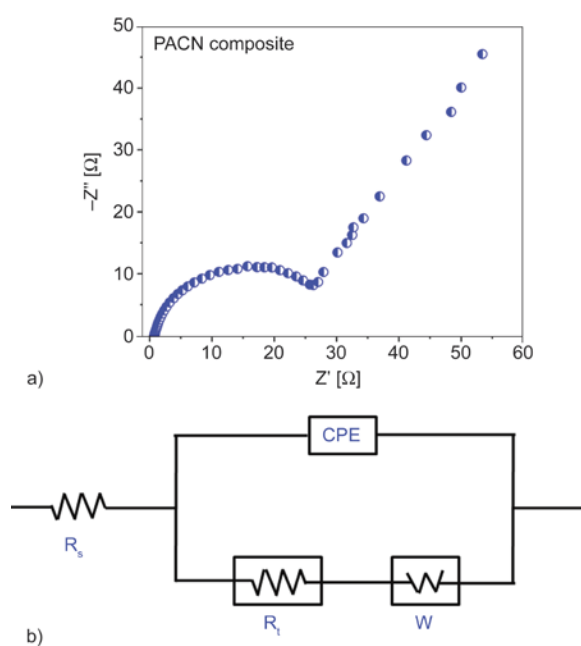
value [41]. The Nyquist plots were analyzed by fitting the experimental impedance spectra to an equivalent electrical circuit. Thus, Figure 5b shows a suitable fitting circuit for PACN composites which is schematically drawn. As observed, semicircle is seen at high frequency region and a straight line is shown at the low frequency range. The π-π interaction among the PANI and CNH plays a crucial role to help for efficient electrolyte accessibility to the electrode surface through shortening the ion diffusion path. The observed vertical line at low frequency region indicates the good capacitive behavior and low diffusion resistance of the electrode material. The quality of the electrode materials strongly depends on the 'n' value. The supercapacitor will be called ideal when n value will be equal to 1. If 'n' value is zero, then it will be called insulators. In the case of PACN composites, obtained n value is 0.83 (>0.5) which indicates the moderate capacitor behavior.

4.2. Morphology study

Figure 6 shows the morphology of the pure PANI, CNH and PACN composites. Figure 6a represents the FESEM image of PANI which indicates the fiber like structure of the PANI. The FESEM image of the CNH is shown in Figure 6b. From this image (Figure 6b), the flower like image of CNH is clearly seen. Figure 6c and 6d indicate the high magnification FESEM images of PACN composites. From these images, fiber like structure of PACN composites is clearly observed where CNH is coated with the PANI. This provides more active sites for nucleation and electron transfer path and helps to increase the π-π interaction with PANI in the composites. Thus, the specific capacitance of the PACN composites is enhanced due to the successful coating of CNH and formation of fiber like PACN composites. Figure 6e and 6f indicate the HRTEM images of PACN composites at different magnifications. Figure 6e indicates the formation of PANI-coated fiber like structure of CNH in PACN composites. The successful coating of CNH is clearly observed in Figure 6f. Thus, the fiber like structure of the composites plays a crucial role to improve the specific capacitance value of the PACN composites. From the both FESEM and HRTEM images, it is clearly seen that CNH are homogeneously dispersed and formed a conducting network path in the composites which is also responsible for the higher specific capacitance

Figure 5. Nyquist plot (a) and equivalent electrical circuit (b) used in EIS fitting data of PACN composites
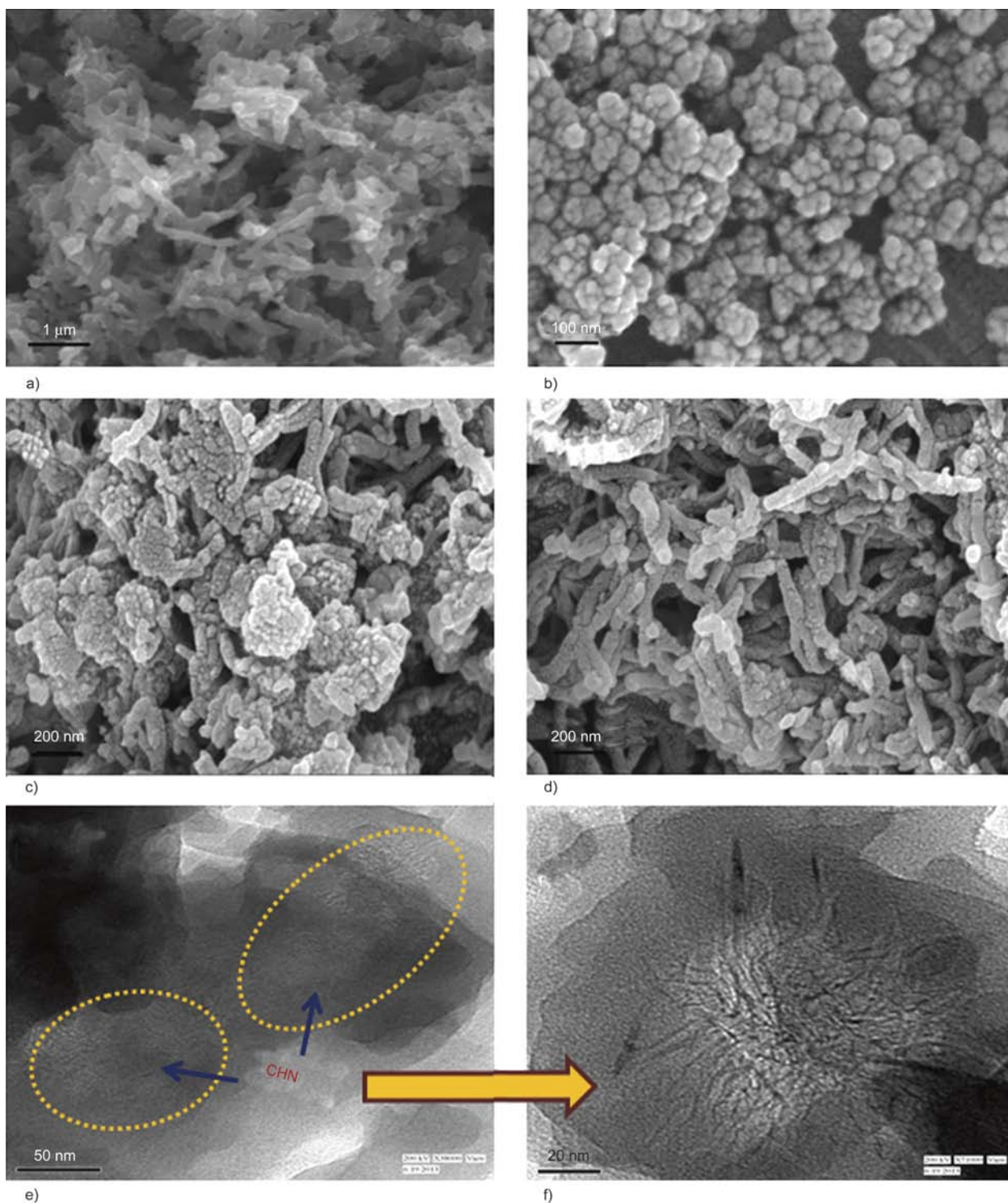
Figure 6. FESEM micrographs of (a) pure PANI, (b) pure CNH and (c, d) PACN composites at two different magnifications. HRTEM micrographs of (e, f) of PACN composites at two different magnifications

value as well as conducting behavior of the PACN composites.

4.3. Comparative study
Several researchers have already reported the specific capacitance values for different composites based on PANI or other composites. Feng *et al.* [42]

have obtained specific capacitance value of ≈ 640 F/g for PANI/graphene composites films which were synthesized through *in-situ* polymerization of aniline in the presence of graphite oxide (GO). The composites show 90% retention life after 1000 charge/discharge cycles. Wang *et al.* [43] have synthesized PANI/flexible graphene hybrid materials via *in-situ*

polymerization-reduction/dedoping-redoping process. The reported specific capacitance value of the composites was ≈ 1126 F/g. Li *et al.* [44] have prepared PANI nanofiber/graphene nanosheets composites through *in-situ* polymerization in 1 (M) H$_2$SO$_4$ solution. The composites show specific capacitance value of ≈ 1130 F/g at 5 mV/s scan rate with retention of 87% specific capacitance after 1000 harge/discharge processes. Liu *et al.* [45] have achieved the specific capacitance value of ≈ 301 F/g for PANI nanofibers/ flexible graphene sheet composites. Zhang *et al.* [46] has synthesized PANI doped graphene composites and reported value of specific capacitance was ≈ 480 F/g at current density of 0.1 A/g. Wang *et al.* [47] have reported gravimetric capacitance of ≈ 233 F/g and volumetric capacitance of ≈ 135 F/cm^3 for PANI/flexible graphene composites. The composites have been synthesized by *in-situ* electropolymerization method. Sahoo *et al.* [48] have synthesized polypyrrole (PPy) nanofiber/graphene composites through *in-situ* polymerization and obtained specific capacitance value of the composites was ≈ 466 F/g at 10 mV/s scan rate. Hu *et al.* [49] have synthesized highly porous nanorod-PANI/graphene composites films through *in-situ* electrochemical polymerization method. They have obtained specific capacitance value of ≈ 878.57 F/g at a current density of 1 A/g. Yan *et al.* [50] have achieved specific capacitance of ≈ 637 F/g at 2 mV/s scan rate for MnO$_2$ based composites which was prepared through coating of amorphous MnO$_2$ onto crystalline SnO$_2$ nanowires, grown on stainless steel substrate. Cong *et al.* [51] have synthesized PANI nanorods/flexible graphene composites papers through *in-situ* electropolymerization technique. Thus, prepared PANI nanorods/flexible graphene composites show specific capacitance value of ≈ 763 F/g with good cycling stability. Feng *et al.* [52] prepared MnO$_2$/ graphene composites by hydrothermal method and reported specific capacitance of ≈ 516.8 F/g at a scan rate of 1 mV/s. Fan *et al.* [53] synthesized polyaniline hollow spheres (PANI-HS) electrochemically reduced graphene oxide (ERGO) hybrids with core-shell structures through solution-based co-assembly process. The specific capacitance of hybrid composites was ≈ 614 F/g at a current density of 1 A/g. Qian *et al.* [54] prepared CNT/PPy core/shell composites via π–π interaction. The reported specific capacitance of the composites was ≈ 276.3 F/g at current density of 1 A/g. Chang *et al.* [55] have syn-

thesized PANI/MWCNT nanocomposites films using fresh plant leaves as a template through the nanocasting technique. The obtained specific capacitance of the nanocomposites was ≈ 535 F/g at a current density of 1 A/g for 5 wt% MWCNT loading. In our study, we have achieved high specific capacitance value of ≈ 834 F/g for PACN composites at 5 mV/s scan rate compared to most of the above reported methods.

4.4. Electrical properties
4.4.1. DC electrical conductivity
The PACN composites show high DC electrical conductivity (σ_{DC}) in the order of ≈ 6.7·10^{-2} S/cm. This very high electrical conductivity of the composites can be explained considering the formation of continuous conductive interconnected network structure of CNH-CNH and CNH-PANI in the PACN composites even at exceptionally low CNH content. This high electrical conductivity of the PACN composites is well supported by high capacitance value. Generally, the electrical conduction is generated in polymer composites through tunneling of charge carriers between the conducting nanofillers. The changing of the conducting value in the conducting polymer composites occurred due to tunneling conduction [56]. The energy barrier change in the composites strongly depends on the nature of the matrix polymer and the fabrication method. The current in a tunnel junction varied with the barrier width and exponentially decreases with it. If the nanofillers are randomly distributed in the polymer composites, then the barrier width is considered the mean average distance (d) between the conducting nanofillers and in the first approximation, it is directly proportional to the nanofillers concentration in weight, $p^{-1/3}$ [57]. So, the tunneling conductivity ($\log \sigma_{DC}$) can be expressed by Equation (8):

$$\log(\sigma_{DC}) \propto p^{-1/3} \tag{8}$$

In general, the tunneling occurs among the adjacent nanofillers in the composites. Generally, the electrons in the polymer composites cannot shift from one electrode to another electrode due to existence of high energy barrier insulating or less conductive matrix polymer. However, the energy barrier gap is reduced by applying of voltage from the source between the two electrodes which act as a driving force for the movement of electrons by tunneling con-

duction. Thus, the electrons in the composites are moved and enhanced the electrical conductivity of the composites. In addition, π-π interaction between CNH-CNH and CNH-PANI help to reduce the contact resistance and enhanced the electrical conductivity of the PACN composites.

4.4.2. AC electrical conductivity

Figure 7 shows the variation of AC electrical conductivity (σ_{AC}) with frequency (f) of the PACN composites which is measured in the frequency range of ~10^1 to ~10^6 Hz at room temperature. As observed, the value of σ_{AC} depends on the frequency and it increases with the increase in frequency. The value of σ_{AC} remains almost same up to certain frequency, known as critical frequency (f_c) and after that (above f_c), electrical conductivity suddenly increased with frequency [58, 59]. The value of σ_{AC} of any dielectric material below fc (at low frequency range) is the summation of two components and can be written by Equation (9):

$$\sigma_{AC} = \sigma_{DC} + \omega\varepsilon'' \qquad (9)$$

where σ_{DC} is the DC electrical conductivity, ω represents angular frequency which is equal to $2\pi f$ and ε'' stands for dielectric loss factor.

The σ_{DC} is the first component of the above equation which develops due to the ionic or electronic conductivity. The second component ($\omega\varepsilon''$) of the above equation varies with the extent of polarization of dipoles (induced and permanent) and accumulated interfacial charges which are well known as Maxwell-Wagner-Sillars (MWS) effect. At low frequency region (below f_c), the effect of interfacial polarization becomes more significant and the dipoles/induced dipoles get enough time to orient themselves with the direction of applied electric field. So, the value of σ_{AC} actually indicates the σ_{DC} for a conductive system at low frequency region. The polarization effect becomes insignificant at high frequency region (above f_c) and the dipoles do not get enough relaxation time to orient them in the direction of applied electric field. The applied AC electric field (periodic alternation) above f_c results in the radical reduction of space charge accumulation and dispersion of dipoles in the applied field direction that reduces the extent of polarization. Thus, the value of σ_{AC} varies strongly with the excitation of the charge particles and electrons move through the continuous interconnected conducting network path in the composites. Additionally, it can be assumed that the hopping of excited electrons through the inter particle gap (thin polymer layer) becomes easier above f_c, adding to the conductivity that already exists at low frequency in the composites.
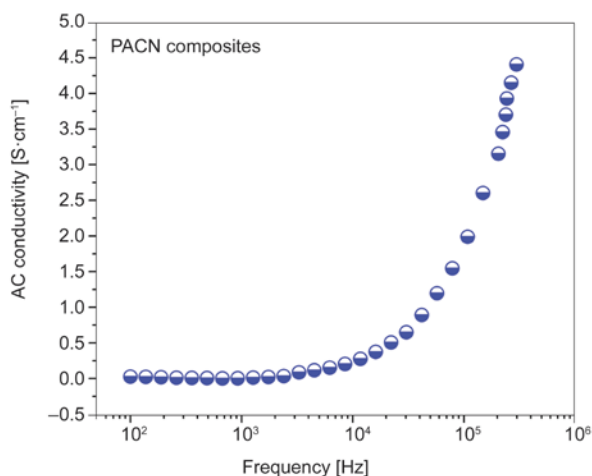
5. Conclusions

In this work, PANI coated CNH based composites (PACN) has been successfully synthesized as a supercapacitor materials by *in-situ* polymerization method. The composites show high specific capacitance value (≈ 834 F/g at 5 mV/s) compared to the pure PANI (≈ 231 F/g at 5 mV/s) and CNH (≈ 145 F/g at 5 mV/s). Thus, cost-effective and simple method for the preparation of PACN composite gives high capacitance value which is the major success of this study. The very high aspect ratio of CNH plays a crucial role to achieve high capacitance value of the composites. The π-π interaction among the electron rich phenyl rings of PANI and conducting CNH nanofiller in the PACN composites also take part to improve the specific capacitance value and the electrical conductivity of the composites than that of pure PANI. Thus, the obtained high specific capacitance value of the PACN composites indicated that this composite can be used as promising materials for supercapacitor applications. In addition, the PACN composite is electrically conductive in nature. So, it can also be used in the various conducting field of applications. The capacitive behavior, morphological study and electrical properties of the PACN composites were thoroughly characterized.

Figure 7. AC conductivity vs. frequency of the PACN composites

Acknowledgements

References

[1] Cuentas-Gallegos A. K., Lira-Cantú M., Casañ-Pastor N., Gómez-Romero P.: Nanocomposite hybrid molecular materials for application in solid-state electrochemical supercapacitors. Advanced Functional Materials, **15**, 1125–1133 (2005).
DOI: 10.1002/adfm.200400326

[2] Miller J. R., Simon P.: Electrochemical capacitors for energy management. Science, **321**, 651–652 (2008).
DOI: 10.1126/science.1158736

[3] Jang B. Z., Liu C., Neff D., Yu Z., Wang M. C., Xiong W., Zhamu A.: Graphene surface-enabled lithium ion-exchanging cells: Next-generation high-power energy storage devices. Nano Letters, **11**, 3785–3791 (2011).
DOI: 10.1021/nl2018492

[4] Kim T. Y., Lee H. W., Stoller M., Dreyer D. R., Bielawski C. W., Ruoff R. S., Suh K. S.: High-performance supercapacitors based on poly(ionic liquid)-modified graphene electrodes. ACS Nano, **5**, 436–442 (2010).
DOI: 10.1021/nn101968p

[5] Khilari S., Pandit S., Ghangrekar M. M., Pradhan D., Das D.: Graphene oxide-impregnated PVA–STA composite polymer electrolyte membrane separator for power generation in a single-chambered microbial fuel cell. Industrial and Engineering Chemistry Research, **52**, 11597–11606 (2013).
DOI: 10.1021/ie4016045

[6] Long C., Wei T., Yan J., Jiang L., Fan Z.: Supercapacitors based on graphene-supported iron nanosheets as negative electrode materials. ACS Nano, **7**, 11325–11332 (2013).
DOI: 10.1021/nn405192s

[7] Li X-G., Huang M-R., Zeng J-F., Zhu M-F.: The preparation of polyaniline waterborne latex nanoparticles and their films with anti-corrosivity and semi-conductivity. Colloids and Surfaces A: Physicochemical and Engineering Aspects, **248**, 111–120 (2004).
DOI: 10.1016/j.colsurfa.2004.08.077

[8] Huang M-R., Ding Y-B., Li X-G.: Combinatorial screening of potentiometric Pb(II) Sensors from polysulfoaminoanthraquinone solid ionophore. ACS Combinatorial Science, **16**, 128–138 (2014).
DOI: 10.1021/co400140g

[9] Huang M-R., Rao X-W., Li X-G., Ding Y-B.: Lead ion-selective electrodes based on polyphenylenediamine as unique solid ionophores. Talanta, **85**, 1575–1584 (2011).
DOI: 10.1016/j.talanta.2011.06.049

[10] Simon P., Gogotsi Y.: Materials for electrochemical capacitors. Nature Materials, **7**, 845–854 (2008).
DOI: 10.1038/nmat2297

[11] Zhang L. L., Zhao X. S.: Carbon-based materials as supercapacitor electrodes. Chemical Society Reviews, **38**, 2520–2531 (2009).
DOI: 10.1039/B813846J

[12] Chen P-C., Shen G., Shi Y., Chen H., Zhou C.: Preparation and characterization of flexible asymmetric supercapacitors based on transition-metal-oxide nanowire/single-walled carbon nanotube hybrid thin-film electrodes. ACS Nano, **4**, 4403–4411 (2010).
DOI: 10.1021/nn100856y

[13] Khilari S., Pandit S., Das D., Pradhan D.: Manganese cobaltite/polypyrrole nanocomposite-based air-cathode for sustainable power generation in the single-chambered microbial fuel cells. Biosensors and Bioelectronics, **54**, 534–540 (2014).
DOI: 10.1016/j.bios.2013.11.044

[14] Huang M-R., Ding Y-B., Li X-G.: Lead-ion potentiometric sensor based on electrically conducting microparticles of sulfonic phenylenediamine copolymer. Analyst, **138**, 3820–3829 (2013).
DOI: 10.1039/c3an00346a

[15] Li X-G., Feng H., Huang M-R., Gu G-L., Moloney M. G.: Ultrasensitive Pb(II) potentiometric sensor based on copolyaniline nanoparticles in a plasticizer-free membrane with a long lifetime. Analytical Chemistry, **84**, 134–140 (2012).
DOI: 10.1021/ac2028886

[16] Li Y., Zhao X., Xu Q., Zhang Q., Chen D.: Facile preparation and enhanced capacitance of the polyaniline/sodium alginate nanofiber network for supercapacitors. Langmuir, **27**, 6458–6463 (2011).
DOI: 10.1021/la2003063

[17] Chen D., Feng H., Li J.: Graphene oxide: Preparation, functionalization, and electrochemical applications. Chemical Reviews, **112**, 6027–6053 (2012).
DOI: 10.1021/cr300115g

[18] Lee J. W., Hall A. S., Kim J-D., Mallouk T. E.: A facile and template-free hydrothermal synthesis of Mn_3O_4 nanorods on graphene sheets for supercapacitor electrodes with long cycle stability. Chemistry of Materials, **24**, 1158–1164 (2012).
DOI: 10.1021/cm203697w

[19] Zhu S., Xu G.: Single-walled carbon nanohorns and their applications. Nanoscale, **2**, 2538–2549 (2010).
DOI: 10.1039/C0NR00387E

[20] Dai H., Zhang S., Hong Z., Li X., Xu G., Lin Y., Chen G.: Enhanced photoelectrochemical activity of a hierarchical-ordered TiO_2 mesocrystal and its sensing application on a carbon nanohorn support scaffold. Analytical Chemistry, **86**, 6418–6424 (2014).
DOI: 10.1021/ac500813u

[21] Izadi-Najafabadi A., Yamada T., Futaba D. N., Yudasaka M., Takagi H., Hatori H., Iijima S., Hata K.: High-power supercapacitor electrodes from single-walled carbon nanohorn/nanotube composite. ACS Nano, **5**, 811–819 (2011).
DOI: 10.1021/nn1017457

[22] Wu Q., Xu Y., Yao Z., Liu A., Shi G.: Supercapacitors based on flexible graphene/polyaniline nanofiber composite films. ACS Nano, **4**, 1963–1970 (2010).
DOI: 10.1021/nn1000035

[23] Deshmukh A. B., Shelke M. V.: Synthesis and electrochemical performance of a single walled carbon nanohorn–Fe_3O_4 nanocomposite supercapacitor electrode. RSC Advances, **3**, 21390–21393 (2013).
DOI: 10.1039/C3RA43079K

[24] Wang D., Wang Q., Wang T.: Morphology-controllable synthesis of cobalt oxalates and their conversion to mesoporous Co_3O_4 nanostructures for application in supercapacitors. Inorganic Chemistry, **50**, 6482–6492 (2011).
DOI: 10.1021/ic200309t

[25] Kumar N. A., Choi H-J., Shin Y. R., Chang D. W., Dai L., Baek J-B.: Polyaniline-grafted reduced graphene oxide for efficient electrochemical supercapacitors. ACS Nano, **6**, 1715–1723 (2012).
DOI: 10.1021/nn204688c

[26] Xu J., Wang K., Zu S-Z., Han B-H., Wei Z.: Hierarchical nanocomposites of polyaniline nanowire arrays on graphene oxide sheets with synergistic effect for energy storage. ACS Nano, **4**, 5019–5026 (2010).
DOI: 10.1021/nn1006539

[27] Yan J., Wei T., Shao B., Fan Z., Qian W., Zhang M., Wei F.: Preparation of a graphene nanosheet/polyaniline composite with high specific capacitance. Carbon, **48**, 487–493 (2010).
DOI: 10.1016/j.carbon.2009.09.066

[28] Bose S., Kuila T., Uddin M. E., Kim N. H., Lau A. K. T., Lee J. H.: *In-situ* synthesis and characterization of electrically conductive polypyrrole/graphene nanocomposites. Polymer, **51**, 5921–5928 (2010).
DOI: 10.1016/j.polymer.2010.10.014

[29] Meher S. K., Justin P., Rao G. R.: Microwave-mediated synthesis for improved morphology and pseudocapacitance performance of nickel oxide. ACS Applied Materials and Interfaces, **3**, 2063–2073 (2011).
DOI: 10.1021/am200294k

[30] Jung H. J., Kim Y-J., Han J. H., Yudasaka M., Iijima S., Kanoh H., Kim Y. A., Kaneko K., Yang C-M.: Thermal-treatment-induced enhancement in effective surface area of single-walled carbon nanohorns for supercapacitor application. Journal of Physical Chemistry C, **117**, 25877–25883 (2013).
DOI: 10.1021/jp405839z

[31] Dhibar S., Das C. K.: Silver nanoparticles decorated polyaniline/multiwalled carbon nanotubes nanocomposite for high-performance supercapacitor electrode. Industrial and Engineering Chemistry Research, **53**, 3495–3508 (2014).
DOI: 10.1021/ie402161e

[32] Zhao D., Guo X., Gao Y., Gao F.: An electrochemical capacitor electrode based on porous carbon spheres hybrided with polyaniline and nanoscale ruthenium oxide. ACS Applied Materials and Interfaces, **4**, 5583–5589 (2012).
DOI: 10.1021/am301484s

[33] Sun Z., Lu X.: A solid-state reaction route to anchoring $Ni(OH)_2$ nanoparticles on reduced graphene oxide sheets for supercapacitors. Industrial and Engineering Chemistry Research, **51**, 9973–9979 (2012).
DOI: 10.1021/ie202706h

[34] Gao Z., Yang W., Wang J., Wang B., Li Z., Liu Q., Zhang M., Liu L.: A new partially reduced graphene oxide nanosheet/polyaniline nanowafer hybrid as supercapacitor electrode material. Energy Fuels, **27**, 568–575 (2013).
DOI: 10.1021/ef301795g

[35] Zhang Y., Li G-Y., Lv Y., Wang L-Z., Zhang A-Q., Song Y-H., Huang B-L.: Electrochemical investigation of MnO_2 electrode material for supercapacitors. International Journal of Hydrogen Energy, **36**, 11760–11766 (2011).
DOI: 10.1016/j.ijhydene.2011.06.020

[36] Biswas S., Drzal L. T.: Multilayered nanoarchitecture of graphene nanosheets and polypyrrole nanowires for high performance supercapacitor electrodes. Chemistry of Materials, **22**, 5667–5671 (2010).
DOI: 10.1021/cm101132g

[37] Wang Y., Shi Z., Huang Y., Ma Y., Wang C., Chen M., Chen Y.: Supercapacitor devices based on graphene materials. Journal of Physical Chemistry C, **113**, 13103–13107 (2009).
DOI: 10.1021/jp902214f

[38] Cho S., Shin K-H., Jang J.: Enhanced electrochemical performance of highly porous supercapacitor electrodes based on solution processed polyaniline thin films. ACS Applied Materials and Interfaces, **5**, 9186–9193 (2013).
DOI: 10.1021/am402702y

[39] Chen W., Rakhi R. B., Hu L., Xie X., Cui Y., Alshareef H. N.: High-performance nanostructured supercapacitors on a sponge. Nano Letters, **11**, 5165–5172 (2011).
DOI: 10.1021/nl2023433

[40] Cheng Q., Tang J., Ma J., Zhang H., Shinya N., Qin L-C.: Polyaniline-coated electro-etched carbon fiber cloth electrodes for supercapacitors. Journal of Physical Chemistry C, **115**, 23584–23590 (2011).
DOI: 10.1021/jp203852p

[41] Liu J., An J., Ma Y., Li M., Ma R.: Synthesis of a graphene-polypyrrole nanotube composite and its application in supercapacitor electrode. Journal of Electrochemical Society, **159**, A828–A833 (2012).
DOI: 10.1149/2.093206jes

[42] Feng X-M., Li R-M., Ma Y-W., Chen R-F., Shi N-E., Fan Q-L., Huang W.: One-step electrochemical synthesis of graphene/polyaniline composite film and its applications. Advanced Functional Materials, **21**, 2989–2996 (2011).
DOI: 10.1002/adfm.201100038

[43] Wang H., Hao Q., Yang X., Lu L., Wang X.: A nanostructured graphene/polyaniline hybrid material for supercapacitors. Nanoscale, **2**, 2164–2170 (2010).
DOI: 10.1039/c0nr00224k

[44] Li J., Xie H., Li Y., Liu J., Li Z.: Electrochemical properties of graphene nanosheets/polyaniline nanofibers composites as electrode for supercapacitors. Journal of Power Sources, **196**, 10775–10781 (2011).
DOI: 10.1016/j.jpowsour.2011.08.105

[45] Liu S., Liu X., Li Z., Yang S., Wang J.: Fabrication of free-standing graphene/polyaniline nanofibers composite paper *via* electrostatic adsorption for electrochemical supercapacitors. New Journal of Chemistry, **35**, 369–374 (2011).
DOI: 10.1039/C0NJ00718H

[46] Zhang D., Zhang X., Chen Y., Yu P., Wang C., Ma Y.: Enhanced capacitance and rate capability of graphene/polypyrrole composite as electrode material for supercapacitors. Journal of Power Sources, **196**, 5990–5996 (2011).
DOI: 10.1016/j.jpowsour.2011.02.090

[47] Wang D-W., Li F., Zhao J., Ren W., Chen Z-G., Tan J., Wu Z-S., Gentle I., Lu G. Q., Cheng H-M.: Fabrication of graphene/polyaniline composite paper *via in situ* anodic electropolymerization for high-performance flexible electrode. ACS Nano, **3**, 1745–1752 (2009).
DOI: 10.1021/nn900297m

[48] Sahoo S., Dhibar S., Hatui G., Bhattacharya P., Das C. K.: Graphene/polypyrrole nanofiber nanocomposite as electrode material for electrochemical supercapacitor. Polymer, **54**, 1033–1042 (2013).
DOI: 10.1016/j.polymer.2012.12.042

[49] Hu L., Tu J., Jiao S., Hou J., Zhu H., Fray D. J.: *In situ* electrochemical polymerization of a nanorod-PANI–graphene composite in a reverse micelle electrolyte and its application in a supercapacitor. Physical Chemistry Chemical Physics, **14**, 15652–15656 (2012).
DOI: 10.1039/c2cp42192e

[50] Yan J., Khoo E., Sumboja A., Lee P. S.: Facile coating of manganese oxide on tin oxide nanowires with high-performance capacitive behavior. ACS Nano, **4**, 4247–4255 (2010).
DOI: 10.1021/nn100592d

[51] Cong H-P., Ren X-C., Wang P., Yu S-H.: Flexible graphene–polyaniline composite paper for high-performance supercapacitor. Energy and Environmental Science, **6**, 1185–1191 (2013).
DOI: 10.1039/C2EE24203F

[52] Feng X., Yan Z., Chen N., Zhang Y., Ma Y., Liu X., Fan Q., Wang L., Huang W.: The synthesis of shape-controlled MnO_2/graphene composites *via* a facile one-step hydrothermal method and their application in supercapacitors. Journal of Materials Chemistry A, **1**, 12818–12825 (2013).
DOI: 10.1039/C3TA12780J

[53] Fan W., Zhang C., Tjiu W. W., Pramoda K. P., He C., Liu T.: Graphene-wrapped polyaniline hollow spheres as novel hybrid electrode materials for supercapacitor applications. ACS Applied Materials and Interfaces, **5**, 3382–3391 (2013).
DOI: 10.1021/am4003827

[54] Qian T., Zhou X., Yu C., Wu S., Shen J.: Highly dispersed carbon nanotube/polypyrrole core/shell composites with improved electrochemical capacitive performance. Journal of Materials Chemistry A, **1**, 15230–15234 (2013).
DOI: 10.1039/C3TA13624H

[55] Chang C-M., Weng C-J., Chien C-M., Chuang T-L., Lee T-Y., Yeh J-M., Wei Y.: Polyaniline/carbon nanotube nanocomposite electrodes with biomimetic hierarchical structure for supercapacitors. Journal of Materials Chemistry A, **1**, 14719–14728 (2013).
DOI: 10.1039/C3TA13758A

[56] Gefen Y., Aharony A., Alexander S.: Anomalous diffusion on percolating clusters. Physical Review Letters, **50**, 77–83 (1983).
DOI: 10.1103/PhysRevLett.50.77

[57] Bello A., Laredo E., Marval J. R., Grimau M., Arnal M. L., Müller A. J.: Universality and percolation in biodegradable poly(ε-caprolactone)/multiwalled carbon nanotube nanocomposites from broad band alternating and direct current conductivity at various temperatures. Macromolecules, **44**, 2819–2828 (2011).
DOI: 10.1021/ma102598h

[58] Dyre J. C.: The random free-energy barrier model for ac conduction in disordered solids. Journal of Applied Physics, **64**, 2456–2468 (1988).
DOI: 10.1063/1.341681

[59] Dyre J. C., Schroder T. B.: Universality of ac conduction in disordered solids. Reviews of Modern Physics, **72**, 873–892 (2000).
DOI: 10.1103/RevModPhys.72.873

The effect of varying carboxylic-group content in reduced graphene oxides on the anticorrosive properties of PMMA/reduced graphene oxide composites

K. C. Chang[1]*, W. F. Ji*[1]*, C. W. Li*[1]*, C. H. Chang*[1]*, Y. Y. Peng*[2]*, J. M. Yeh*[1*]*, W. R. Liu*[3]

[1]Department of Chemistry, Center for Nanotechnology and Biomedical Technology at Chung-Yuan Christian University (CYCU), Chung Li, 32023 Taiwan, Republic of China
[2]Master Program in Nanotechnology and Center for Nanotechnology at CYCU, Chung Li, 32023 Taiwan, Republic of China
[3]Department of Chemical Engineering, CYCU, Chung Li, 32023 Taiwan, Republic of China

Abstract. We present comparative studies on the effect of varying the carboxylic-group content of thermally reduced graphene oxides (TRGs) on the anticorrosive properties of as-prepared poly(methyl methacrylate) (PMMA)/TRG composite (PTC) coatings. TRGs were formed from graphene oxide (GO) by thermal exfoliation. The as-prepared TRGs were then characterized using Fourier transform infrared (FTIR) spectroscopy and X-ray photoelectron spectroscopy (XPS). Subsequently, the PTC materials were prepared via a UV-curing process and then characterized using FTIR spectroscopy and transmission electron microscopy (TEM). PTC coatings containing TRGs with a higher carboxylic-group content exhibited better corrosion protection of a cold-rolled steel electrode that those with a lower carboxylic-group content. This is because the well-dispersed TRG with a higher carboxylic-group content embedded in the PMMA matrix effectively enhances the oxygen barrier properties of the PTC. This conclusion was supported by gas permeability analysis.

Keywords: polymer composites, PMMA, reduced graphene oxide, anticorrosion, XPS

1. Introduction

Graphene is a class of two-dimensional materials that consists of sp^2-bonded carbon atoms densely packed in a honeycomb crystal lattice. Recently, graphene nanosheets (GNSs) have emerged as another promising conductive carbon filler for use in polymer matrices because of their high aspect ratio, low cost, ease of production, and low resistance [1–4], along with their excellent mechanical, thermal, electrical, gas barrier, and anticorrosion properties [5–12].

To achieve high-performing graphene-polymer nancomposites, the GNSs must be homogeneously dispersed in the polymer hosts and have suitable interfacial interactions with the surrounding matrix. Graphene is not compatible with organic polymer matrices because the individual sheets of graphene tend to restack owing to their large specific surface areas; the van der Waals interactions between the interlayers of GNSs lower their effectiveness as a nanofiller for improved physical properties [2, 4]. An effective means to overcome the agglomeration and enhance the compatibility between GNSs and a polymer matrix is surface modification (i.e., functionalization) of graphene.

Poly(methyl methacrylate) (PMMA) is a nonconductive polymer that is inexpensive and available in large quantities. However, to broaden the application

---

*Corresponding author, e-mail: juiming@cycu.edu.tw

range of PMMA, its thermal stability and mechanical and electrical properties must be enhanced. One active field for PMMA application is the incorporation of nanomaterials.

Over the past decade, many reports have been published on the addition of functionalized graphene sheets (FGSs) to PMMA to impart a variety of improved physical properties [13–21]. Villar-Rodil *et al.* [16] prepared chemically reduced graphene/ PMMA by free radical solution–polymerization of methyl methacrylate (MMA) in the presence of exfoliated graphene oxide (GO). As a result, the glass transition temperature shifted by over 15°C with graphene loadings as low as 0.05 wt%, and the elastic modulus increased by 28% at just 1 wt% loading. Jang *et al.* [18] prepared conductive composites of PS/PMMA blends filled with octadecy-lamine-functionalized graphene (GE-ODA) and studied the electrical properties. Their results imply that the incorporation of GE-ODA into immiscible polymer blends is an efficient means of improving the electrical properties. In addition, there have been studies into using thermal reduction at different temperatures to obtain FGSs of varying degrees of functionalization [22]; these FGSs were subsequently added into polymer matrices of composites and the resultant electrochemical properties were investigated [23].

Recently, some studies reported the anticorrosive capabilities of composites containing graphene-based materials such as GNSs and GO [24–27]; however, there have been no reports on the addition of FGSs with different degrees of functionalization to PMMA matrices of composites and the resultant impact on the anticorrosive properties. Therefore, in this study, we present the first comparison of the anticorrosive properties of PMMA/thermally reduced graphene oxide (TRG) composite (PTC) coatings featuring TRGs with varying carboxylic-group contents. The detailed anticorrosion performance of the developed PTC coatings was evaluated using a series of electrochemical corrosion measurements. Corrosion protection studies were performed on sample-coated cold-rolled steel (CRS) immersed in a corrosive medium (3.5 wt% of aqueous sodium chloride solution).

2. Experimental section
2.1. Chemicals and instruments

Methyl methacrylate (MMA; Aldrich, 99.0%, Germany) was double-distilled prior to use. The photo-initiator, alpha-Benzyl-alpha-(dimethylamino)-4-morpholinobutyro-phenon (BDMP; Aldrich, 97.0%, Germany), was used as received. The graphene nanosheets used (SFG44-GNS) were prepared from SFG44 synthetic graphite powders (TIMCAL®, IMERYS Graphite & Carbon, USA). All reagents were of reagent grade unless otherwise stated.

Fourier transform infrared (FTIR) spectra were recorded using an FTIR spectrometer (JASCO FT/ IR-4100, Japan) at room temperature. The nanostructure of the composite materials was imaged with a JEOL-200FX transmission electron microscope (TEM, Japan). Prior to TEM analysis, the samples were prepared by microtoming injection-molded composites to 60–90 nm-thick slices using an Ultra 35° diamond knife (knife No. MC11091, DiSTOME Ltd, Switzerland) and dropping them onto 300 mesh copper TEM grids. The corrosion potential and corrosion current of sample-coated CRS electrodes were electrochemically measured using a VoltaLab 50 potentiostat/galvanostat. Electrochemical impedance spectroscopy (EIS) measurements were recorded on an AutoLab potentiostat/galvanostat electrochemical analyzer (PGSTAT302N, Netherlands). Gas permeability (O_2 permeation) experiments were performed using a GTR-31 analyzer (Yangimoto Co., Kyoto, Japan).

2.2. Synthesis of TRGs with different carboxylic-group contents

Graphene oxide (GO) derived from SFG44 synthetic graphite powders (TIMCAL®) was synthesized using a modified Hummers' method [28]: 4.0 g of synthetic graphite powder and 2.0 g of $NaNO_3$ were added to 280 mL of concentrated H_2SO_4 solution and the solution was stirred for 2 h. Then, 16 g of $KMnO_4$ was slowly added into the flask in an ice bath over 2 h. The mixture was then diluted with 400 mL of deionized water, and 5% H_2O_2 was added to the solution until the mixture became brown to ensure that $KMnO_4$ was fully reduced. The as-prepared GO slurry was re-dispersed in deionized water. Then, the mixture was washed with 0.1 M HCl

solution to remove the SO_4^{2-} ions. The GO solution was washed with distilled water to remove the residual acid until the solution pH was ~5 and then vacuum dried at 50°C. The GO powder was put into a furnace and heated at a rate of 0.5°C/min to temperatures of 300, 1000, and 1400°C under a 15% H_2/N_2 atmosphere for 2 h for thermal exfoliation. Finally, a few layers of TRGs with different carboxylic-group contents were obtained via the thermal exfoliation process at the three different temperatures (denoted TRG-300, TRG-1000, and TRG-1400, respectively).

2.3. UV-curable PTC coatings

A typical procedure for the preparation of PTC coatings with 0.5 wt% TRG containing 33, 11, and 1% carboxylic groups (denoted PTC-33, PTC-11, and PTC-1, respectively) is given as follows: First, 10 g of MMA, 0.01 g of photo-initiator, and 0.05 g of graphene were mixed via sonication and magnetically stirred for 1 and 12 h, respectively, at room temperature. After mixing, two drops of the mixture solution were spin-coated onto CRS at a speed of 1500 rpm and then irradiated with UV light (Fusion UV-curing, light intensity = 2000 mJ/cm^2) for 300 s to obtain the desired PTC coatings.

2.4. Electrochemical corrosion studies

All electrochemical corrosion measurements were performed in a double-wall jacketed cell covered with a glass plate using water that was maintained at 25±0.5°C. The open-circuit potential at the equilibrium state of the system was recorded as the corrosion potential (E_{corr} in mV versus a saturated calomel electrode (SCE)). Tafel plots were obtained by scanning the potential from –500 to 500 mV above E_{corr} at a scan rate of 10 mV/min. The corrosion current (I_{corr}) was determined by superimposing a straight line along the linear portion of the cathodic or anodic curve and extrapolating it through E_{corr}. The corrosion rate (R_{corr}, in milli-inches per year [MPY]) was calculated using Equation (1) [29]:

$$R_{corr}[\text{MPY}] = \frac{0.13 I_{corr}(\text{E.W.})}{A \cdot d} \tag{1}$$

where E.W. is the equivalent weight [g/eq.], A is the area [cm^2], and d is the density [g/cm^3].

An AutoLab potentiostat/galvanostat was used to perform the alternating current (AC) impedance spectroscopy measurements. Impedance was measured in the range of 100 kHz–100 MHz using a 1 cm×1 cm square of pure iron (area: 1 cm^2) embedded in epoxy as the working electrode, Pt as the counter electrode, and an SCE as the reference electrode. The working electrode was left in the test environment for 30 min prior to the impedance run. All experiments were conducted at room temperature and repeated at least three times to ensure the reproducibility and statistical significance of the raw data.
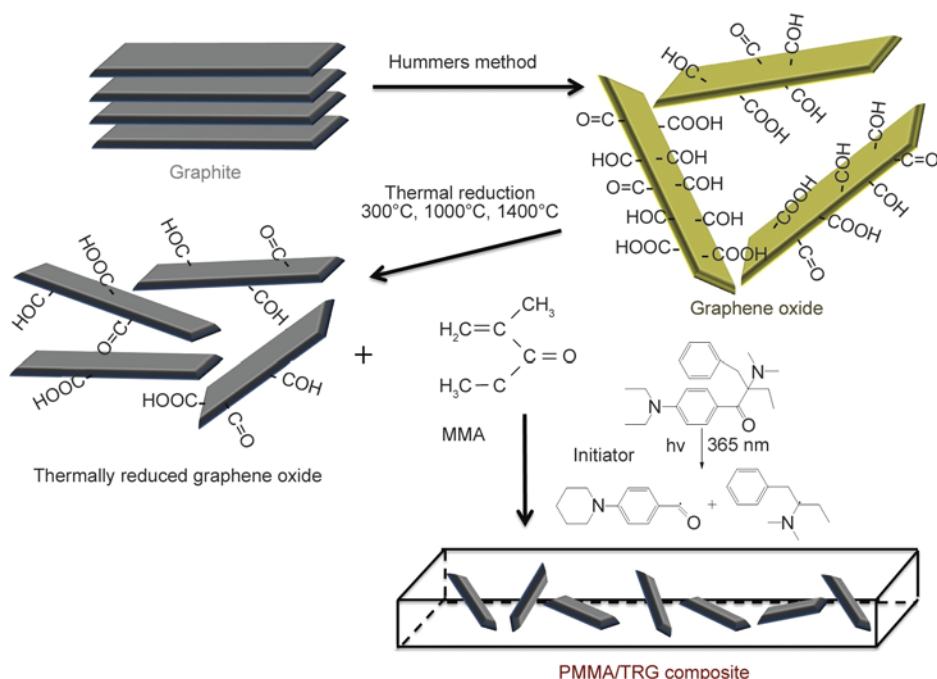

Figure 1. Preparation of PTC membranes

2.5. Preparation of membranes and molecular barrier property measurements

Membranes of the as-prepared PMMA and PTC materials were prepared to determine the oxygen barrier properties, which have been reported in literature [30, 31]. The membranes were ~90 μm thick. The typical procedure for the preparation of PTC membranes with 0.5 wt% TRG is shown in Figure 1.

3. Results and discussion

3.1. Characterization of TRGs

FTIR spectra of TRG-1400, TRG-1000, TRG-300, and GO are shown in Figure 2. GO exhibited several characteristic absorption bands. The prominent broad band at 2900–3500 cm^{-1} is assigned to hydroxyl (C–OH) and includes all vibrations from H_2O and COOH. The absorption bands that peak at 1715 and 1583 cm^{-1} correspond to C=O stretching from carboxyl and lactone and in-plane vibration of sp^2-hybridized C=C, respectively. In addition, the overlapping band at 1100–1280 cm^{-1} is attributed to the peroxide, ether, lactol, anhydride, and epoxide groups [32]. The strong absorption peak at 1045 cm^{-1} could be related to C–OH stretching and possible stretching of the C–O moiety in ether. Because GO was reduced via thermal or chemical processes, the intensities of the characteristic absorption peaks were reduced. TRG-300 showed a dramatic reduction in the intensities of the absorption bands at 3000–3500, ~1715, and 1045 cm^{-1}, indicating the loss of H_2O, COOH and C–OH. For both TRG-1000 and TRG-1400, almost no characteristic peaks were evident.
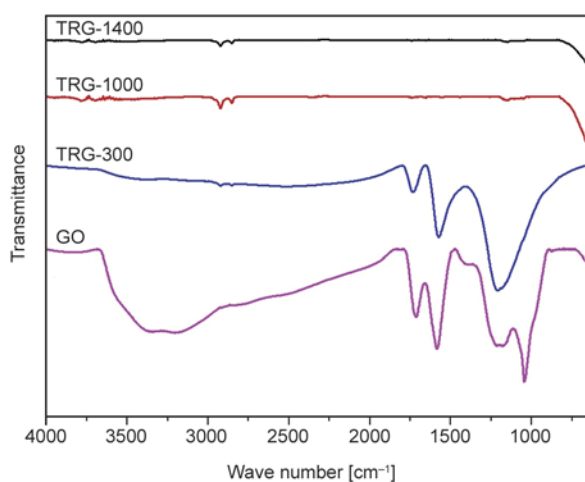

Figure 2. FTIR spectra of TRG-1400, TRG-1000, TRG-300 and GO
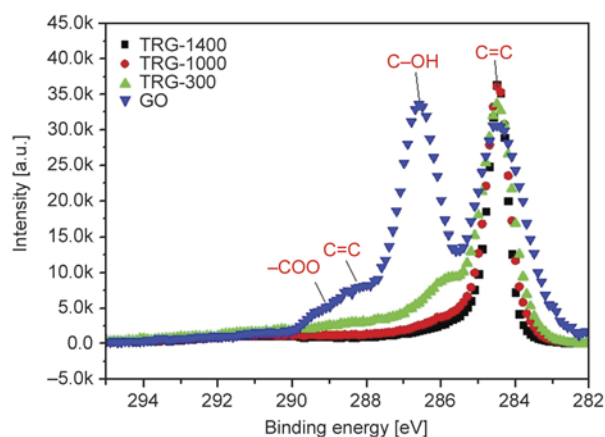

Figure 3. XPS C 1s spectra of TRG-1400, TRG-1000, TRG-300 and GO

Figure 3 shows C 1s X-ray photoelectron spectra (XPS) of TRG-300, TRG-1000, and TRG-1400. The C 1s spectra were normalized to the characteristic C=C peak at 284.5 eV. The C 1s spectrum of TRG-300 shows three peaks assigned to oxygen functional groups: C–O from phenol and ether groups at 286.1 eV, C=O from carbonyl and quinone groups at 287.5 eV, and –COO from carboxyl and ester groups at 288.7 eV. The relative intensity of the C–O peak is much larger than those of C=O and –COOH.

The contents of functionalized groups containing carbon–oxygen bonds of the TRGs were also calculated from the XPS spectra using Equation (2) [22]:

Content of functionalized groups containing carbon-oxygen bonds =

$$\frac{Area_{-C-OH} + Area_{-C=O} + Area_{-COO}}{Area_{total}} \quad (2)$$

The calculated results are shown in Table 1. With increasing reducing temperature from 300 to 1000°C, the contents of the oxygen functional groups decreased; the O/C ratio decreased from 0.25 to 0.05, as analyzed using an elemental analyzer. The analysed data are shown in Table 2. According to Gaussian-fitting quantitative analysis of the three peaks, the contents of C–O, C=O, and –COO in the TRG were 33, 15, and 7%, respectively, at 300°C and 11, 5, and 4%, respectively, at 1000°C. These results indicate that the content of C–OH functional groups is most significantly reduced at 1000°C; this might affect the dispersion of the polymer and TRG. The TRGs were also characterized using X-ray diffraction (XRD), Raman spectroscopy, scanning electron microscopy (SEM), and TEM micrographs

Table 1. The content of functionalized groups containing carbon-oxygen bonds of TRG-1400, TRG-1000, TRG-300 and GO by XPS spectrum

Sample code	Content of functionalized groups containing carbon-oxygen bonds [%]	–C=O [%]	–COO [%]	–C–OH [%]
TRG-1400	1	0	0	1
TRG-1000	20	5	4	11
TRG-300	55	15	7	33
GO	86	27	11	48

using under similar conditions as those previously reported [23, 33].

3.2. Characterization of PMMA and PTC materials

Representative FTIR absorption spectra of PMMA and PTC materials (i.e., PTC-33, PTC-11, and PTC-1) are shown in Figure 4. In the spectra of PMMA and the PTC materials, the following characteristic absorbance bands for PMMA occur: C–H stretching at 2949 cm^{-1}, C=O stretching at 1723 cm^{-1}, and C–O stretching at 1447 cm^{-1}. Moreover, comparison of the four curves reveals that there is no absorption peak that is obviously different; this is most likely because only a small amount of TRG is used [34].

The dispersion capabilities of TRGs with different carboxylic-group contents in a polymer matrix were identified and compared via TEM observation. The image at low magnification was used to determine the dispersion of TRGs in the polymer, while the high-magnification image reveals the degree of exfoliation. Figure 5 shows the TEM micrographs
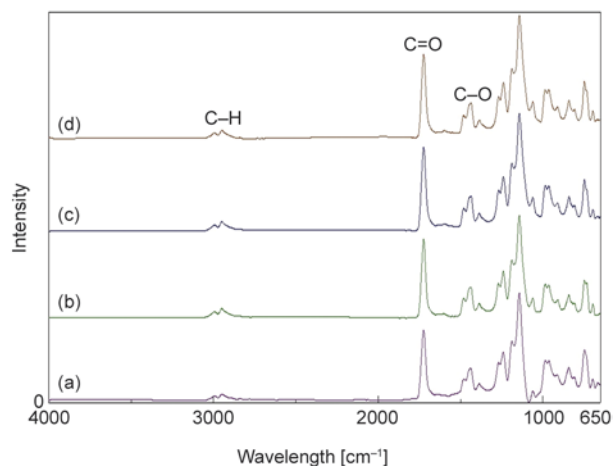
Figure 4. FTIR spectra for (a) PMMA, (b) PTC-33, (c) PTC-11 and (d) PTC-1

of the PMMA composites with 0.5 wt% TRG. Figures 5a, 5c, and 5e shows images of PTC 0.5 at low magnification (×50k), while Figures 5b, 5d, and 5f show images of the same sample at higher magnification (×200k). The gray regions of the high-magnification photograph represent the domain of the PMMA matrix and the dark lines correspond to cross sections of TRGs. As shown in Figure 5, the TEM micrograph of PTC-33 (Figure 5b) at ×50k magnification exhibits well-dispersed TRGs. However, the TEM images of PTC-11 and PTC-1 (Figures 5d and 5f) clearly show partially and fully aggregated dispersion, indicating the poor dispersion capabilities of TRGs embedded in the PMMA matrix; these results suggest that the attachment of carboxylic groups onto the TRG surface and higher carboxylic-group contents enhance the compatibility of the TRGs and PMMA matrix, resulting in improved dispersion. The greater dispersion evident in PTC-33 can also be attributed to hydrogen bonding between the remaining hydroxyl groups of TRG and the carbonyl groups of PMMA [35].

3.3. Potentiodynamic measurements

Polarization curves for PMMA and a series of PTC coatings on CRS substrates, which were recorded after 30 min immersion in 3.5 wt% of aqueous NaCl electrolyte, are illustrated in Figure 6. Tafel lines at 500 mV/min are evident in Figure 6 curves (a)–(e), which show the polarization curves for uncoated, PMMA-coated, PTC-1-coated, PTC-11-coated, and PTC-33-coated CRS electrodes, respectively. The corrosion parameters calculated from the Tafel plots for the composite materials are summarized in Table 3; generally, higher E_{corr} and polarization-resistance, R_p, values and lower I_{corr} and R_{corr} values indicate better corrosion protection. The R_p values were evaluated from the Tafel plots according to the Stearn–Geary Equation (3) [36]:

$$R_p = \frac{b_a b_c}{2.303} (b_a + b_c) I_{corr} \qquad (3)$$

where I_{corr} is determined by an intersection of the linear portions of the anodic and cathodic curves and b_a and b_c are the anodic and cathodic Tafel slopes (i.e., $\Delta E/\Delta \log I$), respectively.

The results shown in Figure 6 and Table 3 indicate that the CRS substrate coated by PMMA exhibits a higher E_{corr} value than uncoated CRS, which is consistent with the results of earlier studies [37–39].
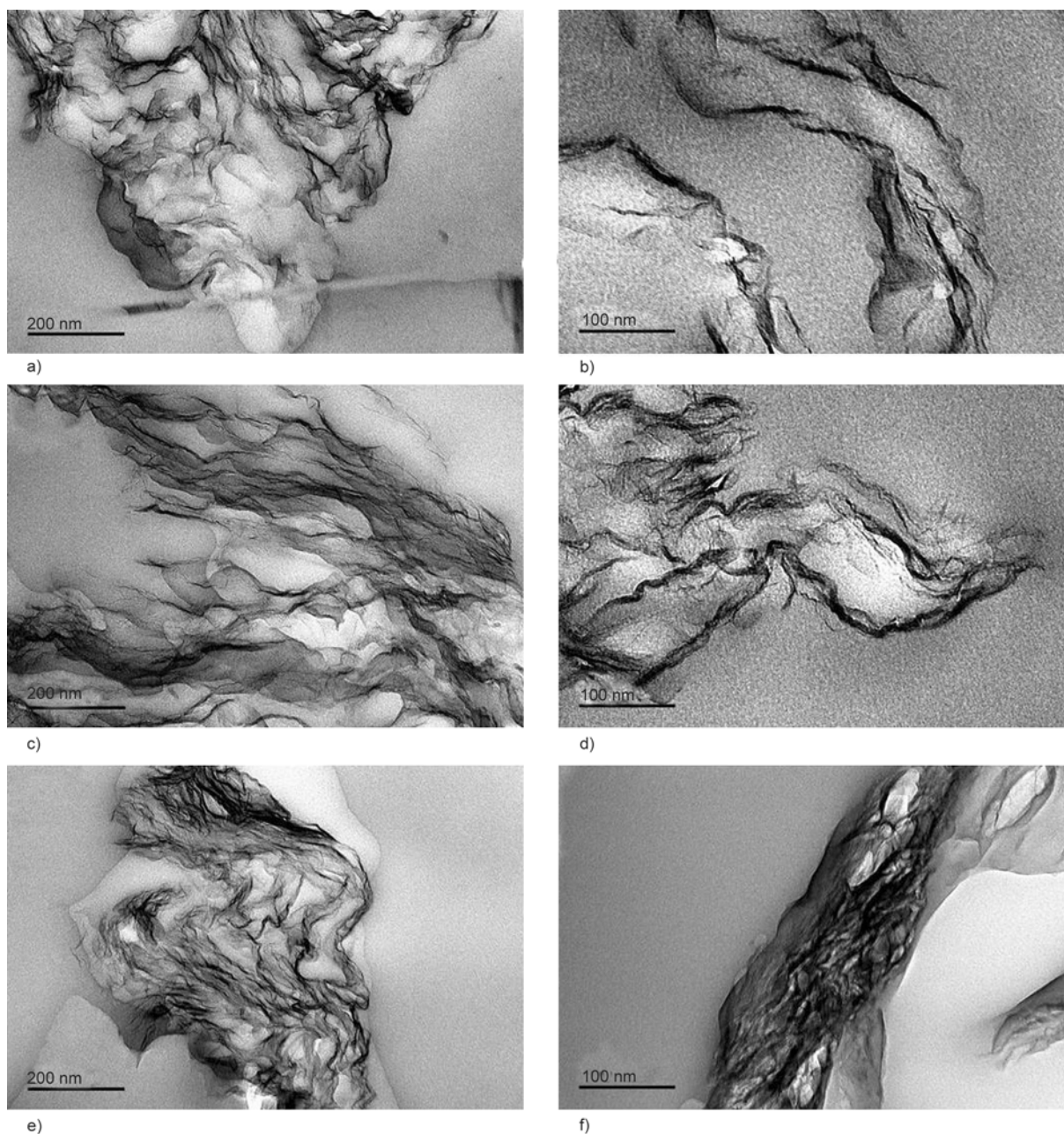
Figure 5. TEM micrographs of PTC-33, PTC-11 and PTC-1 at (a, c, e) low magnification (×50 k) and (b, d, f) high magnification (×200 k)

Table 2. The elemental analysis results of TRG-1400, TRG-1000 and TRG-300

Sample code	C [%]	O [%]	C/O
TRG-1400	95	5	0.05
TRG-1000	85	15	0.17
TRG-300	80	20	0.25

Moreover, PTC materials demonstrate higher E_{corr}, R_p, and PEF values and lower I_{corr} and R_{corr} values than PMMA. For example, PTC-33-coated CRS has an E_{corr} of –437 mV, I_{corr} of 0.23 μA/cm^2, R_p of 126.45 kΩ·cm^2, and R_{corr} of 0.21 MPY; these values are more than twice those of the PMMA-coated

specimens. Furthermore, it should be noted that the Rcorr and Icorr values of PTC-11 and PTC-1 are larger than those of PTC-33, indicating that PTC coatings with TRGs with lower carboxylic-group contents may provide reduced corrosion protection than PTC coatings with TRGs with higher carboxylic-group contents.

3.4. Electrochemical impedance measurements

Dielectric spectroscopy, which is sometimes called impedance spectroscopy or EIS, is used to measure the dielectric properties of a medium and express
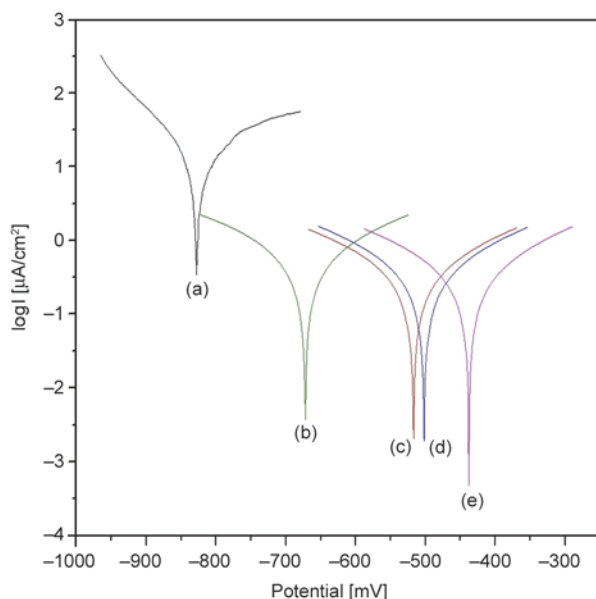
Figure 6. Tafel plots for (a) bare (b) PMMA-coated, (c) PTC-1-coated, (d) PTC-11-coated and (e) PTC-33-coated CRS electrodes measured at 25±0.5°C

them as functions of frequency [40, 41]. EIS can also be used to examine the difference in the activity of the surface of a bare CRS electrode and PMMA- or PTC-coated ones. Impedance is the result of complex resistance created when alternating current flows through a circuit made of capacitors, resistors, insulators, or any combination thereof [42]. EIS measurements give the currents produced over a wide range of frequencies via a complex nonlinear least-squares procedure that is available in numerous EIS-data–fitting computer programs; the model is ideally fitted to the experimental data in order to obtain the Randles circuit parameters. For the simulation studies, the metal corrosion is modeled with an equivalent circuit (i.e., the Randles circuit), as illustrated in Figure 7. This consists of a double-layer capacitor connected in parallel with a charge-transfer resistor and in series with an electrolyte solution resistor. The impedance (Z) depends on the charge-transfer resistance (R_{ct}), solution resistance
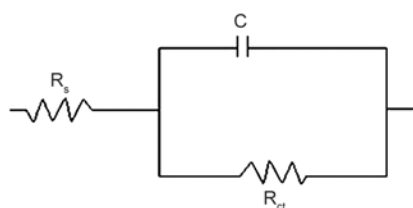
(R_s), capacitance of the electrical double-layer, and frequency of the AC signal (ω), as shown by Equation (4):

$$Z = Z' + jZ'' =$$
$$R_S + \frac{R_{ct}}{1 + (R_{ct}C_{dl}\omega)^2} + \frac{j(R_{ct}^2 C_{dl}\omega)}{1 + (R_{ct}C_{dl}\omega)^2} \quad (4)$$

The fitted data agrees well with the experimental electrochemical data. The high-frequency intercept represents the solution resistance, and the low-frequency intercept represents the sum of the solution and charge-transfer resistances [43]. In general, a higher semicircle diameter (i.e., charge transfer resistance) represents a lower corrosion rate.

Figure 8 shows the Nyquist plots of the four measured samples with sample (a) being uncoated CRS. The series of samples denoted as (b), (c), (d), and (e) represent CRS coated with PMMA, PTC-1, PTC-11, and PTC-33, respectively. The charge-transfer resistances of all the samples, as determined by subtracting the intersection of the high-frequency end from the low-frequency end of the semicircle arc with the real axis, are 2.69, 70.11, 170, 109, 164, and 619 kΩ·cm² respectively. EIS Bode plots (impedance vs. frequency) of the samples are shown in Figure 9, where Z_{real} is a measure of the corrosion resistance [44]. A low Z_{real} value is generally due to very high capacitance and/or very low resistance of the coating [45]. A large capacitance has been related to a high extent of water penetration into the coating [46]. In the Bode plots, the value of Z_{real} at the lowest frequency also represents the corrosion resistance. The Bode magnitude plots
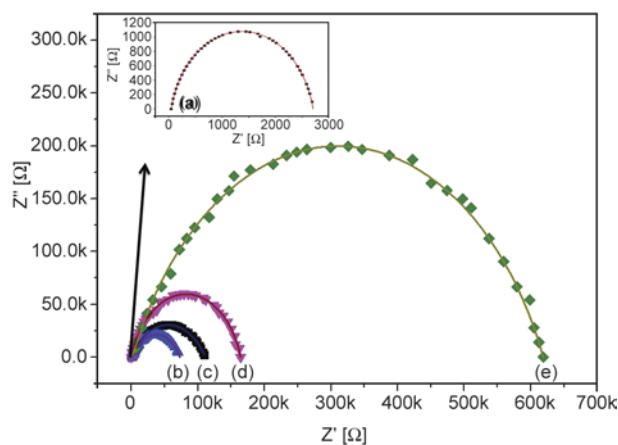

Figure 7. Randles equivalent circuit used for modeling impedance measurements (EIS)

Figure 8. Nyquist plot for (a) bare (b) PMMA-coated, (c) PTC-1-coated, (d) PTC-11-coated and (e) PTC-33-coated CRS electrodes

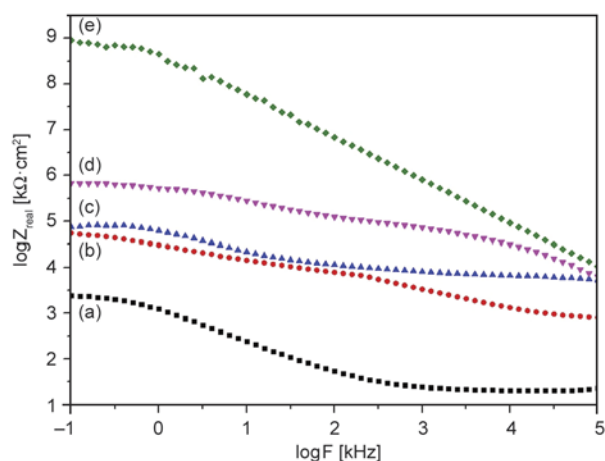**Figure 9.** Bode plot for (a) bare (b) PMMA-coated, (c) PTC-1-coated, (d) PTC-11-coated and (e) PTC-33-coated CRS electrodes

Figure 10. Schematic representation of oxygen following a tortuous path through PMMA and PTC materials

for uncoated CRS and CRS coated with PMMA, PTC-1, PTC-11, and PTC-33 show Z_{real} values of 3.4, 4.7 4.8, 5.8, and 8.9 $k\Omega\cdot cm^2$, respectively, at the low-frequency end. These results clearly demonstrate that the PTC-33 coating protected the CRS electrode against corrosion better than the PMMA, PTC-1, and PTC-11 coatings.

The electrochemical results show that the PTC-33 coating provided better protection against corrosion of the CRS electrode than the other coatings did; this is mainly attributed to good dispersion of TRG in the PMMA matrix, leading to significant barrier effects from the TRGs dispersed in the composites of the coating. The significant barrier effect of PTC-33, as compared to those of PTC-11 and PTC-1, may result from the well-dispersed TRG in the PMMA matrix more effectively increasing the tortuosity of the diffusion pathways for O_2 molecules [9, 47], as shown in Figure 10. This is evidenced by the gas permeability studies of the as-prepared membranes, as discussed in Section 3.5. In addition to the barrier effect, the higher carboxylic-group content of TRG-300 leads to the formation of stronger hydrogen bonds between the hydroxyl groups of TRG and the carbonyl groups of PMMA. Therefore, the PTC-33 coating could act as a very strong passivation layer against corrosion [24].

3.5. Gas barrier and optical clarity of PMMA and PTC membranes

The incorporation of graphene-based materials such as graphene nanoplatelets (GNPs), GNSs, and GO can significantly reduce gas permeation through a polymer composite [9, 47–50]. A percolating net-
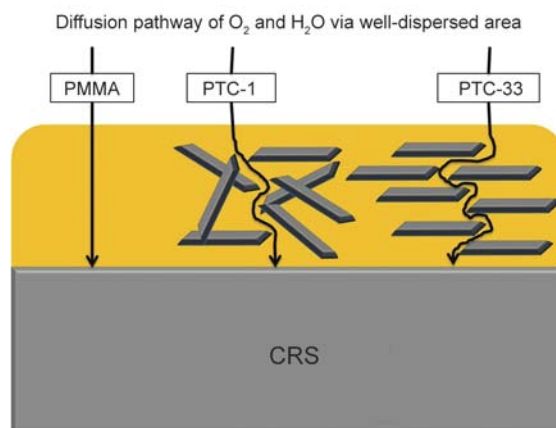
work of graphene nanoplatelets or nanosheets can increase tortuosity, which inhibits molecular diffusion through the matrix, thus resulting in significantly reduced permeability [9]. Morimune *et al*. [47] reported a 50% reduction of the gas permeability after 1% w/w incorporation of GO into PMMA. Furthermore, a nanocomposite with 10% w/w of GO was found to be almost completely impermeable.

In this study, PTC membranes with 0.5 wt% of TRG show at least a 27% reduction in O_2 permeability, compared to PMMA membranes (Figure 11 and Table 3); this is attributed to the barrier properties of the layers of TRGs dispersed in the composites. In addition, the PTC-33 membrane reduced the O_2 permeability by over 90%. As compared to the PTC-11 and PTC-1 membranes, the more significant reduction of the permeability of the PTC-33 membrane implies that better dispersion of TRGs with higher carboxylic-group contents in the PMMA matrix results in lower permeability than that of PMMA matrices with TRGs with lower car-
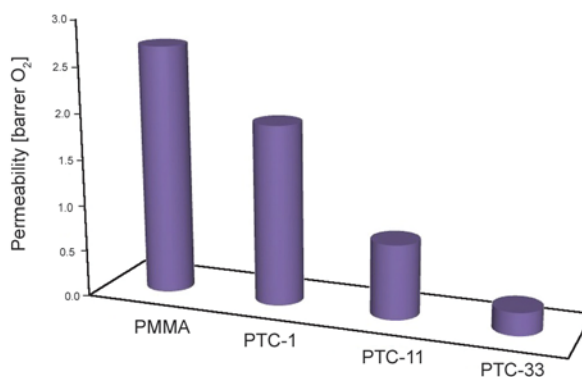

Figure 11. Gas permeability of oxygen for PMMA, PTC-1, PTC-11 and PTC-33 membranes

Table 3. Electrochemical corrosion measurements of bare CRS, PMMA, PTC-1, PTC-11 and PTC-33 coated electrodes, and gas permeability of PMMA and PTC membranes

Sample code	Electrochemical corrosion measurements[a]				Thickness [μm]	O$_2$ permeability [barrer]
	E_{corr} [mV vs SCE]	R_p [kΩ·cm^2]	I_{corr} [μA/cm^2]	Rcorr [MPY]		
CRS	−828	1.83	12.03	11.19	–	–
PMMA	-672	76.97	0.39	0.36	10±1	2.70
PTC-1	−518	120.75	0.26	0.24	10±1	1.95
PTC-11	−502	123.97	0.26	0.24	10±1	0.81
PTC-33	−437	126.45	0.23	0.21	11±1	0.25

[a]Saturated calomel electrode (SCE) was employed as a reference electrode.
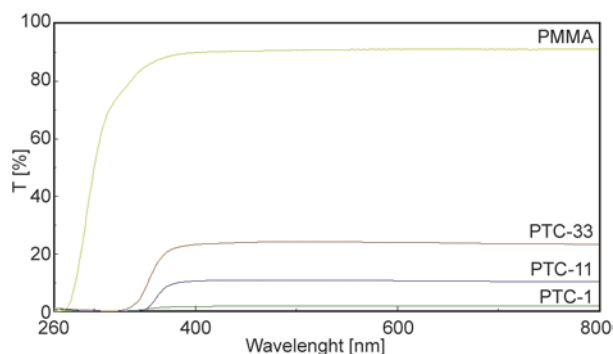
Figure 12. UV-visible transmission spectra of PMMA and PTC membranes

boxylic-group contents. This conclusion is consistent with our TEM observations.

Figure 12 shows the UV/visible transmission spectra of PMMA and PTC membranes. First, we found that the optical clarity of PMMA membrane showed high transparency. However, the spectra of PTC membranes exhibiting low transparency. Among the membrane of PTC-33 is the most transparent one. The obvious difference in the optical clarity of the PTC membranes could be associated with the different dispersion degrees and abilities of TRGs in the polymer matrix. Generally, the optical clarity of PTC membranes with a better dispersion of TRGs showed higher transparency than that of membranes with a poor dispersion in the polymer matrix. Therefore, we believe that PTC-33 had a better dispersion of TRGs than PTC-11 and PTC-1. This is consistent with the results of TEM observations.

4. Conclusions

PTC materials were successfully prepared by a UV-curing process and subsequently characterized using FTIR spectroscopy and TEM. The corrosion protection effect of PTC coatings containing TRGs was demonstrated by performing a series of potentiodynamic and impedance electrochemical meas-

urements on CRS substrates in 3.5 wt% of aqueous NaCl electrolyte. The PTC coatings with TRG containing higher carboxylic-group content exhibited better anticorrosion performance than PTC coatings with TRG containing lower carboxylic-group content. The significantly enhanced corrosion protection of PTC-33 coatings on a metallic surface is attributed to the TRG with a higher carboxylic-group content being better dispersed in the PMMA matrix, leading to a significant barrier effect from TRGs dispersed in the coating composites.

References
[1] Geim A. K., Novosolov K. S.: The rise of graphene. Nature Materials, **6**, 183–191 (2007).
DOI: 10.1038/nmat1849
[2] Loh K. P., Bao Q., Ang P. K., Yang J.: The chemistry of graphene. Journal of Materials Chemistry, **20**, 2277–2289 (2010).
DOI: 10.1039/B920539J
[3] Jang B. Z., Zhamu A.: Processing of nanographene platelets (NGPs) and NGP nanocomposites: A review. Journal of Materials Science, **43**, 5092–5101 (2008).
DOI: 10.1007/s10853-008-2755-2
[4] Zhu Y., Murali S., Cai W., Li X., Suk J. W., Potts J. R., Ruoff R. S.: Graphene and graphene oxide: Synthesis, properties, and applications. Advanced Materials, **22**, 3906–3924 (2010).
DOI: 10.1002/adma.201001068
[5] Kuilla T., Bhadra S., Yao D., Kim N. H., Bose S., Lee J. H.: Recent advances in graphene based polymer composites. Progress in Polymer Science, **35**, 1350–1375 (2010).
DOI: 10.1016/j.progpolymsci.2010.07.005

[6] Salavagione H. J., Martínez G., Ellis G.: Recent advances in the covalent modification of graphene with polymers. Macromolecular Rapid Communications, **32**, 1771–1789 (2011).
DOI: 10.1002/marc.201100527

[7] Kim H., Abdala A. A., Macosko C. W.: Graphene/polymer nanocomposites. Macromolecules, **43**, 6515–6530 (2010).
DOI: 10.1021/ma100572e

[8] Bai H., Li C., Shi G.: Functional composite materials based on chemically converted graphene. Advanced Materials, **23**, 1089–1115 (2011).
DOI: 10.1002/adma.201003753

[9] Potts J. R., Dreyer D. R., Bielawski C. W., Ruoff R. S.: Graphene-based polymer nanocomposites. Polymer, **52**, 5–25 (2011).
DOI: 10.1016/j.polymer.2010.11.042

[10] Tantis I., Psarras G. C., Tasis D.: Functionalized graphene – poly(vinyl alcohol) nanocomposites: Physical and dielectric properties. Express Polymer Letters, **6**, 283–292 (2012).
DOI: 10.3144/expresspolymlett.2012.31

[11] Singh B. P., Nayak S., Nanda K. K., Jena B. K., Bhattacharjee S., Besra L.: The production of a corrosion resistant graphene reinforced composite coating on copper by electrophoretic deposition. Carbon, **61**, 47–56 (2013).
DOI: 10.1016/j.carbon.2013.04.063

[12] Sahu S. C., Samantara A. K., Seth M., Parwaiz S., Singh B. P., Rath P. C., Jena B. K.: A facile electrochemical approach for development of highly corrosion protective coatings using graphene nanosheets. Electrochemistry Communications, **32**, 22–26 (2013).
DOI: 10.1016/j.elecom.2013.03.032

[13] Ramanathan T., Abdala A. A., Stankovich S., Dikin D. A., Herrera-Alonso M., Piner R. D., Adamson D. H., Schniepp H. C., Chen X., Ruoff R. S., Nguyen S. T., Aksay I. A., Prud'Homme R. K., Brinson L. C.: Functionalized graphene sheets for polymer nanocomposites. Nature Nanotechnology, **3**, 327–331 (2008).
DOI: 10.1038/nnano.2008.96

[14] Das B., Prasad K. E., Ramamurty U., Rao C. N. R.: Nano-indentation studies on polymer matrix composites reinforced by few-layer graphene. Nanotechnology, **20**, 125705/1–125705/5 (2009).
DOI: 10.1088/0957-4484/20/12/125705

[15] Yuan X. Y., Zou L. L., Liao C. C., Dai J. W.: Improved properties of chemically modified graphene/poly(methyl methacrylate) nanocomposites *via* a facile *in-situ* bulk polymerization. Express Polymer Letters, **6**, 847–858 (2012).
DOI: 10.3144/expresspolymlett.2012.90

[16] Villar-Rodil S., Paredes J. I., Martínez-Alonsoa A., Tascón J. M. D.: Preparation of graphene dispersions and graphene-polymer composites in organic media. Journal of Materials Chemistry, **19**, 3591–3593 (2009).
DOI: 10.1039/B904935E

[17] Potts J. R., Lee S. H., Alam T. M., An J., Stoller M. D., Piner R. D., R. Ruoff S.: Thermomechanical properties of chemically modified graphene/poly(methyl methacrylate) composites made by *in situ* polymerization. Carbon, **49**, 2615–2623 (2011).
DOI: 10.1016/j.carbon.2011.02.023

[18] Yang Y-K., He C-E., Peng R-G., Baji A., Du X-S., Huang Y-L., Xie X-L., Mai Y-W.: Non-covalently modified graphene sheets by imidazolium ionic liquids for multifunctional polymer nanocomposites. Journal of Materials Chemistry, **22**, 5666–5675 (2012).
DOI: 10.1039/C2JM16006D

[19] Mao C., Zhu Y., Jiang W.: Design of electrical conductive composites: Tuning the morphology to improve the electrical properties of graphene filled immiscible polymer blends. ACS Applied Materials and Interfaces, **4**, 5281–5286 (2012).
DOI: 10.1021/am301230q

[20] Wang J., Shi Z., Ge Y., Wang Y., Fan J., Yin J.: Solvent exfoliated graphene for reinforcement of PMMA composites prepared by *in situ* polymerization. Materials Chemistry and Physics, **136**, 43–50 (2012).
DOI: 10.1016/j.matchemphys.2012.06.017

[21] Gudarzi M. M., Sharif F.: Enhancement of dispersion and bonding of graphene-polymer through wet transfer of functionalized graphene oxide. Express Polymer Letters, **6**, 1017–1031 (2012).
DOI: 10.3144/expresspolymlett.2012.107

[22] Yang D., Velamakanni A., Bozoklu G., Park S., Stoller M., Piner R. D., Stankovich S., Jung I., Field D. A., Ventrice Jr. C. A., Ruoff R. S.: Chemical analysis of graphene oxide films after heat and chemical treatments by X-ray photoelectron and micro-Raman spectroscopy. Carbon, **47**, 145–152 (2009).
DOI: 10.1016/j.carbon.2008.09.045

[23] Kuo S-L., Liu W-R., Kuo C-P., Wu N-L., Wu H-C.: Lithium storage in reduced graphene oxides. Journal of Power Sources, **244**, 552–556 (2013).
DOI: 10.1016/j.jpowsour.2013.01.186

[24] Yu Y. H., Lin Y. Y., Lin C. H., Chan C. C., Huang Y. C.: High-performance polystyrene/graphene-based nanocomposites with excellent anti-corrosion properties. Polymer Chemistry, **5**, 535–550 (2014).
DOI: 10.1039/c3py00825h

[25] Singh B. P., Jena B. K., Bhattacharjee S., Besra L.: Development of oxidation and corrosion resistance hydrophobic graphene oxide-polymer composite coating on copper. Surface and Coatings Technology, **232**, 475–481 (2013).
DOI: 10.1016/j.surfcoat.2013.06.004

[26] Chang K. C., Hsu C. H., Lu H. I., Ji W. F., Chang C. H., Li W. Y., Chuang T. L., Yeh J. M., Liu W. R., Tsai M. H.: Advanced anticorrosive coatings prepared from electroactive polyimide/graphene nanocomposites with synergistic effects of redox catalytic capability and gas barrier properties. Express Polymer Letters, **8**, 243–255 (2014).
DOI: 10.3144/expresspolymlett.2014.28

[27] Chang K-C., Hsu M-H., Lu H-I., Lai M-C., Liu P-J., Hsu C-H., Ji W-F., Chuang T-L., Wei Y., Yeh J-M., Liu W-R.: Room-temperature cured hydrophobic epoxy/ graphene composites as corrosion inhibitor for cold-rolled steel. Carbon, **66**, 144–153 (2014). DOI: 10.1016/j.carbon.2013.08.052

[28] Hummers Jr. W. S., Offerman R. E.: Preparation of graphitic oxide. Journal of the American Chemical Society, **80**, 1339 (1958). DOI: 10.1021/ja01539a017

[29] Wei Y., Wang J., Jia X., Yeh J-M., Spellane P.: Polyaniline as corrosion protection coatings on cold rolled steel. Polymer, **36**, 4535–4537 (1995). DOI: 10.1016/0032-3861(95)96866-7

[30] Chang K-C., Lai M-C., Peng C-W., Chen Y-T., Yeh J-M., Lin C-L., Yang J-C.: Comparative studies on the corrosion protection effect of DBSA-doped polyaniline prepared from *in situ* emulsion polymerization in the presence of hydrophilic Na^+-MMT and organophilic organo-MMT clay platelets. Electrochimica Acta, **51**, 5645–5653 (2006). DOI: 10.1016/j.electacta.2006.02.039

[31] Huang K-Y., Shiu C-L., Su Y-A., Yang C-C., Yeh J-M., Wei Y., Lee K-R.: Preparation and gas transport properties of dense fluoroaniline copolymer membranes. Journal of Membrane Science, **339**, 171–176 (2009). DOI: 10.1016/j.memsci.2009.04.046

[32] Acik M., Lee G., Mattevi C., Chhowalla M., Cho K., Chabal Y. J.: Unusual infrared-absorption mechanism in thermally reduced graphene oxide. Nature Materials, **9**, 840–845 (2010). DOI: 10.1038/nmat2858

[33] Liu W-R., Kuo S-L., Lin C-Y., Chiu Y-C., Su C-Y., Wu H-C., Hsieh C-T.: Characterization and electrochemical behavior of graphene-based anode for Li-ion batteries. The Open Materials Science Journal, **5**, 236–241 (2011). DOI: 10.2174/1874088X01105010236

[34] Shi H., Li Y., Guo T.: *In situ* preparation of transparent polyimide nanocomposite with a small load of graphene oxide. Journal of Applied Polymer Science, **128**, 3163–3169 (2013). DOI: 10.1002/app.38519

[35] Pham V. H., Dang T. T., Hur S. H., Kim E. J., Chung J. S.: Highly conductive poly(methyl methacrylate) (PMMA)-reduced graphene oxide composite prepared by self-assembly of PMMA latex and graphene oxide through electrostatic interaction. ACS Applied Materials and Interfaces, **4**, 2630–2636 (2012). DOI: 10.1021/am300297j

[36] Stern M., Geary A. L.: Electrochemical polarization I . A theoretical analysis of the shape of polarization curves. Journal of the Electrochemical Society, **104**, 56–63 (1957). DOI: 10.1149/1.2428496

[37] Yeh J-M., Liou S-J., Lin C-Y., Cheng C-Y., Chang Y-W.: Anticorrosively enhanced PMMA–clay nanocomposite materials with quaternary alkylphosphonium salt as an intercalating agent. Chemistry of Materials, **14**, 154–161 (2002). DOI: 10.1021/cm010337f

[38] Chang K-C., Chen S-T., Lin H-F., Lin C-Y., Huang H-H., Yeh J-M., Yu Y-H.: Effect of clay on the corrosion protection efficiency of PMMA/Na^+-MMT clay nanocomposite coatings evaluated by electrochemical measurements. European Polymer Journal, **44**, 13–23 (2008). DOI: 10.1016/j.eurpolymj.2007.10.011

[39] Yeh J-M., Liou S-J., Lai M. C., Chang Y-W., Huang C-Y., Chen C-P., Jaw J-H., Tsai T-Y., Yu Y-H.: Comparative studies of the properties of poly(methyl methacrylate)–clay nanocomposite materials prepared by *in situ* emulsion polymerization and solution dispersion. Journal of Applied Polymer Science, **94**, 1936–1946 (2004). DOI: 10.1002/app.21095

[40] Liu Y. D., Fang F. F., Choi H. J.: Core–shell structured semiconducting PMMA/polyaniline snowman-like anisotropic microparticles and their electrorheology. Langmuir, **26**, 12849–12854 (2010). DOI: 10.1021/la101165k

[41] Liu Y. D., Park B. J., Kim Y. H., Choi H. J.: Smart monodisperse polystyrene/polyaniline core–shell structured hybrid microspheres fabricated by a controlled releasing technique and their electro-responsive characteristics. Journal of Materials Chemistry, **21**, 17396–17402 (2001). DOI: 10.1039/C1JM12443A

[42] Park S-M., Yoo J-S.: Peer reviewed: Electrochemical impedance spectroscopy for better electrochemical measurements. Analytical Chemistry, **75**, 455–461 (2003). DOI: 10.1021/ac0313973

[43] Amirudin A., Thierry D.: Application of electrochemical impedance spectroscopy to study the degradation of polymer-coated metals. Progress in Organic Coatings, **26**, 1–28 (1995). DOI: 10.1016/0300-9440(95)00581-1

[44] Zucchi F., Grassi V., Frignani A., Monticelli C., Trabanelli G.: Electrochemical behaviour of a magnesium alloy containing rare earth elements. Journal of Applied Electrochemistry, **36**, 195–204 (2006). DOI: 10.1007/s10800-005-9053-3

[45] Kannan M. B., Gomes D., Dietzel W., Abetz V.: Polyoxadiazole-based coating for corrosion protection of magnesium alloy. Surface and Coatings Technology, **202**, 4598–4601 (2008). DOI: 10.1016/j.surfcoat.2008.03.027

[46] Reinhard G., Rammelt U.: Application of electrochemical impedance spectroscopy (EIS) for characterizing the corrosion-protective performance of organic coatings on metals. Progress in Organic Coatings, **21**, 205–226 (1992). DOI: 10.1016/0033-0655(92)87005-U

[47] Morimune S., Nishino T., Goto T.: Ecological approach to graphene oxide reinforced poly(methyl methacrylate) nanocomposites. ACS Applied Materials and Interfaces, **4**, 3596–3601 (2012).
DOI: 10.1021/am3006687

[48] Compton O. C., Kim S., Pierre C., Torkelson J. M., Nguyen S. B. T.: Crumpled graphene nanosheets as highly effective barrier property enhancers. Advanced Materials, **22**, 4759–4763 (2010).
DOI: 10.1002/adma.201000960

[49] Kim H., Miura Y., Macosko C. W.: Graphene/polyurethane nanocomposites for improved gas barrier and electrical conductivity. Chemistry of Materials, **22**, 3441–3450 (2010).
DOI: 10.1021/cm100477v

[50] Kalaitzidou K., Fukushima H., Drzal L. T.: Multifunctional polypropylene composites produced by incorporation of exfoliated graphite nanoplatelets. Carbon, **45**, 1446–1452 (2007).
DOI: 10.1016/j.carbon.2007.03.029

The effect of the prismatic filler arrangement and cross-sectional shape on the thermal conductivity of polymer composites

X. J. Wang[*]

School of Chemistry and Biological Engineering, Lanzhou Jiaotong University, Lanzhou, Gansu 730070, China

Abstract. Incorporation of fillers with high thermal conductivity to base materials has been recognized as an efficient way to increase the thermal conductivity of composite materials. In this study, the effects of the prismatic filler arrangement and cross-sectional shape on the thermal conductivity of the composites were investigated. This research addresses these problems by solving the heterogeneous two-dimensional heat conduction problem in the composite materials. A validated commercial software-FLUENT and finite volume method was used in the analysis. The close-packed, directional and random filler arrangements were considered. It was found that the prismatic filler arrangement and cross-sectional shape have great impacts on the thermal conductivity of the composite materials. Double Y shaped, I shaped, T shaped, elliptical, rhombic and rectangular cross-sectional fillers can greatly increase the thermal conductivity only in directional arrangement. The effects of circular, square, triangular and Y shaped cross-sectional are similar in directional and random arrangements. The close-packed arrangements for all cross-sectional shapes have small thermal conductivity. The double Y shaped, Y shaped and I shaped cross-sectional were found to be the best choice for composite materials regardless of the filler arrangements.

Keywords: polymer composites, thermal conductivity, directional arrangement, close-packed arrangement, filler shapes

1. Introduction

Thermal management devices such as heat exchangers and heat sinks are the key equipments in various industries like air-conditioning, refrigeration, energy-recovery, electronic communication and so on [1–3]. The performance of a heat exchanger is often important to the overall efficiency, cost and size of the system. Conventional heat exchangers are mainly made of monolithic metals and metal alloys. Metals are applied extensively. Regretfully, metallic heat exchangers cannot operate at acid environments for extended periods of time, and the thermal shock shortens their operation life [4]. To solve this problem, plastics or polymers instead of metals have been used to make heat exchangers [5–7]. However, the thermal conductivity of polymers is very low,

that makes the overall heat transfer coefficients of plastic heat exchangers very low. The consequence is that a larger heat transfer area is required to offset this shortcoming, which makes the polymer heat exchanger very bulky [8].

It has been recognized that adding fillers of high conductivity to the base polymers is an efficient method to increase the thermal conductivity of the base polymer. Many kinds of thermal conductive fillers are introduced into the composites, such as alumina, aluminum nitride, boron nitride, graphite and carbon nanotube [9–11]. In this way, thermal conductivity of polymers is increased while their virtue can be largely kept.

The filler content and its thermal conductivity were reported to be the two dominant factors influencing

the overall thermal conductivity of polymer composites. Previous work and various correlations were mainly focused on these two respects [12–24]. These studies only considered simple filler shapes with uniform filler arrangement [25–29]. Relatively little attention has been paid to the effects of other typical filler arrangements and filler shapes. It is believed that the thermal conductivity of the composite materials is not a simple mixing between the fillers and base materials. Rather, filler's arrangement and shape would have great impacts on the final thermal conductivity of composite materials. The effects of three typical prismatic filler arrangements and ten filler cross-sectional shapes would be investigated in this study. A representing micro cell comprising of fillers and a base material was selected. The heat transfer between fillers and the base materials was modeled by a two-dimensional heat conduction model. Then it was used to reflect the effects of prismatic filler arrangements and cross-sectional shapes. This is the novelty of this study.

2. Numerical work
2.1. Generation of unit cell model
To make the calculation of numerical models easy, a two-dimensional elementary cell comprising of fillers in the base polymer material is considered. The cell is small and convenient for calculations, but large enough to represent a periodic section in the material. The fillers are arranged in the base materials with no contact each other. This is true when the filler content is below 20%. When the fillers are contacting together, the mechanical strength of the composite materials will be seriously deteriorated [30]. The effect of interfacial thermal resistance is very inconspicuous, when filler size greater than 1 μm. At room temperatures, its effect is very small, and the particle size will have to be in the nanoscale range for the effect to be significant [39]. We discuss the effects of macroscopic filler shapes and arrangements, and the interfacial thermal resistance between fillers and matrix can be ignored in this study. The areas of cross-sections of fillers studied are around 0.25 mm² each. The cell selected here is a 1×1 cm² and has a dozen of fillers, represents a periodic section in the composite material. The fillers may have different shapes and orientation angles on the two-dimensional surface. Table 1 lists ten cross-sectional shapes of the fillers considered in this study:

circular, square, equilateral triangular, rhombic, elliptical, rectangular, T shaped, I shaped, Y shaped and double Y shaped. They are artificially designed, to evaluate the effects of filler arrangement and filler shape. They can be orient freely on the *x*-*y* plane (Figure 1). In the table, their orientation angles are defined as 0° when the filler cross-sectional main axis (the vertical axis) overlaps with the heat flux direction.

Three typical filler arrangements are considered in this study. (1) Close-packed arrangement, in which all the fillers are close-packed in the central of polymer matrix with 0° orientation angle. It is similar to the filler clusters, increasing heat transfer by the combined effects of all fillers. These clusters are usually observed in composites with inadequate treatment. (2) Directional arrangement, all the fillers cross-sectional mains axes are randomly located parallel to the heat flux direction. The positions of filler cross-sections are randomly assigned, however the orientation angles are equaled to 0°. At present, many new processing technologies are used to improve performance of composites by controlling the orientation angle of fillers [31]. (3) Random arrangement, the position and orientation angle are randomly assigned in the cell. This is in agreement with practical composite materials. The fillers are mixed with the base material completely, so they are randomly distributed.

Figure 1 demonstrates the case that there is one filler in base materials. Its position and orientation angle can be specified by its coordinates (x_0, y_0) at the filler cross-sectional center and the orientation angle (β_0) between its cross-sectional main axis and the heat flux direction *y*.
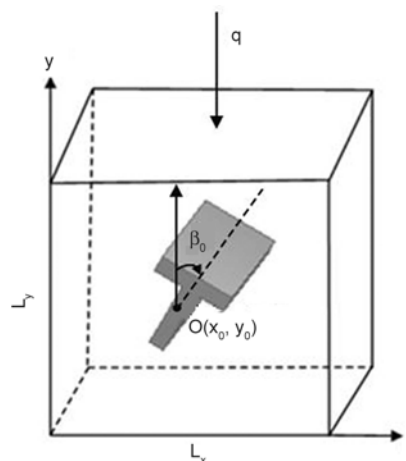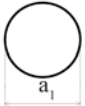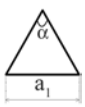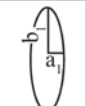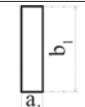

Figure 1. Schematic of a filler arranged in base materials

Table 1. The cross-sectional shapes of fillers and their parameters

Prismatic filler cross-sectional name	Cross-sectional shapes	Shape parameters
Circular		
Square		
Equilateral triangular		$\alpha = 60°$
Rhombic		$\beta = 60°$
Elliptical		$\dfrac{a_1}{b_1} = \dfrac{1}{3}$
Rectangular		$\dfrac{a_1}{b_1} = \dfrac{1}{4}$
T shaped		$a_1 = 5b_1 = \dfrac{5}{4}c_1 = 5d_1$
I shaped		$a_1 = 5b_1 = \dfrac{5}{3}c_1 = 5d_1$
Y shaped		$\dfrac{a_1}{b_1} = 5,\ \gamma = 120°$
Double Y shaped		$\dfrac{a_1}{b_1} = 5,\ \gamma = 120°$

A computer program is developed to automatically generate the positions and orientation angles of fillers [32–34]. At first, the positions for the filler cross-sectional centers are determined. Let coordinates (x_0, y_0) represent the positions of filler cross-sectional centers. Let L_x and L_y denote the length and height of the unit cell respectively, as shown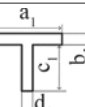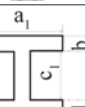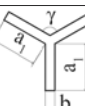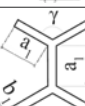 in Figure 1. Then a random number r_x ($0 < r_x < 1$) is generated by the computer. The coordinate x_0 is selected as the product of r_x and L_x. In a similar way coordinate y_0 is obtained. At last, the orientation angles of the filler cross-sections are assigned. If the filler

arrangement type is directional arrangement, the main axes of the filler cross-sections are set parallel to heat flux direction and the orientation angels are 0°. If it is random arrangement, the orientation angle β_0, defined as the angle between the filler cross-sectional main axis and the heat flux direction, is decided as the product of 2π and a random number from 0 to 1. In the process of the filler generation, if new filler is found to overlap with any other old fillers or boundaries, it is cancelled and new one is generated. The filler generation process ends when desired filler content is reached. The geometric models generated by the computer with directionally and randomly assigned fillers are shown in Figure 2b and 2c. The filler cross-sectional shape is I shaped and the filler content is 9%. As a comparison, the close-packed cell is artificial generation in Figure 2a. The nearest distance between the adjacent fillers is 0.05 mm. It is very similar to the cluster formation of the fillers.

In order to reflect the overall performance of the composites with different filler arrangements, a minimum number of fillers must be included in the model. If the number of fillers is too small, the results of different generations may be somewhat different. Consequently, the size of model must be chosen to be large enough to contain the minimum number of fillers, as long as computer capacity permits.

Figure 3 presents the effects of computational model sizes on the relative thermal conductivity of composite. As seen, when the model size becomes larger than 0.3 cm^2, the thermal conductivity is stable and the fluctuations from generation of cell is lower than 2%, regardless of the filler arrangement and content. The differences of thermal conductivity in *x*- and *y*- directions are within 2% for randomly arranged cell. The cell selected here is a 1×1 cm^2 square. It is large enough for this two-dimensional thermal conductivity calculation.

2.2. Heat conduction equations

For the two-dimensional cell generated in Figure 2, heat conduction in base materials is satisfied by Equation (1):

$$\frac{K_m}{(\rho c_p)_m}\left(\frac{\partial^2 T_m}{\partial x^2} + \frac{\partial^2 T_m}{\partial y^2}\right) = 0 \qquad (1)$$

where, T is temperature and x, y are coordinates, subscript '*m*' means base polymer materials. The physical properties, heat conductivity K, density ρ and
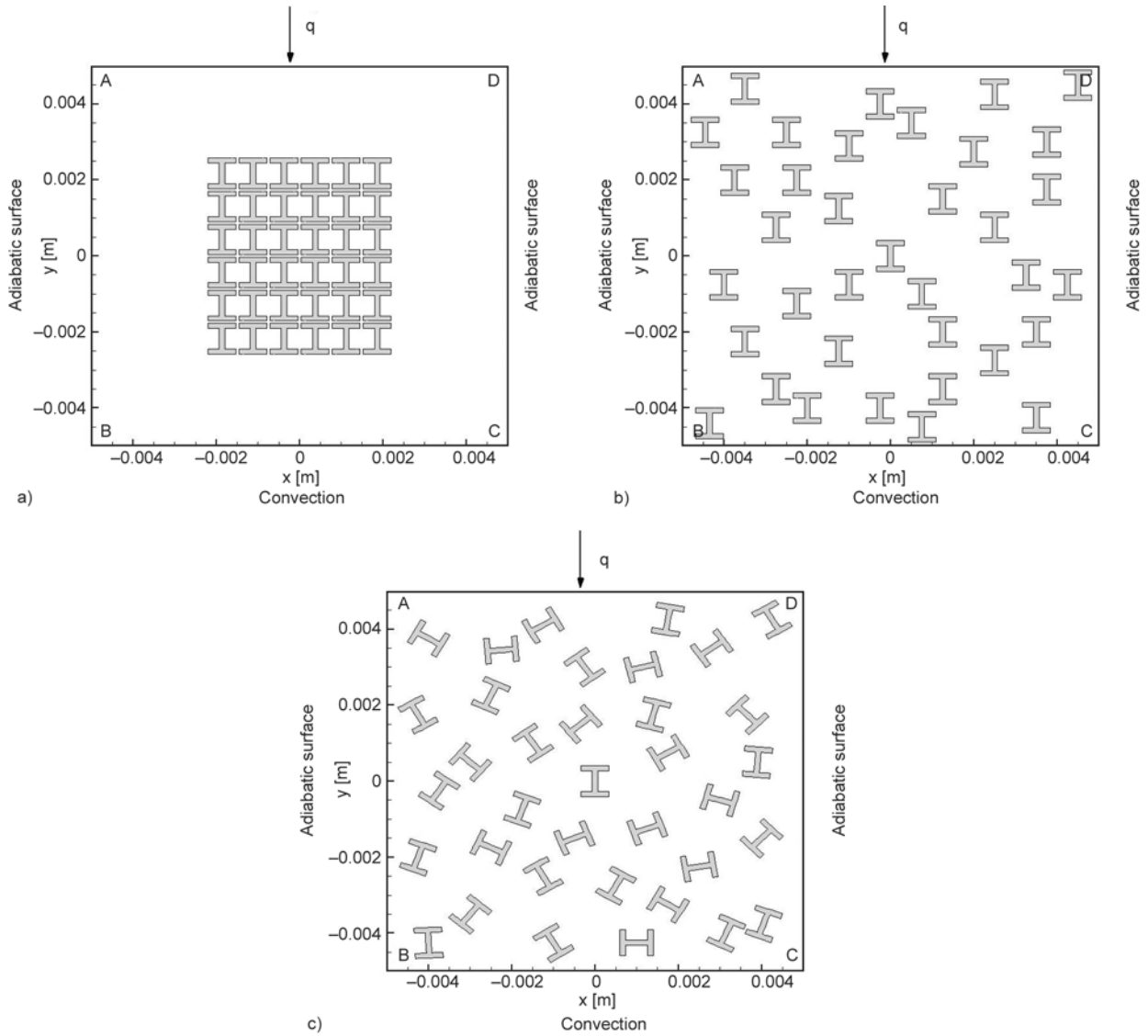
Figure 2. Two-dimensional cell model comprising of I shaped cross-sectional fillers and the base material, $V_f = 0.09$. (a) close-packed arrangement, (b) directional arrangement, (c) random arrangement.
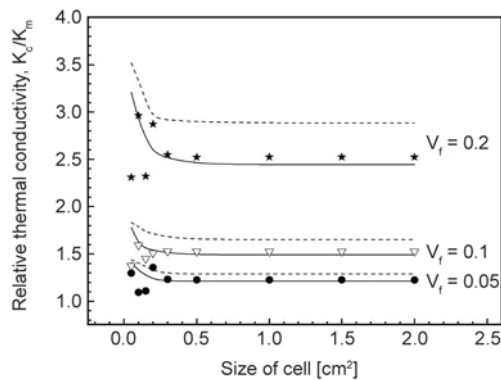
Figure 3. Effects of cell size on the relative thermal conductivity of composite, $K_m = 0.36$ W·m^{-1}·K^{-1}, $K_f = 50.2$ W·m^{-1}·K^{-1}. Solid lines represent the data in close-packed arrangement. Dash lines represent the data in directional arrangement. The discrete points are the value in random arrangement.

specific heat c_p here are written out, to reflect the local properties of the grids.

Heat conduction in the filler is described by Equation (2):

$$\frac{K_f}{(\rho c_p)_f}\left(\frac{\partial^2 T_f}{\partial x^2} + \frac{\partial^2 T_f}{\partial y^2}\right) = 0 \qquad (2)$$

The boundary condition at the top surface of the cell, AD is given by Equation (3):

$$-K_m \frac{\partial T}{\partial n}\Big|_r = q \qquad (3)$$

where, q is the heat flux, which is uniformly imposed on the upper surface, n is the normal direction of the surface. It is the second class boundary condition. In calculation, q is set to 1 kW/m^2.

A third class boundary condition is set on the bottom surface of the cell, BC as shown by Equation (4):

$$K_m \frac{\partial T}{\partial n}\Big|_r = h(T - T_f)_r \qquad (4)$$

where, the convective heat transfer coefficient (h) and ambient temperature (T_f) are set to constants. In this work, h is set to 20 W·m^{-2}·K^{-1}, and T_f is set to 300 K. The heat flows through the cell is prescribed and known as q, but the temperatures on other boundaries are unknown. They should be calculated by the heat conduction equations with the boundary conditions.

The other two boundary conditions, AB, DC is given by Equation (5):

$$\frac{\partial T}{\partial n}\Big|_r = 0 \qquad (5)$$

2.3. Heat conduction coupling

At the boundaries between the base materials and the fillers, the temperatures in the base materials are equaled to the fillers. They are expressed as Equation (6):

$$T_{m,\,interface} = T_{f,\,interface} \qquad (6)$$

where, subscript 'interface' means contact surfaces between the base materials and the fillers.

When the temperature fields in the cell are calculated, the thermal conductivity in y direction for the cell is estimated by Equation (7):

$$K_c = \frac{qL_y}{T_t - T_b} \qquad (7)$$

where, $T_t - T_b$ is the mean temperature difference between the upper and bottom surfaces of the cell. The surface mean temperature here is weighted by area L_x. Dimensions L_x (along the x axis) and L_y (along the y axis) are the cell length and height.

2.4. Calculation scheme and solution

Equations (1) to (7), which describe the conjugated heat conduction in the base materials and fillers, are solved by software-FLUENT [35–38]. The cell is discretized by finite volume method.

The discretized equations are solved by central difference scheme. The calculation methodology can be summarized as following:

(1) Assume initial temperature values for both the fillers and the base materials.

Table 2. Time consumed in calculation with different mesh numbers for a cell with 9% randomly arranged I shaped cross-sectional fillers

Mesh number	Meshing time [s]	Calculation time [s]	Relative thermal conductivity
100×100	34	36	1.438
200×200	80	82	1.458
400×400	600	420	1.476
800×800	5400	2100	1.478

(2) Using the temperature values for fillers at interface as the boundary values for the base materials to solve Equation (1), one gets the temperature field of the base materials..

(3) Taking the just calculated base material temperatures at interface as the boundary values to solve Equation (2), one gets the temperature fields in the fillers.

(4) Return to step (2) until all the old values and new values for both the base materials and the fillers are converged. In this way, the heat conduction equations are satisfied.

To assure the accuracy of the results, a check of grid independence is conducted. For a sample with randomly arranged I shaped cross-sectional fillers. The size of the cell is 0.01 m. The volumetric content of filler is 9%. The calculated relative thermal conductivity and the time consumed in meshing and calculating are presented in Table 2. The time required to perform the analysis is greatly increased as the mesh refinement increases. However no obvious change is observed for the results when the grid size is more than 400×400. Grid independence test is done and numerical uncertainty is within 0.2%. It indicates that grid size of 400×400 is adequate for this problem, because the difference between the results for grid size 800×800 and 400×400 is less than 0.15%. A validated commercial software-FLUENT is used to design the shape of fillers and calculate the data in the analysis. High order scheme, low relaxation factor and re-meshing are used to prevent undergoing oscillation. When the average heat flux on the y direction are known, the thermal conductivity is calculated by Equation (7).

3. Results and discussion
3.1. Effects of the prismatic filler arrangements

To theoretically study the effects of the prismatic filler arrangements having various cross-sectional

shapes on the thermal conductivity, temperature fields in the cell were calculated. The base materials studied here was paraffin wax, with thermal conductivity 0.36 W·m⁻¹·K⁻¹. The filler material was steel with thermal conductivity of 50.2 W·m⁻¹·K⁻¹. Using the selected materials, the thermal conductivity of composites was calculated by numerical analysis method using the model proposed in this study. The thermal conductivity of the investigated composite is measured by Hot Disk (DRX-2). It is based on the Transient Plane Source (TPS) technique, and can be widely used in the measurement of the thermal conductivity of materials.

Figure 4 shows the relative thermal conductivity of composite materials for various filler arrangements at different filler contents. There are three typical filler arrangements and six representative filler cross-sectional shapes. As seen, the thermal conductivity increases with filler content, regardless of the filler arrangements and cross-sectional shapes. In a directionally arranged cell, the fillers are arranged as that in Figure 2b. Their cross-sectional main axes are the same as the input heat flux direction, and the positions are randomly. In these cases, all the filler cross-sectional shapes have the largest contribution for thermal conductivity improvement. On the contrary,
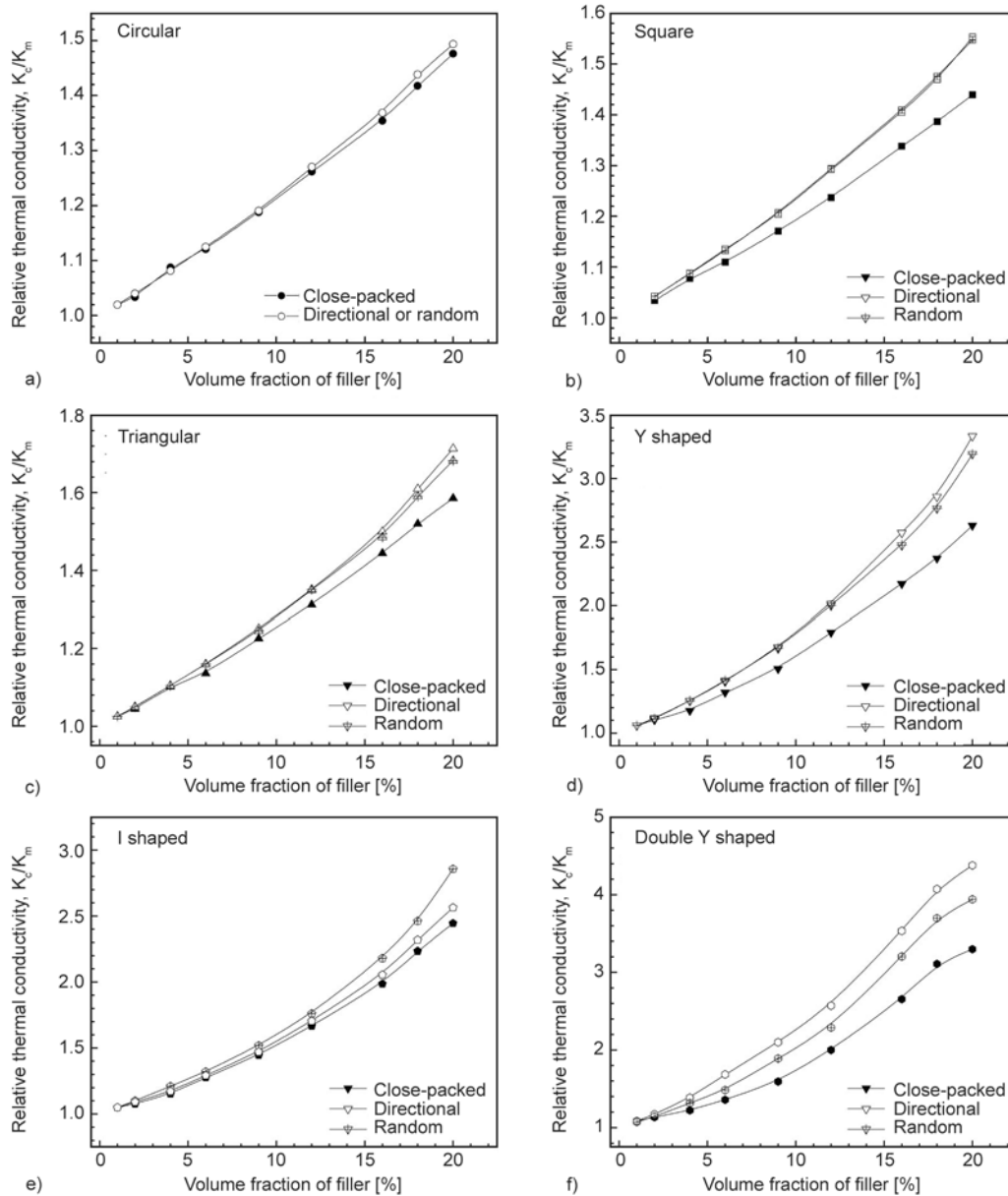

Figure 4. Relative thermal conductivity of composite materials with different filler arrangements and filler cross-sectional shapes: a) circular, b) square, c) triangular, d) Y shaped, e) I shaped, f) double Y shaped

when the fillers are close-packed arranged in polymers as showed in Figure 2a, the contribution of all filler cross-sectional shapes are the smallest. Compared to directional and close-packed arrangements, the random arrangement has middle contribution to the thermal conductivity improvement.

The effects of the filler arrangements are complex for different filler cross-sectional shapes. The circular is a perfectly symmetrical shape. It is not affected by the orientation angle, so the directional and random arrangements have the same structure model. As seen from Figure 4 circular cross-sectional filler, at lower filler content below 10%, the thermal conductivity of composites with randomly and closed-packed arranged fillers are basically identical. When the filler content larger than 10%, the results of the randomly arranged case are larger than that of close-packed case. The differences increase with filler content. However, at a large filler content of 20%, the maximize difference is less than 2%. Some cross-sectional shapes are similar to symmetrical structure, like square, triangular and Y shaped. They have similar heat conduction distance at different filler arrangements. Their thermal conductivities are insensitive to orientation angles. The thermal conductivities of composites with directionally and randomly arranged fillers have small difference as showed in Figure 4 for the square cross-sectional filler, triangular cross-sectional filler and Y shaped cross-sectional filler cases. Their values are small in close-packed arrangement. The control of orientation angles is not effective for these filler cross-sectional shapes. In order to avoid aggregate of fillers, the new technology should be investigated to mix well with base polymer. Other filler cross-sectional shapes like double Y shaped, I shaped, T shaped, elliptical, rhombic and rectangular, are more sensitive to filler arrangement. The heat conductivity distance decreases drastically with orientation angles. The differences of thermal conductivity between the directional and the random cell become more and more apparent with increasing filler content. At
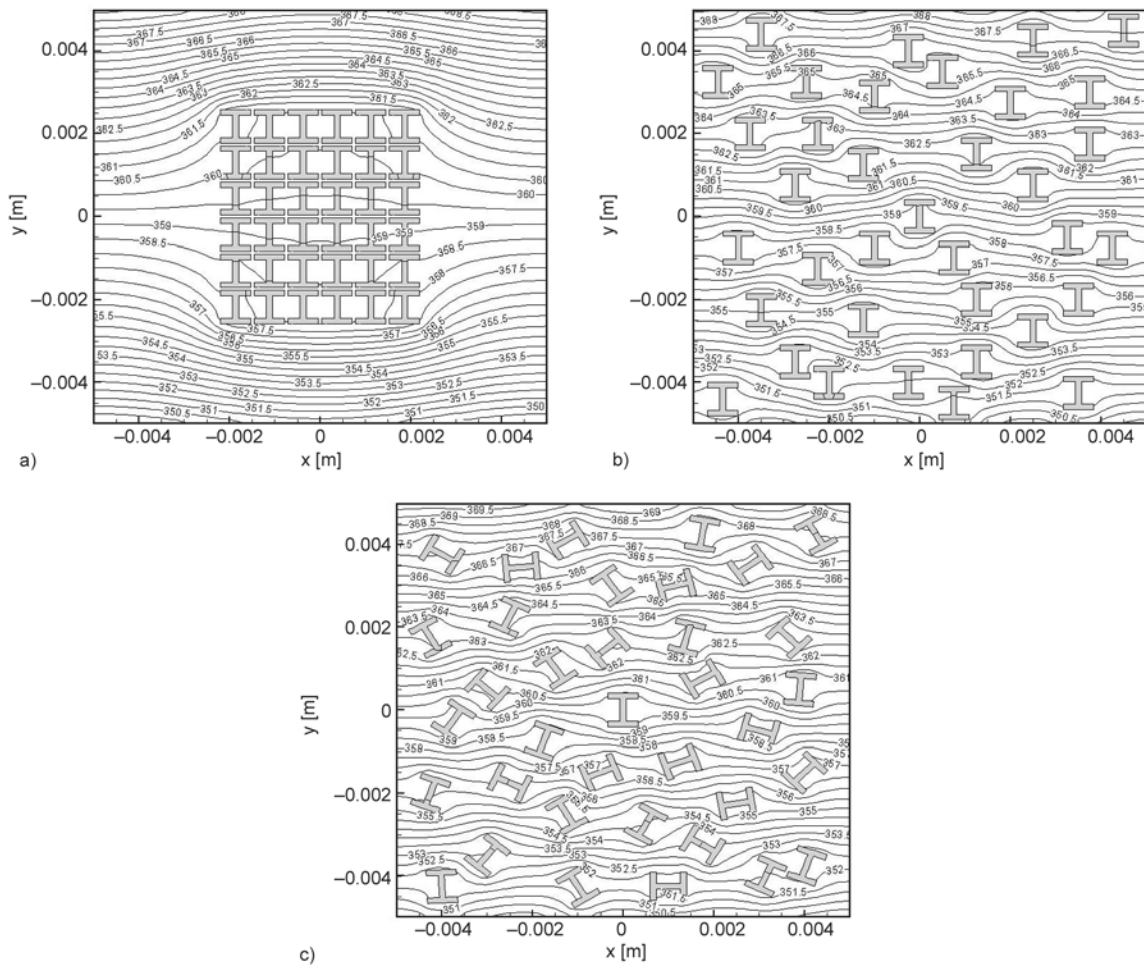

Figure 5. Contours of temperature [K] in the sample cell with 9% I shaped cross-sectional fillers. (a) close-packed arrangement, (b) directional arrangement, (c) random arrangement.

the same filler content of 20%, the differences of rectangular cross-sectional filler is 34%, I shaped cross-sectional filler is 12.5%. By contrast, the difference of the square cross-sectional filler is no more than 0.35%. This shows that to make composite with directional arrangement of fillers is very important for most filler cross-sectional shapes excepting circular.

The effect of fillers augmentation can be explained by the isotherms in the unit cell. Figures 5 and 6 show the effects of the filler arrangements on the isotherms for two filler cross-sectional shapes: I shaped and square. The temperature fields in the base materials are deformed and shortcut by fillers. The fillers act as numerous bridges, transporting the heat fluxes through them. For each bridge, it receives heat at the high temperature side, and releases the heat at the low temperature side. The middle part of the filler is capable of transporting this received heat effectively, with little temperature gradients. The base material near the filler seldom takes part in

heat transport in the direction along the isotherms in the fillers, rather, it is shortcut. In this way, the heat transport is increased in the cell.

As seen from Figure 5a and Figure 6a, when the fillers in close-packed arrangement, all the fillers arranged in the central of polymer with small distance. This case is very similar to that the fillers are wired together to function as a single system, like a 'larger filler'. The larger filler is beneficial for heat conductivity increasing. The effect in temperature field deformation is more obvious than single filler. However, the larger filler is only one and distributed in the central of the cell. The role of the fillers to enhance heat transfer is very weak in most other regions. Thus, the improvement of heat conductivity is very limited in the close-packed arrangement. By comparing Figures 5b, 5c and Figures 6b, 6c, it is found that when the filler arrangement changes from directional to random, the isotherms change slightly for square cross-sectional fillers. However, the change for I shaped cross-sectional filler is
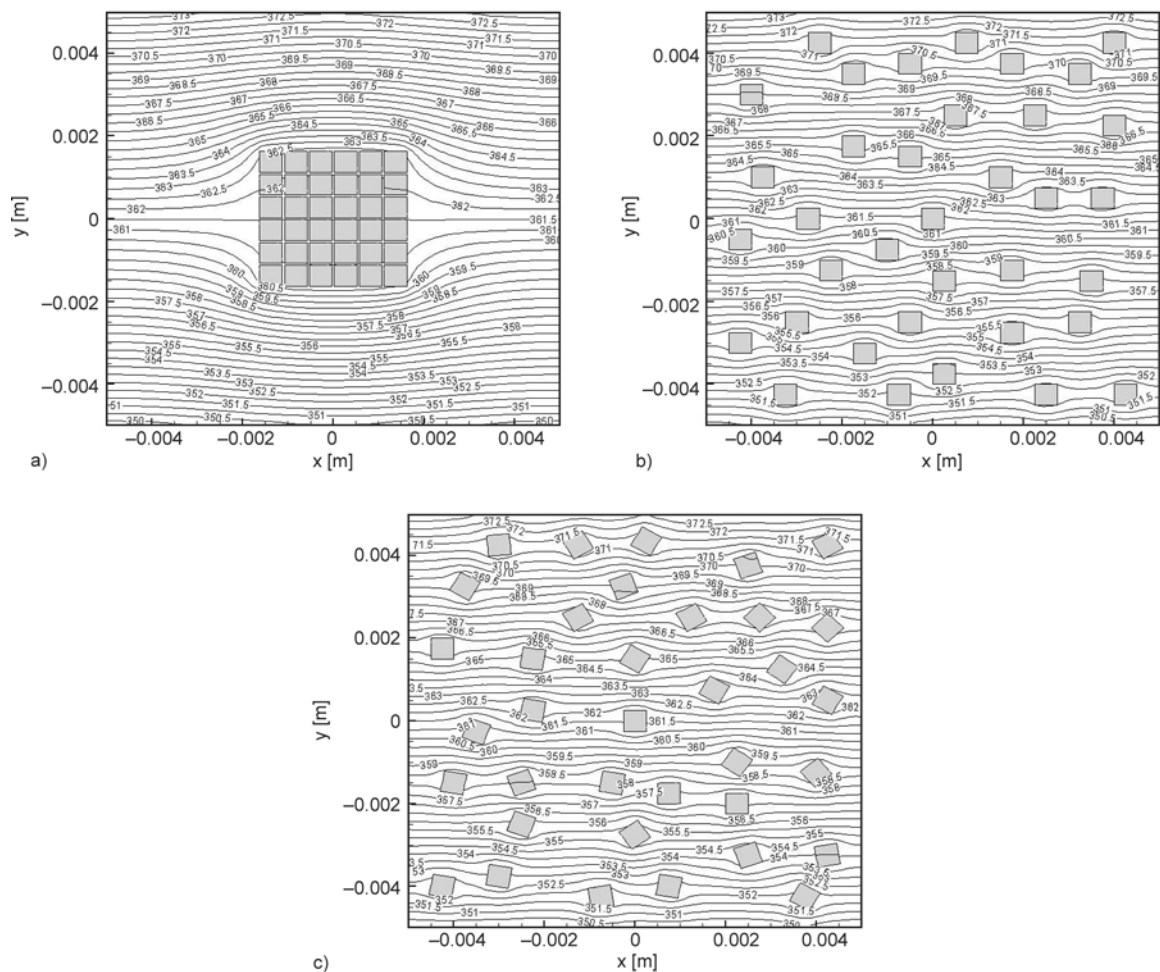

Figure 6. Contours of temperature [K] in the sample cell with 9% square cross-sectional fillers. (a) close-packed arrangement, (b) directional arrangement, (c) random arrangement.

large. The bridge for heat conduction is shortened when I shaped cross-sectional filler is deflected. The thermal conductivity of composites with directionally arranged I shaped cross-sectional filler is much larger than random arrangement. The directional arrangement of I shaped cross-sectional filler is necessary to maximize the role of fillers.

3.2. Effects of filler cross-sectional shapes

All the proposed filler cross-sectional shapes listed in Table 1 are modeled. The arrangements of fillers have three types, as already indicated. The thermal conductivity of these composites is then calculated and compared for various filler cross-sectional shapes, as shown in Figures 7–9. The thermal conductivity increases with filler content in three filler arrangements, regardless of the filler cross-sectional shapes. However, the steps of increase are different. The double Y shaped cross-sectional filler resulting in a larger increasing rate, followed by the Y shaped cross-sectional filler. The trends of other filler cross-sectional shapes are dependent in filler arrangements. The order of thermal conductivity increasing for close-packed arranged fillers is showed in Figure 7, double Y shaped > Y shaped > I shaped > T shaped > rectangular ≈ elliptical ≈ rhombic ≈ triangular ≈ square ≈ circular. Except double Y shaped, Y shaped, I shaped and T shaped,

the effects of filler cross-sectional shapes on thermal conductivity are not obvious in this filler arrangement. Generally, the fillers are easy to be attracted together due to their large specific surface area and high surface energy. The effects of most filler shapes will be seriously deteriorated in this situation. New technique of making composite, such as liquid phase method, should be designed to overcome this aggregation.

Figure 8 shows the thermal conductivity of composites with directionally arranged fillers. The order of thermal conductivity increasing is: double Y shaped > Y shaped > rectangular ≈ shaped > T shaped > elliptical > rhombic > triangular > square ≈ circular. All the cross-sectional shapes with directionally arranged fillers have larger effects on increasing thermal conductivity. In industrial application, the technology of making composite with directional filler arrangement should be paid special attention. The trends for randomly arranged fillers are showed in Figure 9. The order of thermal conductivity increasing is: double Y shaped > Y shaped > I shaped > T shaped > rectangular > elliptical > rhombic ≈ triangular > square ≈ circular. For the random arrangement, the constructible filler cross-sectional shapes [39] such as double Y shaped, Y shaped, I shaped and T shaped are better than other regular shapes in enhancing thermal conductivity. They have long heat

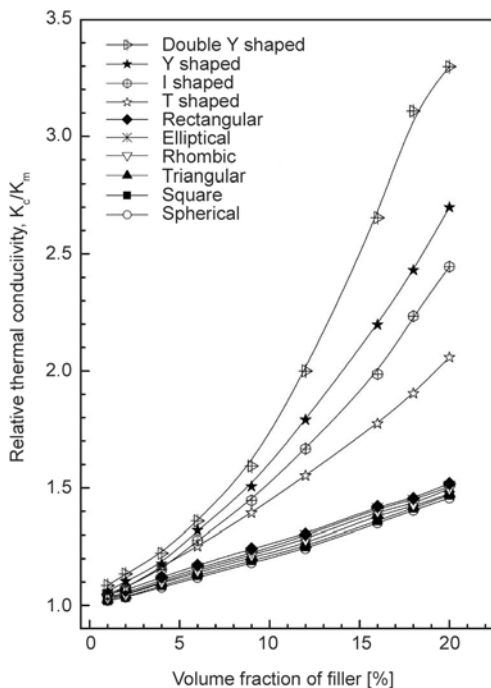**Figure 7.** Relative thermal conductivity of composites materials with different filler cross-sectional shapes: close-packed arrangement
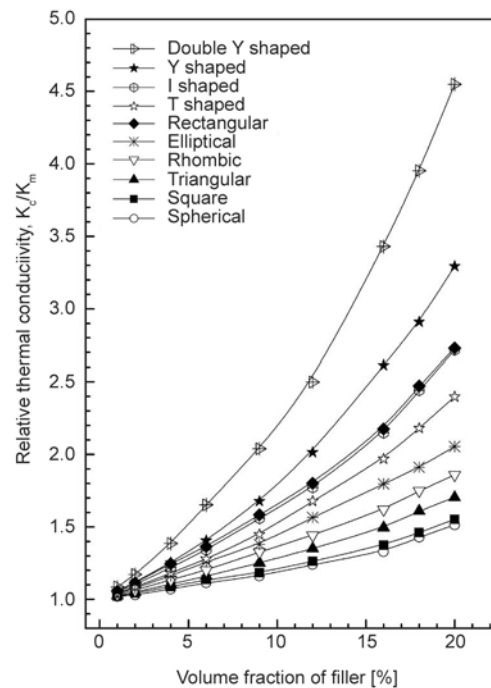

Figure 8. Relative thermal conductivity of composites materials with different filler cross-sectional shapes: directional arrangement
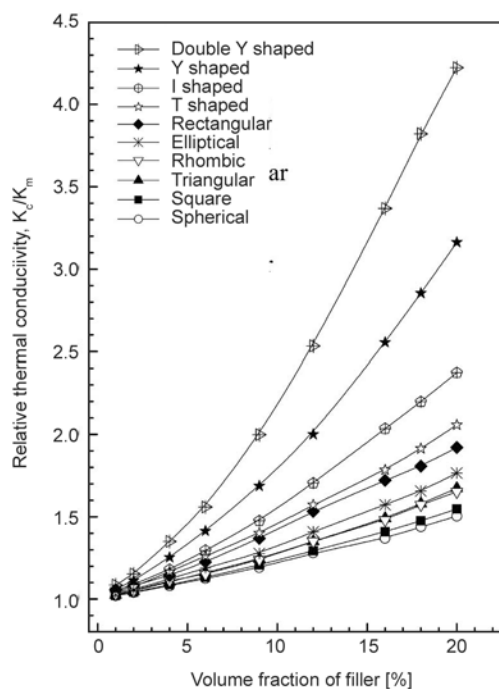
Figure 9. Relative thermal conductivity of composites materials with different filler cross-sectional shapes: random arrangement

conduction distances and large contact areas even when they are placed unfavorably. From above analysis, it can be concluded the best fillers are those that have long heat conduction distances, regardless of filler arrangement. The aggregation of fillers should be avoided for all the filler cross-sectional shapes.

Above-mentioned results show that the filler arrangement has very large effect on enhancement of thermal conductivity. In future study, the control of filler arrangement should be investigated for most filler shapes.

4. Conclusions

To add highly conductive fillers in the polymer matrix is an effective way to increase thermal conductivity of polymers. This study investigated the effects of three typical filler arrangements and ten filler cross-sectional shapes. Following results can be concluded:

(1) For increasing thermal conductivity, best filler arrangement is that all the fillers should have the longest heat conduction distances, and the largest sphere diameter of influence. From this respect, the directional arrangement for double Y shaped, I shaped, T shaped, elliptical, rhombic and rectangular cross-sectional fillers are the best. The efficiency of circular, square, triangular and Y shaped

cross-sectional fillers are similar in directional and random arrangement. Thermal conductivity is the smallest in close-packed arrangement for all the filler cross-sectional shapes.

(2) Best filler shape should be constructible shape. Best fillers should have relatively long heat conduction distances in any types of the filler arrangements. The double Y shaped, Y shaped, I shaped and T shaped are the best cross-sectional shapes in increasing heat conductivity.

(3) In industrial applications, new methods to control the arrangement of fillers should be investigated, and the double Y shaped, Y shaped, I shaped and T shaped cross-sectional fillers should be used to replace the traditional fillers like spherical and fibroid fillers.

Acknowledgements

Nomenclature

a_1 sectional length
AB   left boundary of cell
AD   top boundary of cell
b_1 sectional length
BC   bottom boundary of cell
c_p specific heat [kJ·kg^{-1}·K^{-1}]
c_1 sectional length
d_1 sectional length
DC   right boundary of cell
K thermal conductivity [W·m^{-1}·K^{-1}]
L_x length along the x axis
L_y height along the y axis
n normal direction
q heat flux [W·m^{-2}]
V volumetric fraction
x, y coordinates [m]
x_0 coordinate of filler cross-sectional center [m]
y_0 coordinate of filler cross-sectional center [m]

Greek letters

α apex angle for triangle [°]
β apex angle for rhombus [°]
β_0 orientation angle [°]
γ apex angle for Y and double Y [°]
ρ density [kg/m^3]

Subscripts

c composite
f filler
m polymer matrix

References

[1] Zaheed L., Jachuck R. J. J.: Review of polymer compact heat exchangers, with special emphasis on a polymer film unit. Applied Thermal Engineering, **24**, 2323–2358 (2004).
DOI: 10.1016/j.applthermaleng.2004.03.018

[2] Zhang L-Z., Wang X-J., Quan Y-Y., Pei L-X.: Conjugate heat conduction in filled composite materials considering interactions between the filler and base materials. International Journal of Heat and Mass Transfer, **64**, 735–742 (2013).
DOI: 10.1016/j.ijheatmasstransfer.2013.05.021

[3] Joen C. T., Park Y., Wang Q., Sommers A., Han X., Jacobi A.: A review on polymer heat exchangers for HVAC&R applications. International Journal of Refrigeration, **32**, 763–779 (2009).
DOI: 10.1016/j.ijrefrig.2008.11.008

[4] Wang Q., Han X. H., Sommmers A., Park Y., T'Joen C., Jacobi A.: A review on application of carbonaceous materials and carbon matrix composites for heat exchangers and heat sinks. International Journal of Refrigeration, **35**, 7–26 (2012).
DOI: 10.1016/j.ijrefrig.2011.09.001

[5] Liu X. H., Jiang Y.: Coupled heat and mass transfer characteristic in packed bed dehumidifier/regenerator using liquid desiccant. Energy Conversion and Management, **49**, 1357–1366 (2008).
DOI: 10.1016/j.enconman.2008.01.009

[6] Mahmud K., Mahmood G. I., Simonson C. J., Besant R. W.: Performance testing of a counter-cross-flow run-around membrane energy exchanger (RAMEE) system for HVAC applications. Energy and Buildings, **42**, 1139–1147 (2010).
DOI: 10.1016/j.enbuild.2010.02.005

[7] Vali A., Simonson C. J., Besant R. W.: Numerical model and effectiveness correlations for a run-around heat recovery system with combined counter and cross flow exchangers. International Journal of Heat and Mass Transfer, **52**, 5827–5840 (2009).
DOI: 10.1016/j.ijheatmasstransfer.2009.07.020

[8] Zhang L-Z., Wang X-J., Pei L-X.: Nonlinear programming optimization of filler shapes for composite materials with inverse problem technique to maximize heat conductivity. International Journal of Heat and Mass Transfer, **55**, 7287–7296 (2012).
DOI: 10.1016/j.ijheatmasstransfer.2012.07.059

[9] Han Z., Fina A.: Thermal conductivity of carbon nanotubes and their polymer nanocomposites: A review. Progress in Polymer Science, **36**, 914–944 (2011).
DOI: 10.1016/j.progpolymsci.2010.11.004

[10] Sofian N. M., Rusu M., Neagu R., Neagu E.: Metal powder-filled polyethylene composites. V. Thermal properties. Journal of Thermoplastic Composite Materials, **14**, 20–33 (2001).
DOI: 10.1106/9N6K-VKH1-MHYX-FBC4

[11] Yu A., Ramesh P., Sun X., Bekyarova E., Itkis M. E., Haddon R. C.: Enhanced thermal conductivity in a hybrid graphite nanoplatelet – Carbon nanotube filler for epoxy composites. Advanced Materials, **20**, 4740–4744 (2008).
DOI: 10.1002/adma.200800401

[12] Lewis T. B., Nielsen L. E.: Dynamic mechanical properties of particulate-filled composites. Journal of Applied Polymer Science, **14**, 1449–1471 (1970).
DOI: 10.1002/app.1970.070140604

[13] Nozad I., Garbonell R. G., Whitaker S.: Heat conduction in multiphase systems – I: Theory and experiment for two-phase systems. Chemical Engineering Science, **40**, 843–855 (1985).
DOI: 10.1016/0009-2509(85)85037-5

[14] Whitaker S.: The method of volume averaging (theory and applications of transport in porous media). Springer, Haifa (1998).

[15] Nielsen L.: The thermal and electrical conductivity of two-phase systems. Industrial and Engineering Chemistry Fundamentals, **13**, 17–20 (1974).
DOI: 10.1021/i160049a004

[16] Baschirow A. B., Manukian A. M.: Thermal conductivities of polymers at various temperatures and pressures. Polymer Mechanics, **3**, 564–566 (1974).
DOI: 10.1007/BF00865620

[17] Bruggeman D. A.: Dielectric constant and conductivity of mixtures of isotropic materials. Annals of Physics, **24**, 636–679 (1953).

[18] Agari Y., Uno T.: Estimation on thermal conductivities of filled polymers. Journal of Applied Polymer Science, **32**, 5705–5712 (1986).
DOI: 10.1002/app.1986.070320702

[19] Agari Y., Ueda A., Nagai S.: Thermal conductivity of a polyethylene filled with disoriented short-cut carbon fibers. Journal of Applied Polymer Science, **43**, 1117–1124 (1991).
DOI: 10.1002/app.1991.070430612

[20] Agari Y., Ueda A., Nagai S.: Thermal conductivities of composites in several types of dispersion systems. Journal of Applied Polymer Science, **42**, 1665–1669 (1994).
DOI: 10.1002/app.1991.070420621

[21] Tavman I. H., Akinci H.: Transverse thermal conductivity of fiber reinforced polymer composites. International Communications in Heat and Mass Transfer, **27**, 253–261 (2000).
DOI: 10.1016/S0735-1933(00)00106-8

[22] Halpin J. C.: Stiffness and expansion estimates for oriented short fiber composites. Journal of Composite Materials, **3**, 732–734 (1969).
DOI: 10.1177/002199836900300419

[23] Sanada K., Tada Y., Shindo Y.: Thermal conductivity of polymer composites with close-packed structure of nano and micro fillers. Composites Part A: Applied Science and Manufacturing, **40**, 724–730 (2009).
DOI: 10.1016/j.compositesa.2009.02.024

[24] Yang S-Y., Lin W-N., Huang Y-L., Tien H-W., Wang J-Y., Ma C-C. M., Li S-M., Wang Y-S.: Synergetic effects of grapheme platelets and carbon nanotubes on the mechanical and thermal properties of epoxy composites. Carbon, **49**, 793–803 (2011).
DOI: 10.1016/j.carbon.2010.10.014

[25] Fricke H.: A mathematical treatment of the electric conductivity and capacity of disperse systems I. The electric conductivity of a suspension of homogeneous spheroids. Physical Review Letters, **24**, 575–587 (1924).
DOI: 10.1103/PhysRev.24.575

[26] Nan C-W., Birringer R., Clarke D. R., Gleiter H.: Effective thermal conductivity of particulate composites with interfacial thermal resistance. Journal of Applied Physics, **81**, 6692–6699 (1997).
DOI: 10.1063/1.365209

[27] Duan H. L., Karihaloo B. L.: Effective thermal conductivities of heterogeneous media containing multiple imperfectly bonded inclusions. Physical Review B, **75**, 064206/1–064206/9 (2007).
DOI: 10.1103/PhysRevB.75.064206

[28] Wang X-J., Zhang L-Z., Pei L-X.: Thermal conductivity augmentation of composite polymer materials with artificially controlled filler shapes. Journal of Applied Polymer Science, **131**, 39550/1–39550/10 (2014).
DOI: 10.1002/app.39550

[29] Yang B., Han Z. H.: Temperature-dependent thermal conductivity of nanorod-based nanofluids. Applied Physical Letters, **89**, 083111/1–083111/3 (2006).
DOI: 10.1063/1.2338424

[30] Casado U., Marcovich N. E., Aranguren M. I., Mosiewicki M. A.: High-strength composites based on tung oil polyurethane and wood flour: Effect of the filler concentration on the mechanical properties. Polymer and Engineering and Science, **49**, 713–721 (2009).
DOI: 10.1002/pen.21315

[31] Han Y., Lv S., Hao C., Ding F., Zhang Y.: Thermal conductivity enhancement of BN/silicone composites cured under electric field: Stacking of shape, thermal conductivity, and particle packing structure anisotropies. Thermochimica Acta, **259**, 68–73 (2012).
DOI: 10.1016/j.tca.2011.11.029

[32] Xu Y., Yagi K.: Automatic FEM model generation for evaluating thermal conductivity of composite with random materials arrangement. Computational Materials Science, **30**, 242–250 (2004).
DOI: 10.1016/j.commatsci.2004.03.011

[33] Huang S-M., Zhang L-Z., Tang K., Pei L-X.: Fluid flow and heat mass transfer in membrane parallel-plates channels used for liquid desiccant air dehumidification. International Journal of Heat and Mass Transfer, **55**, 2571–2580 (2012).
DOI: 10.1016/j.ijheatmasstransfer.2012.01.003

[34] Phelan P. E., Niemann R. C.: Effective thermal conductivity of a thin, randomly oriented composite material. Journal of Heat Transfer, **120**, 971–976 (1998).
DOI: 10.1115/1.2825917

[35] Liu X. H., Jiang Y., Qu K. Y.: Heat and mass transfer model of cross flow liquid desiccant air dehumidifier/regenerator. Energy Conversion and Management, **48**, 546–554 (2007).
DOI: 10.1016/j.enconman.2006.06.002

[36] Zhang L-Z., Huang S-M.: Coupled heat and mass transfer in a counter flow hollow fiber membrane module for air humidification. International Journal of Heat and Mass Transfer, **54**, 1055–1063 (2011).
DOI: 10.1016/j.ijheatmasstransfer.2010.11.025

[37] Zhang L-Z., Huang S-M., Zhang W-B.: Turbulent heat and mass transfer across a hollow fiber membrane bundle considering interactions between neighboring fibers. International Journal of Heat and Mass Transfer, **64**, 162–172 (2013).
DOI: 10.1016/j.ijheatmasstransfer.2013.04.035

[38] Huang S. M., Yang M. L.: Longitudinal fluid flow and heat transfer between an elliptical hollow fiber membrane tube bank used for air humidification. Applied Energy, **112**, 75–82 (2013).
DOI: 10.1016/j.apenergy.2013.05.080

[39] Devpura A., Phelan P. E., Prasher R. S.: Size effects on the thermal conductivity of polymers laden with highly conductive filler particles. Microscale Thermophysical Engineering, **5**, 177–189 (2001).
DOI: 10.1080/108939501753222869

Effect of ionic liquids on the dispersion of zinc oxide and silica nanoparticles, vulcanisation behaviour and properties of NBR composites

M. Maciejewska[*]*, M. Zaborski*

Institute of Polymer and Dye Technology, Technical University of Lodz, Stefanowskiego 12/16, 90-924 Lodz, Poland

Abstract. The aim of this work was to study the activity of several alkylpyrrolidinium, alkylpyridinium, alkylpiperidinium and benzylimidazolium ionic liquids (ILs) for the purpose of improving the dispersion degree of vulcanisation activator and filler nanoparticles in the acrylonitrile-butadiene elastomer (NBR). The effect of the ionic liquids on the vulcanisation kinetics of the rubber compounds, crosslink density and mechanical properties of the vulcanisates and their resistance to thermo-oxidative and UV ageing was studied.
The use of ionic liquids allowed for a homogeneous dispersion of nanoparticles in the elastomer without detrimental effects on the vulcanisation process. The physical properties and the thermal stability of the obtained vulcanisates were significantly improved. Ionic liquids increased the crosslink density of the vulcanisates and their damping properties.
Pirydinium and piperidinium hexafluorophosphates were most effective at increasing the crosslink density and improving the properties of NBR composites.

Keywords: rubber, ionic liquids, nanosized zinc oxide, silica nanoparticles, vulcanisation behaviour

1. Introduction

Zinc oxide is the optimal activator of sulphur vulcanisation. During vulcanisation, zinc ions react with the accelerator to form highly active zinc complexes. The crosslinking reaction is preceded by a reaction of zinc oxide with stearic acid to form hydrocarbon-soluble zinc stearate. The crosslink density increases with the concentration of zinc stearate [1]. Zinc oxide is dispersed in the elastomer in the form of crystalline particles. Particles of the accelerator, sulphur and fatty acids diffuse inside the elastomer and are adsorbed on the surface of zinc oxide to form complexes. Nieuwenhuizen [2] proposed a mechanism wherein the surface of zinc oxide participates in the reaction and is the medium of the reaction. Therefore, the dispersion of inorganic zinc oxide in an organic elastomer is the fundamental parameter affecting the curing process. Because zinc oxide and vulcanisation accelerators are insoluble in rubber, it is assumed that crosslinking reactions occur in a two-phase system and are catalysed by conventional phase transfer catalysts, such as crown ethers or cryptands. ILs are assumed to catalyse the interfacial reactions and could function identically in the crosslinking process [3].

Despite the important role of zinc oxide in the sulphur vulcanisation of elastomers, the amount of zinc oxide in rubber compounds must be reduced to below 2.5% because of its toxicity to aquatic species [4]. Using nanosized zinc oxide as the activator is one method to reduce the amount of ZnO in the elastomer. Because of the reduction in particle size, this powder has a higher and more developed specific surface area. Better contact between the zinc oxide

*Corresponding author, e-mail: magdalena.maciejewska@p.lodz.pl

nanoparticles and the other components of the cross-linking system is achieved, which increases the activity of ZnO in vulcanisation and reduces the amount used in rubber compounds [5]. The key factor is to ensure the homogeneous dispersion of the nanoparticles in the elastomer matrix. Unfortunately, zinc oxide nanoparticles reveal a high tendency to agglomerate in rubber [6] because of the high surface energy of this powder [7]. Our previous studies showed that surfactants and ionic liquids, such as alkylimidazolium salts, effectively improved the dispersion of zinc oxide nanoparticles in the elastomer [6].

Fukushima and Aida [8] reported that imidazolium ionic liquids can be used to disperse single-walled carbon nanotubes in soft composite materials. The ability of ionic liquids to functionalise and improve the dispersion of carbon nanotubes has been intensively studied [9, 10] also in diene elastomers [11]. Ionic liquids resulted in the development of a conductive polychloroprene rubber containing a low concentration of multi-walled carbon nanotubes (MWCNTs) [12, 13]. The fine homogeneous dispersion of the MWCNTs and their strong secondary network in the elastomer resulted in the high conductivity of the composite. Kreyenschulte *et al.* [14] demonstrated attractive interactions between carbon black and ionic liquids such as 1-allyl-3-methylimidazolium chloride. It is hypothesised that these interactions are because of cation-π-interactions between IL cations and the π-electrons on the carbon black surface. ILs can act as local plasticisers at the carbon black surface and can accelerate the formation of a carbon black secondary network in unsaturated elastomers.

N-ethylmethylimidazolium bis(trifluoromethanesulfonyl)imide (EMITFSI) was used for the preparation of flexible solid polymer electrolytes based on acrylonitrile-butadiene elastomers and poly(ethylene oxide) interpenetrating polymer networks [15]. When swollen in EMITFSI, the NBR/PEO composites exhibited good mechanical properties and elongation at break and ionic conductivity higher than 10^{-4} S·cm^{-1} at room temperature. Similar results were obtained for interpenetrating polymer networks containing alkylpirrolidinium bis(trifluoromethanesulfonyl)imides [16]. Conductive NBR composites with an ionic conductivity of $2.54 \cdot 10^{-4}$ S·cm^{-1} have also been prepared using 1-butyl-3-methylimidazolium bis(trifluoromethyl sulfonyl)imide [17].

Ionic liquids were also used to improve the dispersion of silica in styrene-butadiene (SBR) composites. 1-Methylimidazolidine methacrylate salt (MimMa) was found to polymerise via a radical-initiated mechanism and was easily grafted onto SBR chains during vulcanisation [18]. Substantial hydrogen bonding between polymerised MimMa and silica facilitated the dispersion of silica in the elastomer and improved the interfacial interactions between SBR and silica particles. Silica agglomerates were significantly decreased, and the filler particles were uniformly distributed in the elastomer matrix. The mechanical properties of the SBR composites were improved. Similar results were reported for 1-methylimidazolium sorbate (MimS) [19]. These findings suggest that ionic liquids have the potential to improve the dispersion of solid nanoparticles in elastomers.

Our previous studies demonstrated that applying alkylimidazolium salts (bromides, chlorides, tetrafluoroborates and hexafluorophosphates) improved the dispersion of zinc oxide nanoparticles in the NBR and allowed for the production of vulcanisates with the amount of zinc oxide, sulphur and MBT reduced to 1.3 phr. These vulcanisates exhibited tensile strengths comparable to those without a dispersing agent [6]. In this work, we applied several alkylpyrrolidinium, alkylpyridinium, alkylpiperidinium and benzylimidazolium ionic liquids to improve the dispersion degree of zinc oxide and silica nanoparticles in NBR. The influence of nanosized zinc oxide and ILs on the curing kinetics of rubber compounds, vulcanisate crosslink density, tensile strength, damping properties, thermal stability and resistance to thermo-oxidative and UV ageing is discussed.

2. Materials and methods
2.1. Materials
The acrylonitrile-butadiene elastomer (EUROPREN N3960) containing 39 wt% acrylonitrile was obtained from Polimeri Europa (Rome, Italy). The Mooney viscosity was (ML1+4 (100°C):60). The elastomer was vulcanised with sulphur (Siarkopol, Poland), with microsized zinc oxide as the activator (ZnO, Aldrich, USA). To reduce the amount of zinc ions in the rubber compounds, nanosized zinc oxide (nZnO, Nanostructured & Amorphous Materials, Inc., USA) was used as an alternative to microsized ZnO. 2-Mercaptobenzothiazole (MBT, Aldrich, USA) was used as an accelerator. Silica, with a specific surface area

Table 1. Ionic liquids (ILs)

ILs	Symbol
1-Ethyl-1-methylpyrrolidinium bromide	EMPYRRBr
1-Ethyl-1-methylpyrrolidinium hexafluorophosphate	EMPYRRPF$_6$
1-Butyl-1-methylpyrrolidinium chloride	BMPYRRCl
1-Butyl-1-methylpyrrolidinium bromide	BMPYRRBr
1-Butyl-1-methylpyrrolidinium hexafluorophosphate	BMPYRRPF$_6$
1-Butyl-1-methylpyrrolidinium tetrafluoroborate	BMPYRRBF$_4$
1-Benzyl-3-methylimidazolium chloride	BenMICl
1-Benzyl-3-methylimidazolium hexafluorophosphate	BenMIPF$_6$
1-Benzyl-3-methylimidazolium tetrafluoroborate	BenMIBF$_4$
1-Butyl-4-methylpyridinium chloride	BMPYRCl
1-Butyl-4-methylpyridinium hexafluorophosphate	BMPYRPF$_6$
1-Butyl-4-methylpyridinium tetrafluoroborate	BMPYRBF$_4$
1-Butyl-1-methylpiperidinium hexafluorophosphate	BMPIPPF$_6$
1-Butyl-1-methylpiperidinium tetrafluoroborate	BMPIPBF$_4$

of 380 m^2/g (Aerosil 380, Evonic Industries, Germany), was used as the filler. Ionic liquids (Table 1) were obtained from Aldrich.

2.3. Preparation and characterisation of rubber compounds

Rubber compounds, with the formulations given in Table 2, were prepared using a laboratory two-roll mill. The samples were cured at 160°C until they developed a 90% increase in torque, which was measured by an oscillating disc rheometer (Monsanto). The kinetics of vulcanisation of the rubber compounds were studied using a DSC1 (Mettler Toledo) analyser by decreasing the temperature from 25 to –60°C at a rate of 10°C/min and then heating to 250°C at the identical heating rate. The crosslink density (v_T) of the vulcanisates was determined by their equilibrium swelling in toluene based on the Flory-Rehner equation [20]. The Huggins parameter of the elastomer-solvent interaction (χ) was calculated from the Equation (1):

$$\chi = 0.3809 + 0.6707 V_r \tag{1}$$

where V_r is the volume fraction of the elastomer in the swollen gel.

Table 2. Composition of the NBR-based rubber compounds [phr]

Ingredient	With micro-ZnO	With nano-ZnO
NBR	100	100
MBT	2	2
Sulphur	2	2
ZnO	5	2
Silica	30	30
Ionic liquid	–	2

The tensile properties of the vulcanisates were measured according to the standard procedures in ISO-37 using a ZWICK 1435 universal testing machine. Dynamic mechanical measurements were performed in tension mode using a DMA/SDTA861e analyser (Mettler Toledo). Measurements of the dynamic moduli were performed over the temperature range of –80 to 100°C with a heating rate of 2°C/min, a frequency of 1 Hz and a strain amplitude of 4 μm. The elastomer glass transition temperature was determined from the maximum of $\tan\delta = f(T)$, in which $\tan\delta$ is the loss factor, and T is the measurement temperature.

The thermal stability of the vulcanisates was studied using a TGA/DSC1 (Mettler Toledo) analyser. Samples were heated from 25 to 700°C in an argon atmosphere (60 mL/min) with a heating rate of 10°C/min.

The thermo-oxidative degradation of the vulcanisates was performed at a temperature of 100°C for 240 h. The UV degradation of the vulcanisates was performed for 120 h using a UV 2000 (Atlas) machine in two alternating segments: a day segment (irradiation 0.7 W/m^2, temperature 60°C, time 8 h) and a night segment (without UV radiation, temperature 50°C, time 4 h).

To estimate the resistance of the samples to ageing, their mechanical properties and crosslinking densities after ageing were determined and compared with the values obtained for the vulcanisates before the ageing process. The ageing factor (S) was calculated as the numerical change in the mechanical properties of the samples upon ageing (Equation (2)) [21]:

$$S = \frac{(TS \cdot EB)_{\text{after ageing}}}{(TS \cdot EB)_{\text{before ageing}}} \qquad (2)$$

3. Results and discussion

3.1. Dispersion of activator and filler nanoparticles in the elastomer

The ILs were used to improve the dispersion of the vulcanisation activator (zinc oxide) and filler nanoparticles in the elastomer matrix. The homogeneous dispersion of activator particles is required to maximise the activity of the curing system in the crosslinking process. Agglomeration decreases the specific surface area of the activator and the interphase between its particles and the other components of the curing system (sulphur and accelerator). During the first step of the vulcanisation process, particles of the accelerator, sulphur and fatty acids diffuse through the elastomer matrix and are adsorbed onto the ZnO surface, forming intermediate reactive complexes [1]. Therefore, the contact between the ZnO particles and the accelerator in the elastomer matrix should be maximised to enhance the efficiency of the zinc oxide during vulcanisation. The dispersion of the filler particles controls the reinforcement effect of the filler and determines the mechanical properties of the vulcanisate. Agglomerates concentrate stresses in the material when subjected to external strain that can lead to early destruction. SEM images of the vulcanisate surfaces were obtained to examine the dispersion of the activator and filler nanoparticles in the elastomer. These results are presented in Figure 1a–1j.

Zinc oxide and silica nanoparticles showed a strong tendency to agglomerate in the elastomer. They formed agglomerates several micrometres in size consisting of nanosized primary particles (Figure 1a). The dispersion of the zinc oxide and filler particles in the presence of ILs is presented in Figures 1b–1j. Hexafluorophosphates and tetrafluoroborates significantly improved the dispersion of the nanoparticles in the elastomer. The particles were homogeneously dispersed and tightly bound to the elastomer matrix. Therefore, these salts seem to be active dispersing agents that can improve the dispersion degree of zinc oxide and silica in the NBR elastomer. Chlorides were less effective in preventing the particles from agglomeration. Nanoparticles created small agglomerates approximately 1-2 µm in size. However, these agglomerates were uni-

formly dispersed in the elastomer and were surrounded with elastomer film. They did not affect the tensile properties of the vulcanisates. The lower efficiency of the chlorides can be related to their poor miscibility with the elastomer during the preparation of the rubber compounds. The addition of these ILs resulted in the crumbling of the elastomer during processing with the use of the two-roll mill.

3.2. Curing characteristics and the crosslink density of the vulcanisates

The influence of ILs on the vulcanisation process was estimated based on rheometer measurements. The curing characteristics of the NBR compounds and the crosslink densities of the vulcanisates are given in Table 3.

For curing, the conventional NBR compound system consisting of an accelerator (MBT), sulphur and microsized zinc oxide was used and compared with the system containing nanosized zinc oxide and IL. The use of nanosized zinc oxide increased the torque increment compared with that of the reference rubber compound containing microsized ZnO. No considerable influence on the vulcanisation time or scorch time was observed. The use of the ILs significantly reduced the vulcanisation time and increased the torque increment of the rubber compounds compared to the reference compounds with micro- or nanosized zinc oxide. The crosslink density of the

Table 3. Curing characteristics and crosslink densities of NBR vulcanisates containing ILs

ILs	ΔG [dNm]	t_{90} [min]	t_p [min]	$v_T \cdot 10^4$ [mol/cm³]
ZnO	44.5	50	2.2	19.8
nZnO	67.8	50	2.9	20.4
EMPYRRBr	123.2	40	2.1	22.5
EMPYRRPF$_6$	106.5	45	3.1	21.9
BMPYRRCl	120.5	25	2.8	23.1
BMPYRRBr	109.2	25	2.9	21.3
BMPYRRPF$_6$	101.5	40	3.6	21.2
BMPYRRBF$_4$	97.4	30	3.6	20.1
BenMICl	109.0	30	3.1	21.4
BenMIPF$_6$	102.3	37	3.0	20.8
BenMIBF$_4$	104.0	35	2.7	20.3
BMPYRCl	104.3	22	2.5	23.6
BMPYRPF$_6$	104.7	40	3.5	21.7
BMPYRBF$_4$	109.9	40	3.5	20.4
BMPIPPF6	111.0	45	3.5	21.5
BMPIPBF4	114.4	45	2.5	21.1

ΔG – increment of torque in the rubber compound during vulcanisation; t_{90} – optimal vulcanisation time; t_p – scorch time, v_T – crosslink density of vulcanisates
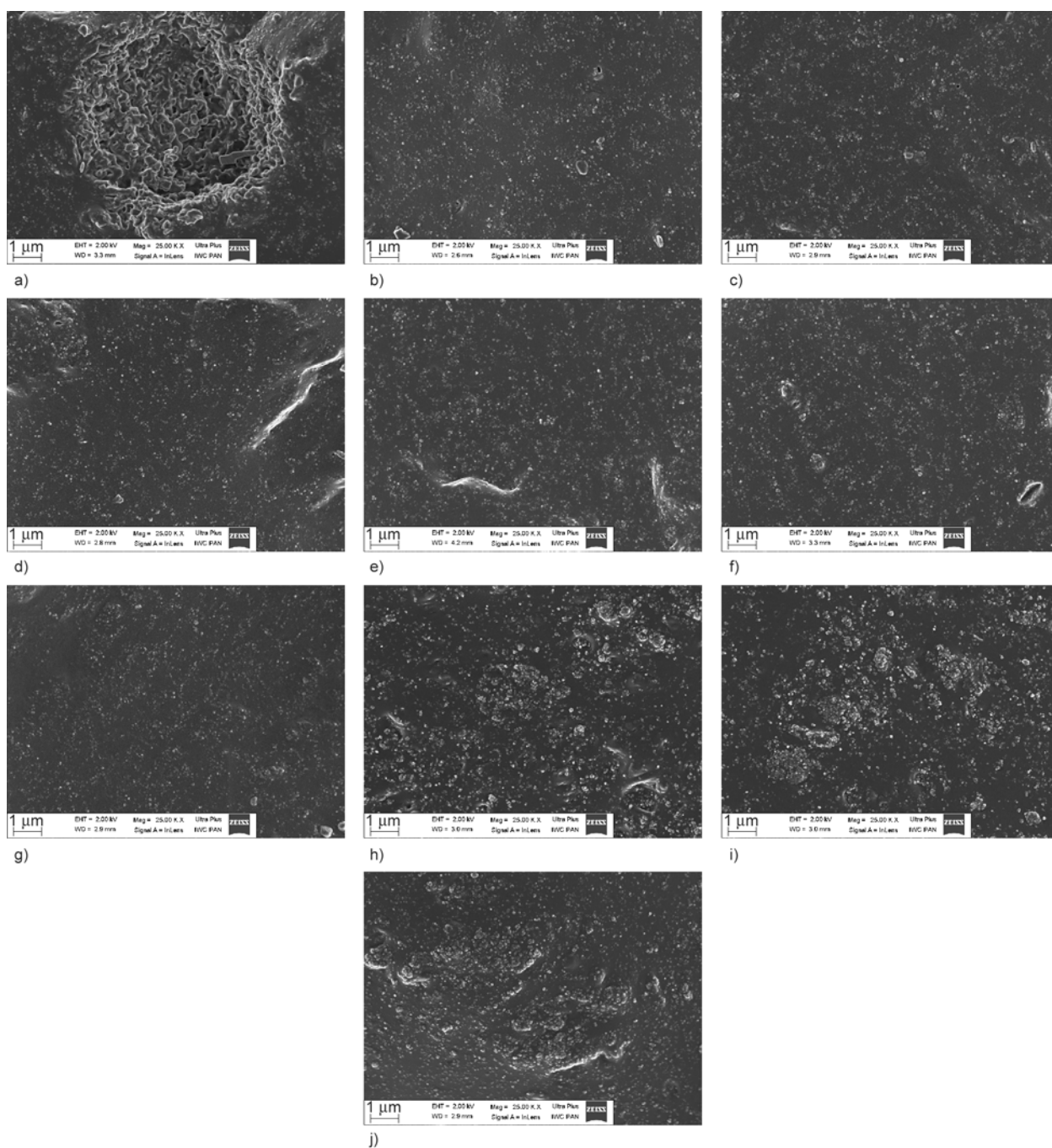
Figure 1. SEM images of vulcanisates: a) without IL, b) with EMPYRRPF$_6$, c) with BMPYRRPF$_6$, d) with BenMIBF$_4$, e) with BMPYRPF$_6$, f) with BMPYRBF$_4$, g) BMPIPPF$_6$, h) with BMPYRRCl, i) with BenMICl, j) with BMPYRCl

vulcanisates also increased. This increase could be because of the more homogeneous dispersion of the zinc oxide nanoparticles in the elastomer that led to better contact between particles of the vulcanisation activator and the other components of the curing system (sulphur, accelerator). ILs may have acted as a catalyst for the interfacial crosslinking reactions. Zinc oxide and vulcanisation accelerators are insoluble in the rubber. Therefore, the crosslinking reac-

tions occur in a two-phase system. ILs are presumed to catalyse the interfacial reactions [3]. This assumption is confirmed by the fact that the composites containing chlorides were characterised by the shortest vulcanisation time and higher crosslink density compared to other ILs, despite poor dispersion of zinc oxide nanoparticles (Figures 1b–1j). There was no simple correlation between the structure of the IL and its influence on the curing charac-

Table 4. Temperature and energetic effects of NBR vulcanisation measured by DSC

ILs	Vulcanisation temperature range [°C]	Energetic effect of vulcanisation [J/g]
ZnO	163–240	10.1
nZnO	165–240	10.3
EMPYRRPF$_6$	168–244	17.6
BMPYRRCl	143–230	9.5
BMPYRRBr	140–230	8.3
BMPYRRPF$_6$	168–240	12.6
BMPYRRBF$_4$	145–230	9.5
BenMIPF$_6$	168–237	13.2
BMPYRPF$_6$	168–230	10.6
BMPIPPF$_6$	168–236	10.9

Table 5. Mechanical properties of NBR vulcanisates containing ILs

ILs	TS [MPa]	EB [%]
ZnO	20.4	531
nZnO	22.4	526
EMPYRRBr	26.6	435
EMPYRRPF$_6$	26.3	490
BMPYRRCl	23.8	429
BMPYRRBr	23.7	411
BMPYRRPF$_6$	27.0	502
BMPYRRBF$_4$	25.0	520
BenMICl	23.4	425
BenMIPF$_6$	25.8	501
BenMIBF$_4$	27.3	530
BMPYRCl	24.7	402
BMPYRPF$_6$	26.8	465
BMPYRBF$_4$	27.0	520
BMPIPPF$_6$	26.4	430
BMPIPBF$_4$	23.7	474

TS – tensile strength; *EB* – elongation at break.

teristics. However, vulcanisates containing pyrrolidinium salts exhibited one of the highest crosslink densities.

We then examined the influence of nanosized zinc oxide and ILs on the temperature and energetic effects of vulcanisation using DSC analysis. The results for exemplary rubber compounds are given in Table 4.

Nanosized zinc oxide had no significant influence on the temperature and heat of vulcanisation compared with those of the NBR compounds containing the microsized activator. The vulcanisation is an exothermic process that took place in a temperature range of 163–240°C, with an energetic effect of 10 J/g. The hexafluorophosphates did not affect the vulcanisation temperature, but the increase in the energetic effect of the process was observed in most of the rubber compounds. Chlorides, bromides and tetrafluoroborates, regardless of the cation type, decreased the vulcanisation onset temperature by 20°C compared with rubber compounds with micro- or nanosized zinc oxide. The application of these ILs allows the NBR elastomer to be cured at lower temperatures than the commonly used 160°C.

3.3. Mechanical properties of the vulcanisates

The aim of applying the ILs was to achieve the homogeneous dispersion of the zinc oxide and silica nanoparticles in the elastomer and to improve the tensile strength of the vulcanisates. The mechanical properties of the NBR vulcanisates were studied under static and dynamic conditions. The results of the tensile tests are presented in Table 5.

NBR conventionally crosslinked with sulphur exhibited a tensile strength of 20.4 MPa and an elongation at break of approximately 531%. Nanosized zinc

oxide increased the tensile strength by 2 MPa, whereas the elongation at break did not change. The ILs increased the tensile strength of the vulcanisates by 2–5 MPa compared with the vulcanisate containing only nanosized zinc oxide. The elongation at break was reduced for vulcanisates with a higher crosslink density than that of the reference nZnO-containing vulcanisate. The highest tensile strength was achieved for vulcanisates with pyridinium hexafluorophosphate and tetrafluoroborate and pyrrolidinium hexafluorophosphate and bromide.

The dynamic mechanical properties are important for the application of rubber products. The rigidity and strength of vulcanisates should be stable and the material must be able to dampen vibration. The influence of ILs on the loss factor (tan δ) was determined with DMA. The loss factor tan δ as a function of temperature for the vulcanisates containing ILs is presented in Figure 2. The presence of one transition can be observed. This is the glass transition of the NBR elastomer, with a maximum that represents the glass transition temperature T_g.

The values of the glass transition temperature and the loss factor at T_g, room temperature and an elevated temperature (100°C) are compiled in Table 6. The glass transition temperature of NBR containing the standard activator – microsized zinc oxide – was –7.3°C. Applying nanosized zinc oxide increased the glass transition temperature of the elastomer because of the higher crosslink density of the vulcanisate. The ILs caused a further small increase in the T_g of
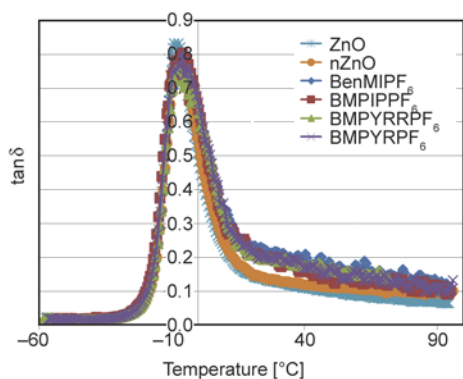
Figure 2. Loss factor (tan δ) versus temperature for NBR vulcanisates containing ILs

Table 6. Glass transition temperature and loss factor of NBR vulcanisates containing ILs

ILs	T_g [°C]	tan δ at T_g [–]	tan δ at 25°C [–]	tan δ at 100°C [–]
ZnO	−7.3	0.58	0.11	0.06
nZnO	−6.5	0.69	0.13	0.10
BMPYRRPF$_6$	−5.7	0.78	0.14	0.10
BenMIPF$_6$	−5.2	0.77	0.22	0.11
BMPYRPF$_6$	−6.2	0.80	0.20	0.11
BMPIPPF$_6$	−6.0	0.80	0.20	0.10

T_g – glass transition temperature; tan δ – loss factor.

the vulcanisates, which was the result of the cross-linked elastomer network that formed during vulcanisation and restricted the mobility of the elastomer chains. The nanosized zinc oxide and the ILs increased the loss factor at T_g, room and elevated temperatures. It is hypothesised that these vulcanisates would demonstrate better damping properties at the examined temperatures.

3.4. Thermal stability and ageing resistance of vulcanisates

Thermal stability and ageing resistance are important properties of rubber products for technological applications. ILs are used to improve the dispersion degree of zinc oxide and silica in the elastomer should not deteriorate these properties. The thermal stability of the vulcanisates was based on the decomposition temperature and total weight loss of the sample determined by TGA analysis. The results are presented in Table 7.

The thermal decomposition of the vulcanisate containing microsized zinc oxide began at 300°C. Replacing the standard activator with nanosized zinc oxide significantly improved the thermal stability of NBR. The decomposition of the vulcanisate started at a temperature that was 50°C higher than that of

Table 7. Decomposition temperatures at a weight loss of 2% (T_{02}), 5% (T_{05}), and 50% (T_{50}) and the total weight loss during decomposition of NBR vulcanisates containing ILs

ILs	T_{02} [°C]	T_{05} [°C]	T_{50} [°C]	Total weight loss [%]
ZnO	300	368	446	68.5
nZnO	350	377	458	70.6
EMPYRRPF$_6$	372	394	465	68.8
BMPYRRPF$_6$	370	392	465	68.9
BenMIPF$_6$	370	390	465	68.9
BMPYRPF$_6$	372	393	465	69.0
BMPIPPF$_6$	369	391	464	69.0

the reference vulcanisate. The use of ILs caused a further increase in the thermal stability of NBR, possibly because of the homogeneous dispersion of the nanoparticles in the elastomer matrix. The network created by the filler particles may be a barrier for the transport of gases and volatile pyrolysis products, thus increasing the thermal stability of the material. ILs also increased the temperatures at 5 and 50% weight loss. The 5% weight loss was achieved at the temperature range of 390–394°C, and 50% weight loss occurred at 464–465°C. The total weight loss during decomposition was similar for all vulcanisates (68.5–70.6%).

After establishing the effects of nanosized zinc oxide and ILs on the thermal stability, we then examined the vulcanisates' resistance to thermo-oxidative and UV ageing. The effect of ILs on ageing resistance was studied through the changes in the mechanical properties and the crosslink density of the vulcanisates.

In Figure 3, the change in crosslink density upon thermo-oxidative and UV ageing is reported for the vulcanisates containing hexafluorophosphates. The ageing process increased the crosslink density of the vulcanisates. This effect was particularly evident in the case of thermo-oxidative ageing. The increase
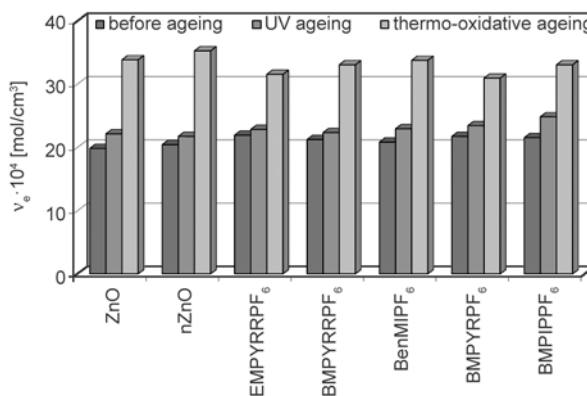

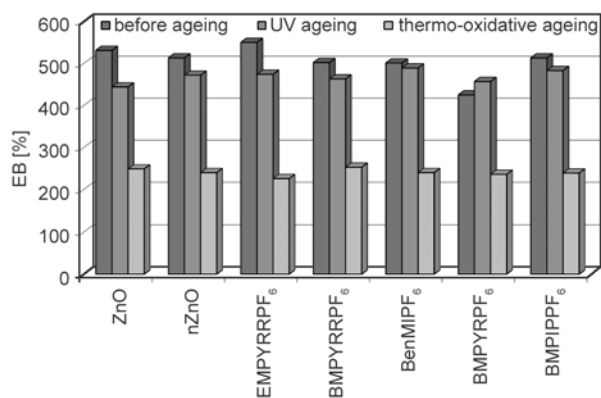**Figure 3.** Vulcanisate crosslink density after ageing

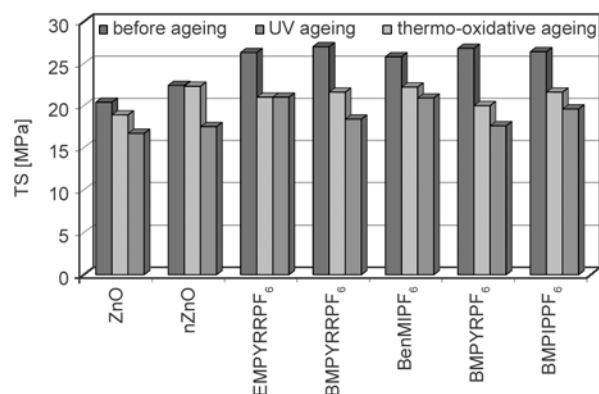**Figure 4.** Vulcanisate elongation at break after ageing

Figure 5. Vulcanisate tensile strength after ageing

in crosslink density resulted in the reduction of the vulcanisates' elongation at break (approximately 300% for thermo-oxidative ageing) (Figure 4.) The vulcanisates became more rigid and brittle, corresponding to a reduction of their tensile strength (Figure 5).

It was difficult to estimate the resistance of the vulcanisates to the ageing process using changes in tensile strength and the elongation at break separately. Therefore, the ageing factor S was calculated to quantitatively estimate the change in the mechanical properties of the vulcanisates (Table 8). The ageing factor could be defined as the change in the deformation energy of the material as a result of the ageing process.

The nanosized zinc oxide and the ILs had no considerable influence on the vulcanisates' resistance to thermo-oxidative and UV ageing. A small improvement in the UV ageing resistance was observed for BMPYRCl and BMPIPBF$_4$. The S_{UV} values are significantly higher than the S_T values, indicating that prolonged exposure to elevated temperature is more

Table 8. Thermo-oxidative and UV ageing factors for NBR vulcanisates containing ILs

ILs	S_T [–]	S_{UV} [–]
ZnO	0.43	0.68
nZnO	0.47	0.72
EMPYRRBr	0.39	0.65
EMPYRRPF$_6$	0.38	0.66
BMPYRRCl	0.43	0.59
BMPYRRBr	0.41	0.78
BMPYRRPF$_6$	0.40	0.73
BMPYRRBF$_4$	0.38	0.65
BenMICl	0.49	0.72
BenMIPF$_6$	0.41	0.79
BenMIBF$_4$	0.41	0.59
BMPYRCl	0.46	0.81
BMPYRPF$_6$	0.41	0.71
BMPYRBF$_4$	0.42	0.69
BMPIPPF$_6$	0.38	0.70
BMPIPBF$_4$	0.41	0.82

S_T – thermo-oxidative ageing factor; S_{UV} – UV ageing factor.

destructive to material properties than UV radiation.

4. Conclusions

Ionic liquids (alkylpyrrolidinium, alkylpyridinium, alkylpiperidinium and benzylimidazolium salts) were used to improve the dispersion degree of a nanosized vulcanisation activator (zinc oxide) and filler (silica). The use of ILs allowed for the homogeneous dispersion of nanoparticles in the elastomer matrix and resulted in the shortening of the optimal vulcanisation time. Chlorides, bromides and tetrafluoroborates decreased the vulcanisation onset temperature by 20°C. ILs increased the vulcanisates' tensile strength compared with the vulcanisate that contained only nanosized zinc oxide. IL-containing vulcanisates also demonstrated better thermal stability and damping properties at the usage temperature. ILs did not affect the resistance of the vulcanisates to thermo-oxidative and UV ageing.

Using nanosized zinc oxide with ILs reduced the amount of zinc ions by 60% compared with conventional rubber compounds containing 5 phr of microsized ZnO as is required by the European Union legislation.

References

[1] Nieuwenhuizen P. J., van Veen J. M., Haasnoot J. G., Reedijk J.: Homogeneous zinc(II) catalysis in accelerated vulcanization IV. The Mechanism of cross-link (de)sulfuration. Rubber Chemistry and Technology, **72**, 43–54 (1999).
DOI: 10.5254/1.3538793

[2] Nieuwenhuizen P. J.: Zinc accelerator complexes.: Versatile homogeneous catalysts in sulfur vulcanization. Applied Catalysis A: General, **207**, 55–68 (2001).
DOI: 10.1016/S0926-860X(00)00613-X

[3] Lu J., Yan F., Texter J.: Advanced applications of ionic liquids in polymer science. Progress in Polymer Science, **34**, 431–448 (2009).
DOI: 10.1016/j.progpolymsci.2008.12.001

[4] Chapman A., Johnson T.: The role of zinc in the vulcanisation of styrene-butadiene rubbers. Kautschuk und Gummi Kunststoffe, **58**, 358–361 (2005).

[5] Przybyszewska M., Zaborski M.: The vulcanizates containing a reduced amount of zinc oxide. Przemysl Chemiczny, **85**, 976–978 (2006).

[6] Przybyszewska M., Zaborski M.: Effect of ionic liquids and surfactants on zinc oxide nanoparticle activity in crosslinking of acrylonitrile butadiene elastomer. Journal of Applied Polymer Science, **116**, 155–164 (2010).
DOI: 10.1002/app.31519

[7] Przybyszewska M., Krzywania A., Zaborski M., Szynkowska M. I.: Surface properties of zinc oxide nanoparticles studied by inverse gas chromatography. Journal of Chromatography A, **1216**, 5284–5291 (2009).
DOI: 10.1016/j.chroma.2009.04.094

[8] Fukushima T., Aida T.: Ionic liquids for soft functional materials with carbon nanotubes. Chemistry – A European Journal, **13**, 5048–5058 (2007).
DOI: 10.1002/chem.200700554

[9] Ma P-C., Siddiqui N. A., Marom G., Kim J-K.: Dispersion and functionalization of carbon nanotubes for polymer-based nanocomposites: A review. Composites Part A: Applied Science and Manufacturing, **41**, 1345–1367 (2010).
DOI: 10.1016/j.compositesa.2010.07.003

[10] Jiang M-J., Dang Z-M., Xu H-P.: Significant temperature and pressure sensitivities of electrical properties in chemically modified multiwall carbon nanotube/methylvinyl silicone rubber nanocomposites. Applied Physics Letters, **89**, 182902/1–182902/2 (2006).
DOI: 10.1063/1.2369643

[11] Das A., Stöckelhuber K. W., Jurk R., Fritzsche J., Klüppel M., Heinrich G.: Coupling activity of ionic liquids between diene elastomers and multi-walled carbon nanotubes. Carbon, **47**, 3313–3321 (2009).
DOI: 10.1016/j.carbon.2009.07.052

[12] Subramaniam K., Das A., Heinrich G.: Development of conducting polychloroprene rubber using imidazolium based ionic liquid modified multi-walled carbon nanotubes. Composites Science and Technology, **71**, 1441–1449 (2011).
DOI: 10.1016/j.compscitech.2011.05.018

[13] Steinhauser D., Subramaniam K., Das A., Heinrich G., Klüppel M.: Influence of ionic liquids on the dielectric relaxation behavior of CNT based elastomer nanocomposites. Express Polymer Letters, **6**, 927–936 (2012).
DOI: 10.3144/expresspolymlett.2012.98

[14] Kreyenschulte H., Richter S., Götze T., Fischer D., Steinhauser D., Klüppel M., Heinrich G.: Interaction of 1-allyl-3-methyl-imidazolium chloride and carbon black and its influence on carbon black filled rubbers. Carbon, **50**, 3649–3658 (2012).
DOI: 10.1016/j.carbon.2012.03.037

[15] Goujon L. J., Khaldi A., Maziz A., Plesse C., Nguyen G. T. M., Aubert P-H., Vidal F., Chevrot C., Teyssié D.: Flexible solid polymer electrolytes based on nitrile butadiene rubber/poly(ethylene oxide) interpenetrating polymer networks containing either LiTFSI or EMITFSI. Macromolecules, **44**, 9683–9691 (2011).
DOI: 10.1021/ma201662h

[16] Shaplov A. S., Ponkratov D. O., Vlasov P. S., Lozinskaya E. I., Malyshkina I. A., Vidal F., Aubert P-H., Armand M., Vygodskii Y. S.: Solid-state electrolytes based on ionic network polymers. Polymer Science Series B, **56**, 164–177 (2014).
DOI: 10.1134/S1560090414020134

[17] Marwanta E., Mizumo T., Nakamura N., Ohno H.: Improved ionic conductivity of nitrile rubber/ionic liquid composites. Polymer, **46**, 3795–3800 (2005).
DOI: 10.1016/j.polymer.2005.02.113

[18] Lei Y. D., Tang Z. H., Guo B. C., Zhu L. X., Jia D. M.: Synthesis of novel functional liquid and its application as a modifier in SBR/silica composites. Express Polymer Letters, **4**, 692–703 (2010).
DOI: 10.3144/expresspolymlett.2010.84

[19] Guo B., Chen F., Lei Y., Liu X., Wan J., Jia D.: Styrene-butadiene rubber/halloysite nanotubes nanocomposites modified by sorbic acid. Applied Surface Science, **255**, 7329–7336 (2009).
DOI: 10.1016/j.apsusc.2009.03.092

[20] Flory P. J., Rehner J.: Statistical mechanics of crosslinked polymer networks II. Swelling. Journal of Chemical Physics, **11**, 521–526 (1943).
DOI: 10.1063/1.1723792

[21] Masek A., Zaborski M., Kosmalska A.: Derivatives of flavonoides as anti-ageing substances in elastomers. Comptes Rendus Chimie, **14**, 483–488 (2011).
DOI: 10.1016/j.crci.2011.01.001

New crosslinked cast films based on poly(vinyl alcohol): Preparation and physico-chemical properties

C. Birck[1,2]*, S. Degoutin*[1,2]*, N. Tabary*[1,2]*, V. Miri*[1,2]*, M. Bacquet*[1,2]*

[1]Unité des Matériaux et Transformations (UMET), CNRS UMR 8207, Equipe ISP, Université Lille 1, 59655 Villeneuve
 d'Ascq, France
[2]Université Lille Nord de France, 59000 Lille, France

Abstract. In this paper, we propose a green route to prepare insoluble poly(vinyl alcohol) (PVOH) cast films with potential application as antimicrobial packaging. First PVOH films were cast from different aqueous solutions and analyzed by Differential Scanning Calorimetry (DSC) and Dynamic Mechanical Analysis (DMA) to determine their physical properties under two storage conditions. In order to obtain insoluble films, PVOH was then crosslinked by citric acid (CTR) as confirmed by Nuclear Magnetic Resonance (NMR) analyses. The crosslinking reaction parameters (curing time, crosslinker content) were studied by comparing the characteristics of PVOH/CTR films, such as free COOH content and glass transition temperature (T_g) value, as well as the impact of the crosslinking reaction on mechanical properties. It was found that for 40 and 10 wt% CTR contents, 120 and 40 min of crosslinking times were necessary to bind all CTR respectively. Brittle films were obtained for 40 wt% CTR whereas 10 wt% CTR content led to ductile films. Finally, films containing hydroxypropyl-β-cyclodextrin (HPβCD), chosen as a potential vector of antimicrobial agent, were prepared. The obtained results show that the incorporation of HPβCD in the PVOH matrix does not mainly influence the physical and mechanical properties of the films.

Keywords: mechanical properties, poly(vinyl alcohol), cyclodextrin, crosslinking, cast films

1. Introduction

Poly(vinyl alcohol) (PVOH) is a non-toxic, biodegradable polymer used in food packaging applications owing to its high barrier properties to oxygen and carbon dioxide [1, 2]. However, due to its solubility in water, it is often combined with other polymers in multilayer structures, PVOH being located in the core layer. An alternative route to avoid the use of several polymers would be the crosslinking of PVOH. For this polymer, the most commonly used crosslinkers are dialdehydes, such as glyoxal [3] or glutaraldehyde [4, 5] and polycarboxylic acids. Among the latter, citric acid (CTR) [6, 7], succinic acid [8] and tartaric acid [9] have the advantage of being used as food additives. In partic-

ular, citric acid (food additive European code E330) is interesting for its low price. It is also well-known as crosslinking agent for compounds bearing hydroxyl groups (like polysaccharides and cyclodextrins) as already reported by our group [10, 11].
The aim of this study is to prepare antimicrobial films for food industry, which is emerging in the area of active packaging [12]. In order to confer a prolonged antimicrobial activity to PVOH crosslinked films, we develop an original approach which consists in adding cyclodextrin in the PVOH matrix. Cyclodextrins present several advantages for our application. These biodegradable cyclic oligosaccharides can be used to form inclusion complexes with antimicrobial agents, in order to release it onto

---

the surface of the food [13–15]. The hydroxypropyl-β-cyclodextrin (HPβCD), selected for this study, is a derivative of the β-cyclodextrin (food additive E 459) and is non-toxic [16].

The objective of this work is to prepare new films based on PVOH and HPβCD, crosslinked by CTR via a green route. In order to optimize the preparation, different processing parameters such as the PVOH dilution ratio, the formulation of the initial batches with or without cyclodextrin and the crosslinking reaction time are studied. Relationships between processing and physico-chemical properties are investigated using several characterization techniques. The release kinetics of an active principle and the antibacterial activity of the optimized films will be discussed in a following paper.

2. Experimental procedures
2.1. Materials
Poly (vinyl alcohol) (PVOH, M_w = 31 000–50 000 g·mol^{-1}, 87–89% hydrolysis, powder) was purchased from Aldrich Chemicals (St. Quentin Fallavier, France). Hydroxypropyl-β-cyclodextrin (HPβCD) was provided by Roquette (Lestrem, France). This derivative of β-cyclodextrin (βCD) is very soluble in water (>1000 g/L). The mean Molar Substitution (MS), which is the average number of hydroxypropyl groups per anhydroglucose unit, is 0.65. Citric acid (CTR), sodium hydroxide and calcium acetate were commercial chemical grade products, supplied by Aldrich Chemicals.

2.2. Films preparation
For non-crosslinked PVOH films, PVOH was dissolved in distilled water at three concentrations (1, 5, 17 wt%) by mechanical agitation with helical blade (150 rpm), in the temperature range 75–90°C during 3 to 5 hours. The homogeneous solution was then slowly cooled at room temperature, cast onto a silicone plate and dried under a hood for 16 hours. To study the effect of PVOH dilution, a non-crosslinked PVOH film was prepared by compression molding at 220°C, 50 bars, and cooled down to room temperature at 1°C/min.

For crosslinked PVOH/CTR films, CTR was added in the homogeneous PVOH solution. The final reagents concentration was equal to 5 wt%. The solution was stirred by mechanical agitation and cast, using similar conditions as previously described. Once the film was formed, the crosslinking reaction

was achieved through a heat treatment at 130±1°C during increasing times (from 0 to 960 min). Two relative weight compositions of PVOH/CTR films were prepared: 90/10 and 60/40.

Crosslinked PVOH/CTR/HPβCD films, in weight proportions 80/10/10, were prepared following the same protocol as for films without HPβCD. The proportion of HPβCD in the film was fixed considering first an equimolar complex between HPβCD and the later added antimicrobial agent and secondly according to the European directive giving a limit for constituent's migration in food packaging at 10 mg/dm^2 [17].

The thickness of each film was 120±20 μm.

Two storage conditions have been used for the films. Dried films were obtained by keeping them at 60°C during 16 hours under vacuum. Hydrated films were obtained by conditioning at 58% Relative Humidity (R.H.) during three days (room temperature in an environmental chamber in the presence of NaBr saturated solutions).

2.3. Thermogravimetric analysis (TGA)
TGA was used to determine the water content and the thermal degradation of films. Experiments were performed on a TA Q50 (TA Instruments, United States) apparatus from ambient to 600°C with a heating rate of 5°C/min. The sample was placed in an open platinum pan under nitrogen.

2.4. Differential scanning calorimetry (DSC)
DSC measurements were performed on a TA Q100 (TA Instruments, United States) apparatus under ultra-pure nitrogen at a heating rate of 10°C/min. PVOH and PVOH/CTR films (with or without HPβCD) were analyzed, during the first heating, from –70 to 220°C and to 150°C, respectively. The glass transition temperature (T_g) was taken at the onset of the heat capacity jump and the melting point (T_m) at the maximum of the endothermic peak. The crystallinity degree (X_c) was calculated using the value of 162 J/g which is the most cited reference melting enthalpy for PVOH crystals [18–20]. Three replicates were analyzed for each film.

2.5. X-ray diffraction (XRD)
Wide-angle-X-ray scattering (WAXS) analysis was performed using a Rigaku rotating anode equipment (Rigaku, Japan) operating at 50 kV and 100 mA. The Cu Kα radiation (λ = 1.54 Å) was selected with a

point focusing monochromator. The WAXS patterns were recorded on MAR2300 imaging plates. Radial Intensity Profiles, $I(2\theta)$, were obtained by azimuthal integration of the 2D patterns.

2.6. Dynamic mechanical analysis (DMA)

DMA measurements were performed on a Rheometrics RSA III (TA Instruments, United States) apparatus operating in tensile mode at a frequency of 1 Hz using a dynamic strain amplitude $\varepsilon_0 = 0.05\%$ in the temperature range $-50°C < T < 150°C$. Specimens with gauge width and length 6 mm×10 mm were cut out from the films of PVOH crosslinked or not.

2.7. Uniaxial tensile measurements

Uniaxial Tensile testing was conducted on a 4466 Instron (Instron, United Kingdom) machine at room temperature (22°C) using specimens with 24 and 5 mm of gauge length and width, respectively. The tensile tests were carried out at a constant crosshead speed of 14.4 mm·min^{-1} which corresponds to an initial strain rate of 0.01 s^{-1}. The nominal stress σ_N and the nominal strain ε_N were defined as conventionally by the ratio of the force per the initial cross-section and the elongation per the initial length of the sample, respectively. Three replicates have been analyzed for each film.

2.8. Nuclear magnetic resonance (NMR)

^{1}H NMR was used to check the presence of unreacted reagents in films. Each film was immersed in water during 3 days under agitation. Once the film was removed, the solution containing released reagents was freeze-dried. The obtained solid was dissolved in D$_2$O and freeze-dried again. The final obtained solid was dissolved in D$_2$O and analyzed by ^{1}H NMR using a spectrometer Bruker Avance™ (Bruker Corporation, Germany) 300 MHz at room temperature.

2.9. Free COOH groups quantification

This quantification was undertaken by Ion Exchange Capacity (*IEC*) method through pH-metric titration using calcium acetate [21]. Each sample was dried 16 hours at 60°C before titration. Typically, 0.1 g of film sample was stirred in 100 mL of a calcium acetate solution during 2 hours. The formed acetic acid was titrated by a standard NaOH solution. The

amount of carboxylic functions was calculated following the Equation (1):

$$IEC\,[\mathrm{mmol/g}] = \frac{C_{\mathrm{b}}[\mathrm{mmol/mL}] \cdot V_{\mathrm{e}}[\mathrm{mL}]}{sample\ weight[\mathrm{g}]} \qquad (1)$$

where C_{b} and V_{e} correspond to the concentration and the equivalent volume of the NaOH solution respectively. Three replicates were undertaken for each film.

3. Results and discussion

A TGA study concerning the thermal behavior of the initial reagents was first carried out (Figure 1). We noticed the lower degradation temperature of CTR (170°C) compared to the other reagents. Thus, the compression molding method at 220°C is not suitable for the preparation of PVOH/CTR films. Therefore, the solvent casting method was chosen as an alternative route for the preparation of our films.
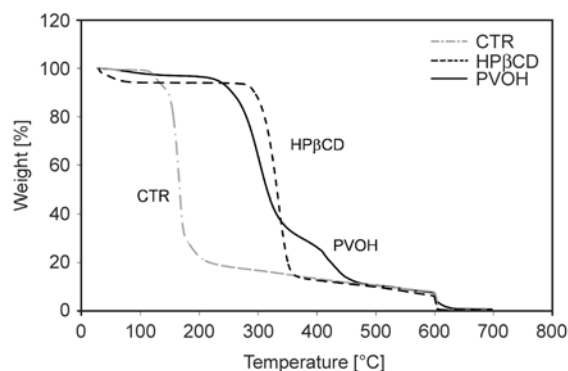

Figure 1. TGA profiles of initial reagents

3.1. Effect of dilution on the physical properties of non-crosslinked PVOH films

Polymer dilution is expected to involve a disentanglement of the polymer coils. This phenomenon may induce an increase of crystallinity. This disentanglement may also affect drawability. At high dilution ratio, there is not enough entanglement to ensure a physical crosslinked network behavior, inducing a decrease of the drawability. So a preliminary study was carried out to investigate the effect of dilution on thermal and mechanical properties of PVOH films, in order to fix the optimal dilution ratio for the further study.

The impact of the dilution ratio during the cast preparation on these thermal transitions is detailed in Table 1. Results for the thermocompression molded film are included for the sake of comparison.

Table 1. Thermal characteristics of cast and molded films dried or conditioned at 58% R.H.

| Concentration [%w/w]	Cast films						Molded film	
	1		5		17			
Conditioning	dried	58% R.H.	dried	58% R.H.	dried	58% R.H.	dried	58% R.H.
wt% water*	2±2	8±1	1±1	8±1	2±1	7±2	1±1	7±1
T_g [°C]	57±4	7±1	57±1	7±1	41±5	6±1	53±1	6±1
T_m [°C]	192±1	193±1	192±1	193±1	192±1	193±1	192±1	193±1
X_c [%]**	26±1	18±2	25±1	16±1	19±2	11±2	14±1	8±2

*water content determined by TGA
**X_c = crystallinity degree

As regards T_g and T_m, no major difference is observed whatever the film preparation method. In the dried conditions (corresponding to 2±1 wt% of water in the samples), films are characterized by a T_g around 55°C and a melting point T_m at 193°C. For comparison, the reported values for partially hydrolyzed PVOH are 80±5°C for T_g and 185±5°C for T_m [1]. In the present study, these relatively 'low' transition temperatures could be explained by the presence of acetate in this hydrolyzed PVOH (87–89%). Under 58% R.H. conditions (corresponding to about 10 wt% of water), compared to dried one, a T_g drop is observed for all samples, relevant to the plasticizer effect of water molecules which disrupt molecular hydrogen bonds between PVOH chains in the amorphous phase.

Crystallinity is higher for cast films than for the molded ones, and tends to increase with the dilution ratio. This phenomenon may be attributed to the effect of disentanglements with dilution which promotes crystallization, as expected [22]. With humidity, a significant decrease of X_c is observed for all samples, suggesting that water molecules destroy crystals. This is consistent with results already reported in literature which have shown that water dissolves gradually crystallites by attacking them at the crystalline/amorphous interface [23].

The evolution of the storage modulus, E', and loss factor tan δ, as a function of temperature for molded and PVOH 5 wt% cast films is presented in Figure 2. In the studied temperature range, all samples exhibit only one relaxation characterized by a pronounced decrease of E' and a damping peak of tan δ. This phenomenon is assigned to the main α_a relaxation associated with the glass transition [24, 25]. As shown in Figure 2, this relaxation is rather independent of film preparation but is very sensitive to water content, in good agreement with DSC results. The peak temperature of tan δ decreases from 65°C to about 20°C for dried and 58% R.H. films, respectively. Note
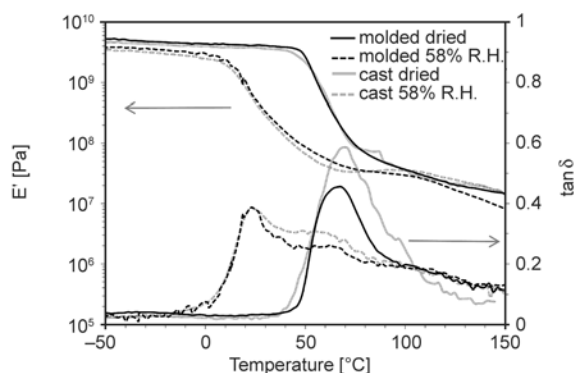
Figure 2. Dynamic mechanical response as a function of temperature of molded and 5 wt% cast PVOH films in dried and 58% R.H. conditions

that the broadness of the peak for humid samples comes from the water evaporation during the experiment.

The yield stress σ_y and the strain at break ε_{break} values of PVOH films conditioned at 58% R.H. are reported in Table 2. No result is reported for dried films because, in this case, all samples exhibit a very brittle behavior, related to the drawing temperature well below T_g.

All samples display a ductile behavior. No major influence of film preparation on the strain at break is noticed while an increase of σ_y is observed as initial PVOH concentration increases. One may have expected the reverse evolution considering the variation of the crystal content with the polymer concentration (Table 1). This shows that other structural parameters, than only the crystal content, play an important role in the initiation of plasticity, such as the number of tie molecules.

To sum up, these results do not show any significant difference between all cast films regarding struc-

Table 2. Mechanical data measured for the different films

PVOH concentration [%w/w]	Cast films			Molded film
	1	5	17	
σ_y [MPa]	10.3±0.6	9.1±0.3	13.8±1.8	14.7±1.5
ε_{break} [%]	126±18	140±16	127±32	120±36

tural and thermomechanical characterizations. These cast films exhibit similar behavior as the molded film. For the following studies, films will be prepared from a total concentration of reactants of 5 wt%, which is the easiest to process in terms of viscosity.

3.2. Influence of crosslinker amount and crosslinking time on structure of PVOH/CTR films

The crosslinking reaction involved in this study consists in the esterification between hydroxyl functions of PVOH and carboxylic functions of CTR as presented in Figure 3a.

The esterification is activated by the preformation of CTR anhydride under the heat treatment. The CTR being a triacid, residual COOH are present in the three-dimensional network at the end of the reaction. Previous works showed that the esterification occurs from 130°C [11].

A constant temperature of 130±1°C was applied for all this study. Two weight proportions of CTR (10 and 40 wt%) representative of low and high crosslinker contents were chosen. For both cases, there is an excess of OH due to PVOH compared with COOH functions. Indeed, there are 10 functions OH for 1 function COOH for 10 wt% CTR films, and 2 functions OH for 1 function COOH in 40 wt% CTR films. The reaction time varied from 0 to 960 min.

As shown on Figure 3b, films are transparent. Visual observations showed that the yellowing and the brittleness increase with CTR content and crosslinking time. With 10 wt% CTR, there is a slight yellowing from 120 min and films are never brittle. With 40 wt% CTR, yellowing is observed from 40 min. Films are brittle from 60 min. The yellowing is due to CTR dehydration and formation of a double bond sensitive to oxidation [26].

To check the efficiency of covalent bonding of the different reagents, eventual unreacted CTR and PVOH were obtained by D_2O extraction of PVOH/CTR films. The ^1H NMR spectra of residual reagents in relation to crosslinking time is presented on Figure 4 (range 4–0 ppm).

The magnitude of the signal for soluble part of the films has been amplified in order to reveal eventual residual compounds and compared to initial reagents. The chemical shifts for PVOH and CTR were attributed to protons also represented on Figure 4.
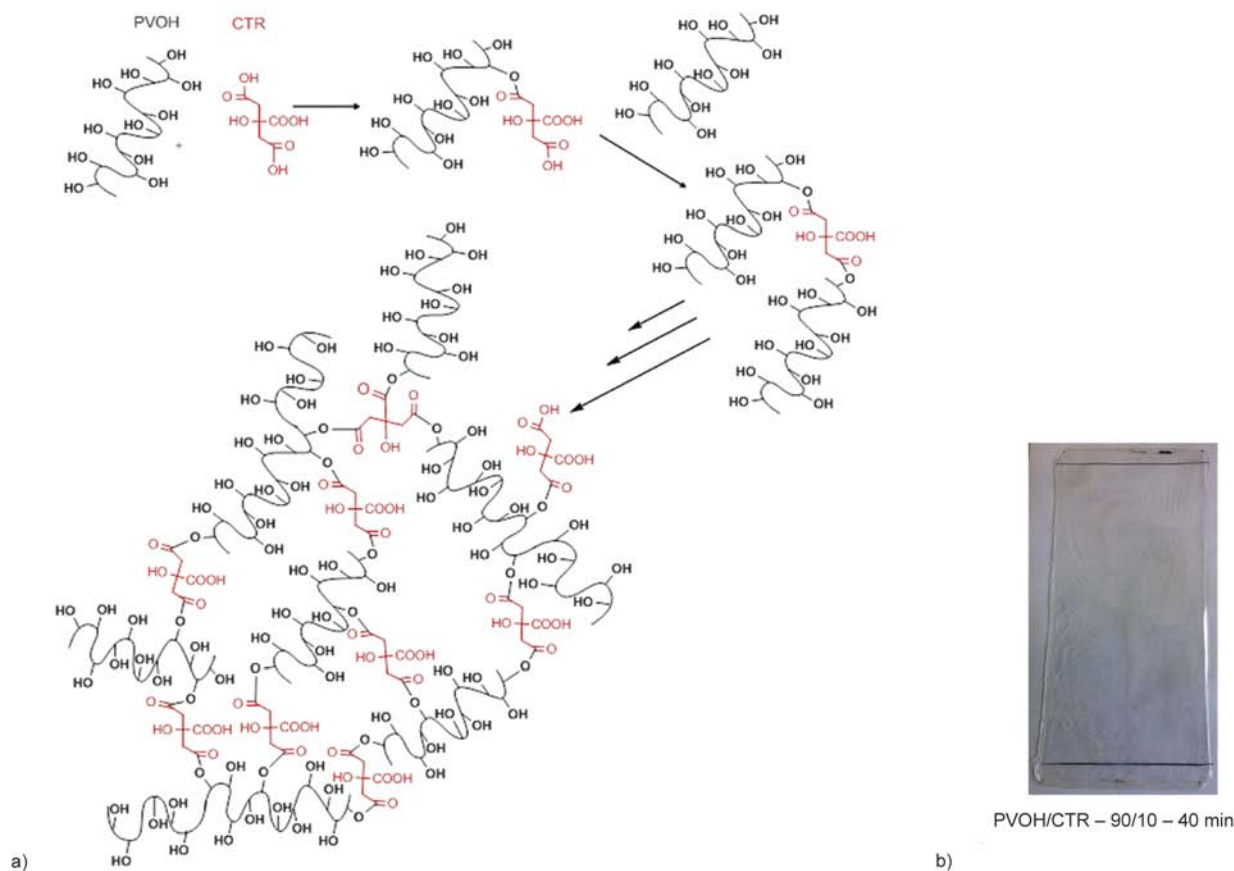

PVOH/CTR – 90/10 – 40 min

Figure 3. (a) Expected reaction between PVOH and CTR and (b) picture of PVOH/CTR 90/10 film
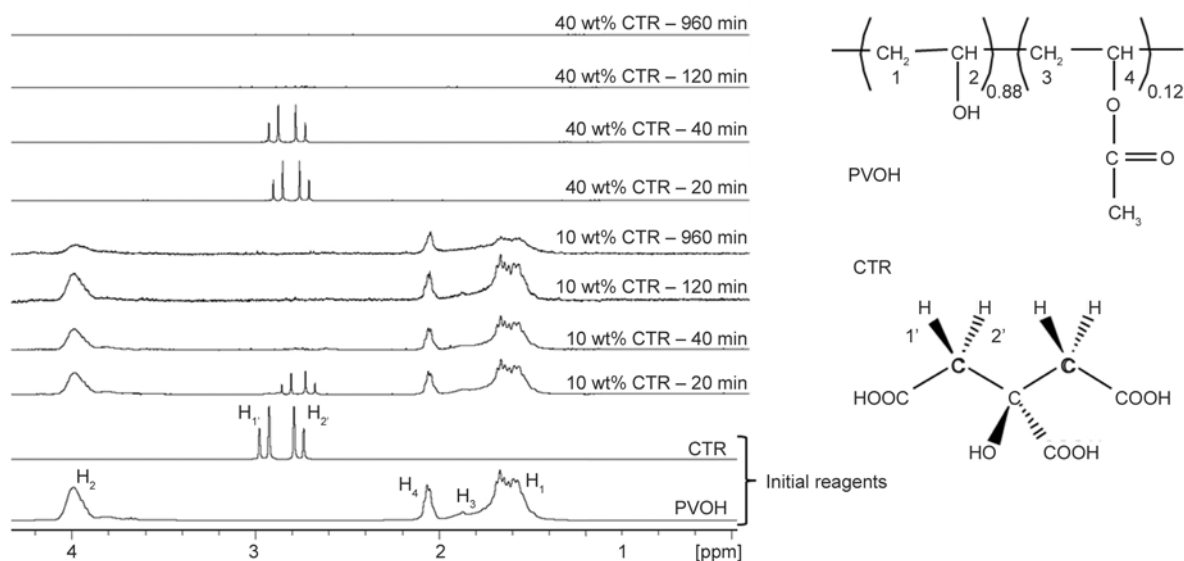
Figure 4. Comparison of ^{1}H NMR spectra for residual reagents in PVOH/CTR films related to CTR ratio and reaction time and protons of CTR and PVOH 88%

We notice that the quantity of residual compounds progressively decreases with crosslinking time. For 40 wt% CTR films, PVOH is not detected after 20 min as well as CTR after 120 min. This means that for this CTR content, a crosslinking time of 120 min is necessary to bind all CTR to PVOH matrix. For 10 wt % CTR films, after 40 minutes, CTR is not detected whereas PVOH is still present after 960 min. This indicates that for 10 wt% CTR, even after 960 min, a weak amount of non crosslinked PVOH chains remains in the films. Nevertheless, the amount of those residual compounds for all the films up to 120 min is very low (less than 0.1%, determined by weight measurements).

It is well known that the glass transition of the crosslinked polymers depends not only on the main chain rigidity, but also on crosslinking density. In this study, the effect of crosslinking conditions on the PVOH/CTR network is thus investigated considering the evolution of the glass transition. In Figure 5a, typical thermograms for several crosslinking times are shown for both kinds of films. All samples exhibit a heat capacity jump, which is clearly curing time-dependent. The evolution of T_g as a function of crosslinking time is represented on Figure 5b for both storage conditions.

In the case of non crosslinked films (time = 0 min), a plasticizer effect of CTR is observed whatever the storage conditions. As expected, this effect is more pronounced for higher CTR concentration. In dried conditions, PVOH exhibits a T_g at 57°C, while this latter decreased to 42°C and 28°C for PVOH/CTR-90/10 and PVOH/CTR-60/40 respectively. Similar drop is observed for hydrated non crosslinked films.
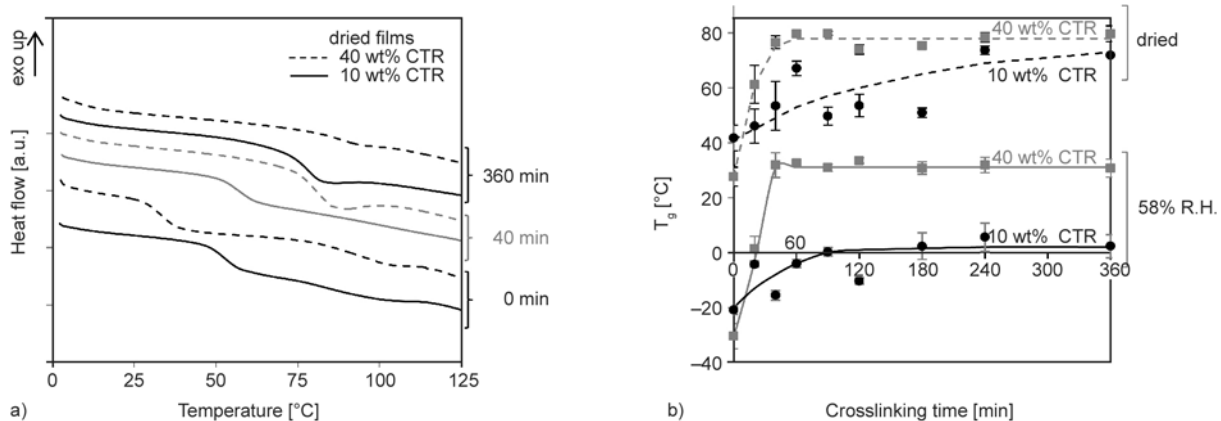

Figure 5. Effect of crosslinking parameters and storage conditions on T_g for different PVOH/CTR films: (a) DSC profiles and (b) T_g as a function of crosslinking time

Then, the T_g progressively increases with crosslinking time for both proportions of CTR. This increase is slower for 10 wt % CTR than for 40 wt% CTR films. In the latter case, an abrupt rise of T_g is observed followed by a leveling off beyond 60 min of heating whatever the storage conditions. Considering that T_g increases with crosslink density, this may suggest that no major evolution of the PVOH/CTR-60/40 network structure occurs above a curing time of 60 min. However, one can observe a decrease of the heat capacity jump ΔC_p from a crosslinking time of 40 to 360 min. Note that this effect does not occur for PVOH-CTR 90-10. This observation may indicate that the amorphous phase content which relaxes at T_g decreases with crosslinking time for the PVOH/CTR-60/40. Several assumptions could be proposed to explain this result. An increase of crystallinity has been rejected because no ordered phase is evidenced for 40 wt% CTR whatever the crosslinking time, as it will be shown later. A subsequent crosslinking reaction inducing a restriction of the molecular motions between chemical entanglements is suggested and will be discussed further below.

For dried films, the value of T_g with high crosslinking time (from 240 min) is surprisingly quite similar for both CTR concentrations. However, T_g rise for 90/10 films is not so smooth. In fact in the dried state, T_g results from several main combining parameters: the crosslinking density and the hydrogen bonds between hydroxyl groups of PVOH chains but also the intrinsic flexibility of PVOH and CTR chains. As shown in literature, these two parameters acted by a compensation effect between the weakening of the chemical network and the plasticizing effect of the introduced more or less flexible linkers [27]. When films are hydrated and swollen under equilibrium, the decreasing gap of T_g for 10 wt% CTR is much more pronounced than the one for 40 wt% CTR. Indeed, the greater proportion of

PVOH hydroxyl groups is, the more they could interact with water molecules resulting in a more pronounced plasticizer effect of water.

The quantification of residual (or free) COOH groups could also provide some additional information about the formation of the PVOH-CTR network. The esterification reaction, catalyzed by intramolecular CTR anhydride formation (Figure 6) highlighted the origin of these free COOH groups. If CTR is consumed according to this intramolecular mechanism, namely 2/3 COOH functions have reacted. Then, the final theoretical COOH amount values should be around 0.5 and 1.9 mmol/g for PVOH/CTR-90/10 and PVOH/CTR-60/40 films respectively.

The comparison of free COOH quantification and T_g evolution for the two films is given on Figure 7. As expected, free COOH functions amount decreases with crosslinking time for both proportions of CTR. A higher decrease is obviously observed for films with 40 wt% CTR. After 120 minutes, the amount of residual COOH functions remains constant regardless initial amount of CTR. At this crosslinking time, all CTR is covalently bound as previously proved by NMR (Figure 4). For PVOH/CTR-90/10 (Figure 7a), the experimental value (0.60±0.12 mmol/g) is close to the theoretical one (0.5 mmol/g). Note that the plateau for T_g and residual COOH are reached for the same crosslinking time (90 min). In the case of PVOH/CTR-60/40 (Figure 7b), the behavior is different. First the COOH experimental value at the plateau (0.76±0.13 mmol/g) is lower than the theoretical one (1.9 mmol/g). Then, the maximum in T_g is achieved from around 40–60 min while at this time COOH value is still decreasing. In addition, we notice that at 40–60 min, the COOH value is about 2–3 mmol/g and close to the calculated one according to the crosslinking mechanism. This can be explained by the fact that for high proportions of CTR, the esterification occurred in two steps. The
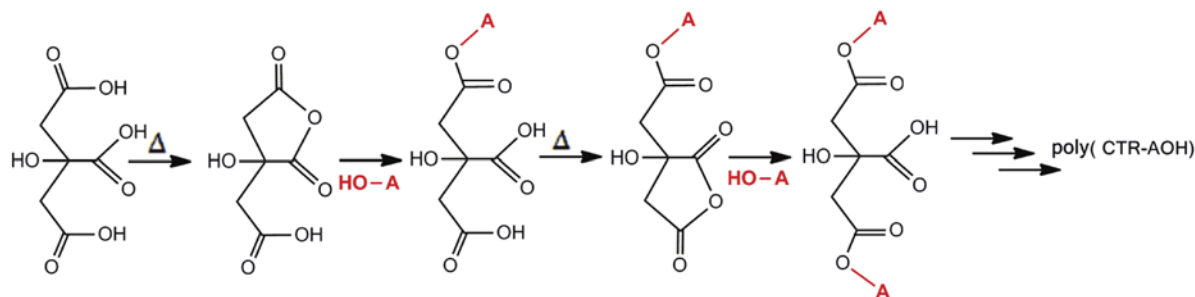

Figure 6. Scheme of intramolecular CTR anhydride formation and esterification between CTR and A-OH = PVOH
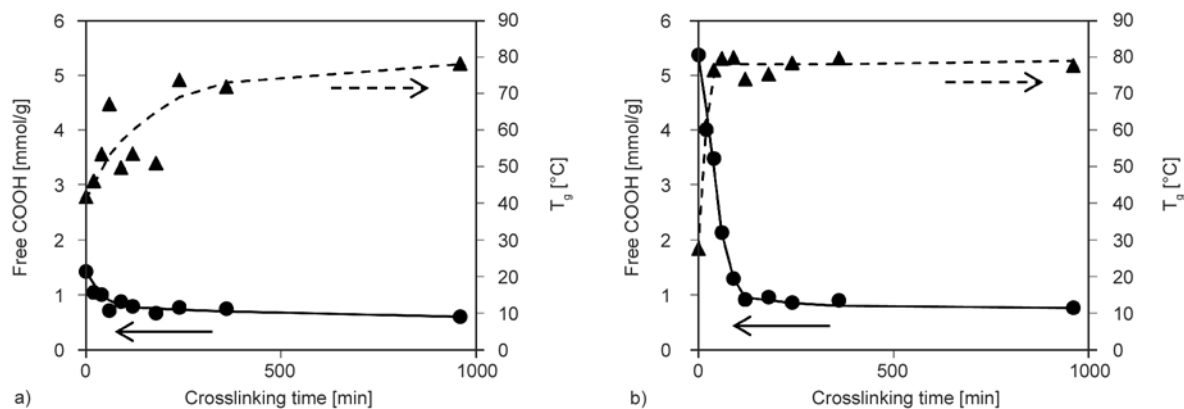
Figure 7. Free COOH groups and T_g of hydrated PVOH/CTR films as a function of crosslinking time for (a) PVOH/CTR 90/10 and (b) PVOH/CTR 60/40

first one may correspond to the grafting of CTR on PVOH chains. Then the spatial proximity between COOH functions already grafted allows the formation of anhydrides via an intermolecular mechanism and therefore additional post-esterification reaction involving chemical groups close to previous crosslinking points. This phenomenon has no major effect on T_g value neither on the global crosslinking degree but may result in a decrease of the heat capacity jump at T_g as previously mentioned.

3.3. Physical and mechanical characterization of PVOH/CTR films

It is interesting to check if some crystallinity is present in initial PVOH/CTR films and remains after crosslinking reaction. PVOH/CTR films exhibit a degradation phenomenon well below the melting point of PVOH (T_m = 185±5°C). Therefore, DSC cannot be used to highlight any melting peak in this case. So, X-ray diffractograms of PVOH/CTR films were recorded as a function of crosslinking time (Figure 8). Whatever the CTR content and crosslink-
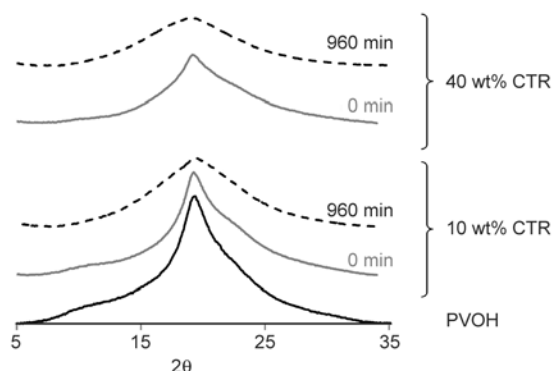
ing time, only one broad diffraction located at around $2\theta = 20°$ is observed without any evidence of crystalline peak which suggests that all samples are mainly in disordered state.

In Figure 9, typical DMA curves of three hydrated PVOH/CTR-90/10 films are shown: non crosslinked one and two crosslinked ones. An increase of the main relaxation temperatures with crosslinking time is observed, in good agreement with previous DSC results. As expected, the storage modulus E' increases with the heating time, below as well as above T_g, relevant to an increase of the crosslink density which rigidifies the polymer network. Additionally, one can notice the presence of two peaks in the $\tan\delta$ curves indicating various relaxations in the amorphous phase, even in the non crosslinked sample. This could suggest that the concentration of CTR is not homogeneous at local scale inside the sample.

The effect of crosslinking conditions on tensile behavior is illustrated on Figure 10. For the non-crosslinked films (t = 0 min), one can observe the
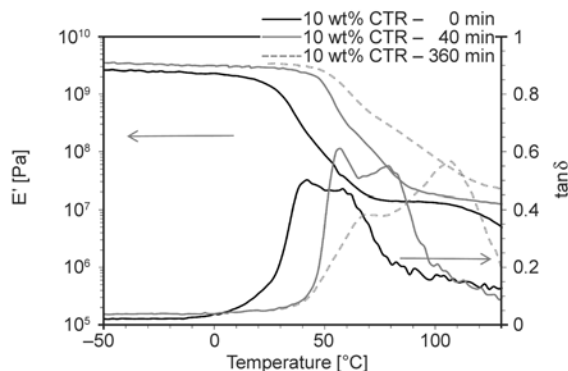

Figure 8. WAXS patterns of hydrated PVOH/CTR films for different crosslinking times

Figure 9. Dynamic mechanical response as a function of temperature of hydrated PVOH/CTR 90/10 films for different crosslinking times
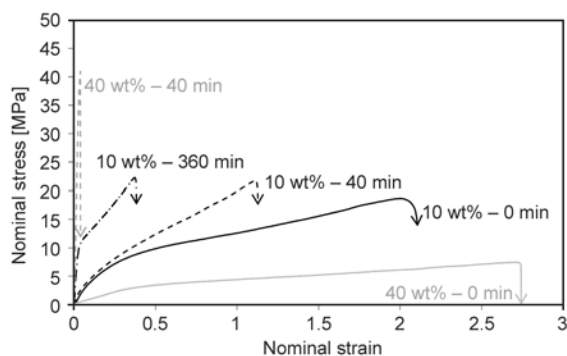
Figure 10. Nominal stress–strain curves of the PVOH/CTR films for different proportions of CTR and crosslinking times under uniaxial drawing at $T = 22°C$ at 58% R.H.

plasticizer effect of CTR indicated by an improvement of ductility as CTR concentration is increased. PVOH/CTR-60/40 samples exhibit a brittle behavior from 40 min curing, related to the highly crosslinking density preventing any plastic deformation. Owing to their brittleness, we decided to focus our attention only on the films containing 10% CTR.

All samples exhibit a homogeneous deformation. The stress level increases and the strain at break significantly decreases as the crosslinking time is increased. This behavior is related to the reduction of the chemical entanglement mass involving an enhancement of the rigidity and reduction of the limit of extensibility of chain segments between entanglements.

3.4. Influence of HPβCD on films properties with 10% of CTR

One of the main objectives of this study is to incorporate HPβCD in the polymer matrix. This cyclodextrin derivative would be used as a vector for prolonged release of a food preservative. As PVOH, HPβCD possesses OH functions which may react with COOH functions of CTR, allowing it to take part of the three-dimensional network. Because films with 40 wt% CTR are too brittle from 40 min of crosslinking, only films containing 10 wt% CTR are studied. Thus, the influence of the HPβCD addition on film properties was investigated on films containing 80 wt% PVOH, 10 wt% HPβCD and 10 wt% CTR using similar approach as previously. In that case, PVOH/HPβCD/CTR-80/10/10 and PVOH/CTR-90/10 cast solutions contain similar quantities of OH groups per gram.
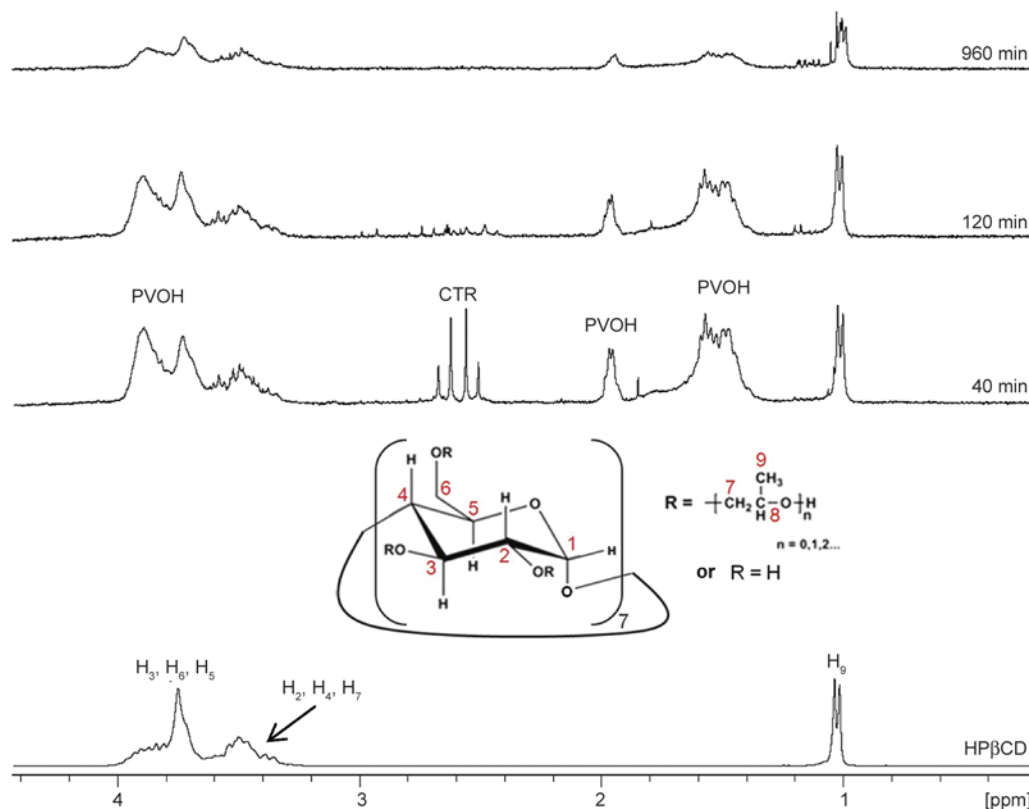

Figure 11. ¹H NMR spectra in D₂O of residual reagents of PVOH/CTR/HPβCD films with 10 wt% CTR and 10 wt% HPβCD for three crosslinking times

The ^{1}H NMR spectra of unreacted reagents obtained by solvent extraction for PVOH/HPβCD/CTR cross-linked films is presented on Figure 11. As previously, the intensity of the spectra has been magnified to reveal the low amounts of residual compounds. As observed for PVOH/CTR films (Figure 4), CTR is completely bound at 120 min, whereas PVOH and HPβCD are not completely bound even after 960 min. However the amounts of residual reagents are very low (<0.1%, determined by weight measurements).

The kinetics of the crosslinking reaction is evaluated following the free COOH content as a function of crosslinking time (Figure 12). Results show the same behavior as for PVOH/CTR films with 10 wt% CTR (Figure 7). COOH functions amount decreases with crosslinking time and reaches a quasi-plateau. The final amount of the free COOH groups is the same with or without HPβCD. The concentration of 10 wt% HPβCD does not modify the crosslinking kinetics.
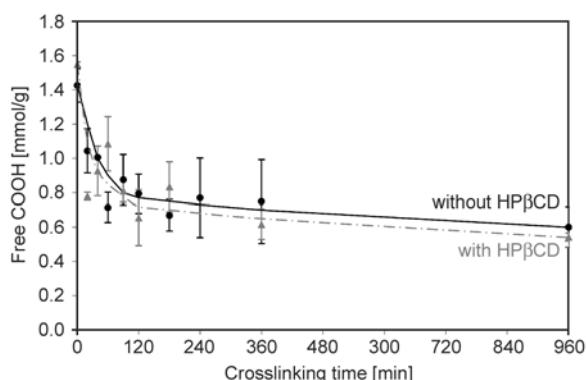

Figure 14. Strain at break at 22°C of PVOH/CTR and PVOH/HPβCD/CTR films, conditioned at 58% R.H., as a function of crosslinking time

It is also important to study the effect of HPβCD on film flexibility through T_g analysis (Figure 13). We notice no plasticizer effect of HPβCD on non-crosslinked films ($t = 0$ min). The incorporation of HPβCD in the polymer network seems to rigidify it. HPβCD is a bulky and rigid molecule. Its presence should decrease the global mobility of polymer chains.

Finally, drawing experiments were carried out and values of strain at break are reported on Figure 14. For all crosslinking times, the presence of HPβCD does not affect significantly the drawability of films. All samples present a ductile behavior.

4. Conclusions

Films based on PVOH and crosslinked with CTR, have been prepared in two steps by solvent casting method followed by heat treatment. Different characteristics of the films (chemical structure, T_g, crystallinity and tensile properties) were studied in relation to their formulation and the crosslinking time. Films with high content of CTR (40 wt%) are too brittle for the considered food application while films

Figure 12. Free COOH quantification of PVOH/CTR and PVOH/HPβCD/CTR films with 10 wt% CTR as a function of crosslinking time

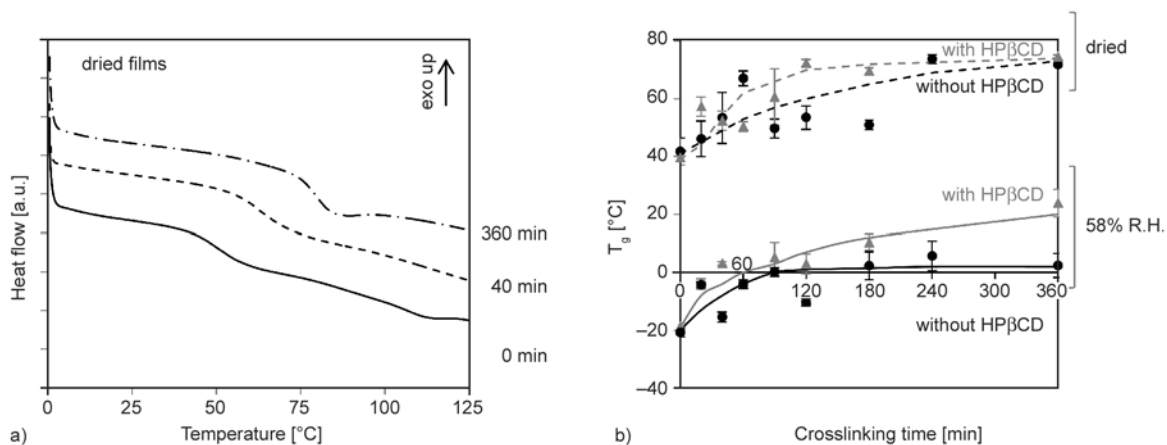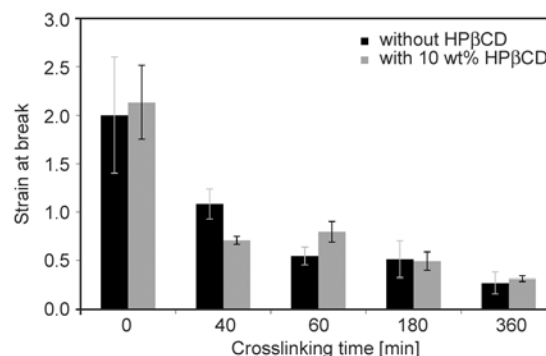**Figure 13.** (a) DSC profiles of PVOH/HPβCD/CTR films and (b) values of T_g as a function of crosslinking time with or without HPβCD

with low content of CTR (10 wt%) are transparent and show a ductile behavior. However, we highlighted that even after 960 min of crosslinking, a weak quantity of PVOH is not bound. We could expect that an intermediate formulation of PVOH and CTR could be more suitable for the targeted application. Moreover, during the crosslinking reaction, a part of COOH functions remains free. We could take advantage of these acid functions for further food storage. Finally, the incorporation of 10 wt% of cyclodextrin derivative as food additive carrier does not influence the characteristics of the films containing 10 wt% CTR. This formulation will be used for further studies.

References

[1] Finch C. A.: Polyvinyl alcohol development. Wiley, New York (1992).

[2] Imam S. H., Cinelli P., Gordon S. H., Chiellini E.: Characterization of biodegradable composite films prepared from blends of poly(vinyl alcohol), cornstarch, and lignocellulosic fiber. Journal of Polymers and the Environment, **13**, 47–55 (2005).
DOI: 10.1007/s10924-004-1215-6

[3] Conte A., Buonocore G. G., Sinigaglia M., Del Nobile M. A.: Development of immobilized lysozyme based active film. Journal of Food Engineering, **78**, 741–745 (2007).
DOI: 10.1016/j.jfoodeng.2005.11.013

[4] Hasimi A., Stavropoulou A., Papadokostaki K. G., Sanopoulou M.: Transport of water in polyvinyl alcohol films: Effect of thermal treatment and chemical crosslinking. European Polymer Journal, **44**, 4098–4107 (2008).
DOI: 10.1016/j.eurpolymj.2008.09.011

[5] Mansur H. S., Sadahira C. M., Souza A. N., Mansur A. A. P.: FTIR spectroscopy characterization of poly(vinyl alcohol) hydrogel with different hydrolysis degree and chemically crosslinked with glutaraldehyde. Materials Science and Engineering: C, **28**, 539–548 (2008).
DOI: 10.1016/j.msec.2007.10.088

[6] Shi R., Bi J., Zhang Z., Zhu A., Chen D., Zhou X., Zhang L., Tian W.: The effect of citric acid on the structural properties and cytotoxicity of the polyvinyl alcohol/starch films when molding at high temperature. Carbohydrate Polymers, **74**, 763–770 (2008).
DOI: 10.1016/j.carbpol.2008.04.045

[7] Wang S., Ren J., Li W., Sun R., Liu S.: Properties of polyvinyl alcohol/xylan composite films with citric acid. Carbohydrate Polymers, **103**, 94–99 (2014).
DOI: 10.1016/j.carbpol.2013.12.030

[8] Ajji Z.: Preparation of poly(vinyl alcohol) hydrogels containing citric or succinic acid using gamma radiation. Radiation Physics and Chemistry, **74**, 36–41 (2005).
DOI: 10.1016/j.radphyschem.2004.12.005

[9] Salt Y., Hasanoğlu A., Salt İ., Keleşer S., Özkan S., Dinçer S.: Pervaporation separation of ethylacetate–water mixtures through a crosslinked poly(vinylalcohol) membrane. Vacuum, **79**, 215–220 (2005).
DOI: 10.1016/j.vacuum.2005.03.010

[10] Martel B., Morcellet M., Ruffin D., Ducoroy L., Weltrowski M.: Finishing of polyester fabrics with cyclodextrins and polycarboxylic acids as crosslinking agents. Journal of Inclusion Phenomena and Macrocyclic Chemistry, **44**, 443–446 (2002).
DOI: 10.1023/A:1023080221850

[11] Martel B., Ruffin D., Weltrowski M., Lekchiri Y., Morcellet M.: Water-soluble polymers and gels from the polycondensation between cyclodextrins and poly(carboxylic acid)s: A study of the preparation parameters. Journal of Applied Polymer Science, **97**, 433–442 (2005).
DOI: 10.1002/app.21391

[12] Dainelli D., Gontard N., Spyropoulos D., Zondervan-van den Beuken E., Tobback P.: Active and intelligent food packaging: Legal aspects and safety concerns. Trends in Food Science and Technology, **19**, S103–S112 (2008).
DOI: 10.1016/j.tifs.2008.09.011

[13] Teixeira B. N., Ozdemir N., Hill L. E., Gomes C. L.: Synthesis and characterization of nano-encapsulated black pepper oleoresin using hydroxypropyl beta-cyclodextrin for antioxidant and antimicrobial applications. Journal of Food Science, **78**, 1913–1920 (2013).
DOI: 10.1111/1750-3841.12312

[14] Piercey M. J., Mazzanti G., Budge S. M., Delaquis P. J., Paulson A. T., Truelstrup Hansen L.: Antimicrobial activity of cyclodextrin entrapped allyl isothiocyanate in a model system and packaged fresh-cut onions. Food Microbiology, **30**, 213–218 (2012).
DOI: 10.1016/j.fm.2011.10.015

[15] Astray G., Gonzalez-Barreiro C., Mejuto J. C., Rial-Otero R., Simal-Gándara J.: A review on the use of cyclodextrins in foods. Food Hydrocolloids, **23**, 1631–1640 (2009).
DOI: 10.1016/j.foodhyd.2009.01.001

[16] Frömming K-H., Szejtli J.: Cyclodextrins in pharmacy. Springer, Dordrecht (1994).

[17] Council Direktrive 85/572/EEC D. Laying down the list of simulants to be used for testing migration of constituents of plastic materials and articles intended to come into contact with foodstuffs (1985).

[18] Fukae R., Yamamoto T., Fujita Y., Kawatsuki N., Sangen O., Kamachi M.: Poly(vinyl alcohol) with high diad-syndiotacticity and high melting point. Polymer Journal, **29**, 293–295 (1997).
DOI: 10.1295/polymj.29.293

[19] Wunderlich B.: Macromolecular Physics, Volume 1: Crystal structure, morphology, defects. Academic Press, New York (1973).

[20] Tubbs R. K.: Melting point and heat of fusion of poly (vinyl alcohol). Journal of Polymer Science Part A: General Papers, **3**, 4181–4189 (1965).
DOI: 10.1002/pol.1965.100031213

[21] Ducoroy L., Martel B., Bacquet M., Morcellet M.: Cation exchange finishing of nonwoven polyester with polycarboxylic acids and cyclodextrins. Journal of Applied Polymer Science, **103**, 3730–3738 (2007).
DOI: 10.1002/app.25249

[22] Darras O., Seguela R., Rietsch F.: Dried gels from linear low-density polyethylene: Morphology, thermal behavior, and mechanical properties. Journal of Polymer Science Part B: Polymer Physics, **30**, 349–359 (1992).
DOI: 10.1002/polb.1992.090300405

[23] Hodge R. M., Edward G. H., Simon G. P.: Water absorption and states of water in semicrystalline poly(vinyl alcohol) films. Polymer, **37**, 1371–1376 (1996).
DOI: 10.1016/0032-3861(96)81134-7

[24] Hoffman J. D.: Anelastic and dielectric effects in polymeric solids. Wiley, New York (1969).

[25] Nishio Y., Manley R. S. J.: Cellulose-poly(vinyl alcohol) blends prepared from solutions in N,N-dimethylacetamide-lithium chloride. Macromolecules, **21**, 1270–1277 (1988).
DOI: 10.1021/ma00183a016

[26] Lu Y., Yang C. Q.: Fabric yellowing caused by citric acid as a crosslinking agent for cotton. Textile Research Journal, **69**, 685–690 (1999).
DOI: 10.1177/004051759906900909

[27] Krumova M., López D., Benavente R., Mijangos C., Pereña J. M.: Effect of crosslinking on the mechanical and thermal properties of poly(vinyl alcohol). Polymer, **41**, 9265–9272 (2000).
DOI: 10.1016/S0032-3861(00)00287-1

Isocyanate toughening of pCBT/organoclay nanocomposites with exfoliated structure and enhanced mechanical properties

T. Abt[1*], *J. J. Bou*[2], *M. Sánchez-Soto*[1]

[1]Department of Materials Science. Centre Catalá del Plàstic. Universitat Politècnica de Catalunya, BarcelonaTech.
 C/Colom 114, 08222 Terrassa, Spain
[2]Department of Chemical Engineering, ETSEIB, Universitat Politècnica de Catalunya, BarcelonaTech, Diagonal 647,
 08028 Barcelona, Spain

Abstract. Cyclic butylene terephthalate (CBT®) is an interesting matrix material for the preparation of nanocomposites due to its very low, water-like melt viscosity which favours clay exfoliation. Nevertheless, polymerized CBT (pCBT) is inherently brittle. This paper reports the preparation of isocyanate-toughened nanocomposites made from CBT and organo-modified montmorillonite. The role of the organoclay as reinforcement and the polymeric isocyanate (PMDI) as toughening agent on the properties of pCBT was studied. The organoclay increased the stiffness and strength by up to 20% whereas the PMDI improved the deformation behaviour. However, the PMDI did not affect the degree of clay dispersion or exfoliation and flocculated-intercalated structures were observed. The compatibility between the pCBT matrix and clay was further increased by preparing PMDI-tethered intercalated organoclay. The modified organoclay then exfoliated during ring-opening polymerization and yielded true pCBT/clay nanocomposites. This work demonstrates that reactive chain extension of CBT with a polyfunctional isocyanate is an effective method to obtain toughened pCBT nanocomposites. Moreover, isocyanates can enhance the compatibility between pCBT and nanofiller as well as the degree of exfoliation.

Keywords: nanocomposites, cyclic butylene terephthalate, pCBT, toughening, clay exfoliation

1. Introduction

Currently, there are considerable efforts to obtain polymer nanocomposites based on organophilic layered silicates. The driving force of these efforts is the dramatic improvement in material properties such as stiffness and strength, flame resistance, gas barrier properties and thermal stability; however, toughness typically decreases with increasing organoclay content. These improvements can be obtained with very low organoclay contents, usually less than 5 wt%. Nevertheless, property improvements are only observed when intercalation, or better complete exfoliation, of the clay occurs and individual silicate layers disperse randomly and homogeneously on a nanoscale level in the polymer matrix. Otherwise, a flocculated-intercalated or even an immiscible structure due to poor physical interactions between the clay and the polymer matrix is usually obtained, leading to decreased mechanical and thermal performance. Therefore, exfoliated nanocomposites exhibit unique properties not shared by their micro- and macrocomposite counterparts [1–3]. The key to exfoliation is to match the polarity between the hydrophobic polymer and hydrophilic clay. A common way to increase compatibility is to render layered silicates organophilic by ion-exchange

reactions with cationic surfactants including primary, secondary, tertiary, and quaternary alkylammonium or alkylphosphonium cations. These surfactants lead to a larger interlayer spacing and a lower surface energy of the treated silicates, which improves polymer wetting and hence clay intercalation [3]. Moreover, some organic surfactants provide functional groups that can react with the polymer chains or initiate the polymerization of monomers, which in turn enhances the strength of the interface between clay surface and polymer [3, 4]. Despite the fact that the intercalation chemistry of polymers has been widely studied, clay exfoliation still remains a major challenge in the preparation of nanocomposites. This is partially due to the high melt viscosity of conventional thermoplastics. High melt viscosities can be overcome using ring-opening polymerization (ROP) of cyclic oligomers such as cyclic butylene terephthalate oligomers (CBT) which possess a very low, water-like melt viscosity (0.02 Pa·s at 190°C [5]). CBT oligomers undergo an entropically driven ROP in the presence of a tin-based catalyst at temperatures both above and below the melting temperature of polymerized CBT (referred to as pCBT), *i.e.* $T_m = 225°C$ [6]. This allows for isothermal processing below the T_m where crystallization and polymerization occur simultaneously, hence demoulding is possible without further cooling [7–9]. Nevertheless, pCBT is inherently brittle which has been ascribed to the formation of large perfect crystals with a lack of intercrystalline tie molecules [8], different crystalline morphologies [10] as well as to a low molecular weight [11, 12].

An increasing amount of publications dealing with pCBT/organoclay nanocomposites can be found in the literature [7, 13–21]; however, despite this considerable body of papers, little is known about the mechanical properties of these materials [15, 18, 20] and information about the deformation behaviour is rare. Most researchers employ the low viscosity of molten or dissolved oligomers in order to obtain a CBT-intercalated organoclay. Subsequent ROP causes an increase in interlayer distance along with the disintegration of the layered clay structure. Nevertheless, obtaining complete clay exfoliation is rather difficult [13], whereas intercalated structures and flocculated-intercalated structures are more commonly observed [15, 16, 18–21]. Although several researchers have shown that the organoclay was successfully intercalated with CBT oligomers or

even completely exfoliated prior to ROP, the silicate layers tended to reorganize due to the low viscosity of the molten CBT during ROP. Consequently, the exfoliated structure was lost and a flocculated-intercalated structure was obtained after polymerization [16, 19, 20].

Similarly, clay nanocomposites made from other types of cyclic oligomers have been reported. Huang *et al.* [22] reported the synthesis of partially exfoliated polycarbonate nanocomposites using carbonate cyclic oligomers and organoclay. They observed clay exfoliation after mixing the cyclic oligomers with the clay in a Brabender mixer for 1 h at 180°C. Subsequent ROP of the cyclics converted the matrix into linear polymer. Although no crystal features of the clay were observed in X-ray diffraction, TEM analysis revealed that partial exfoliation was obtained. González-Vidal *et al.* [23] synthesized nanocomposites of poly(hexamethylene terephthalate) (PHT) and organoclay *via* melt blending of PHT as well as by *in situ* ring-opening polymerization of hexamethylene terephthalate cyclic oligomers. Partially exfoliated structures were observed for samples prepared by melt blending whereas exclusively intercalated nanocomposites could be obtained by ROP. Lee *et al.* [17] polymerized cyclic ethylene terephthalate oligomers in the presence of an organoclay into poly(ethylene terephthalate) (PET)/clay nanocomposites. The oligomers were successfully intercalated into the clay galleries. Subsequent ROP yielded a PET matrix of high molecular weight where the clay was intercalated and partially exfoliated.

To hinder the reorganization of the silicate layers, clay platelets can be tethered to the polymer chains. Furthermore, clay-polymer coupling might enhance the exfoliation process and interfacial adhesion between the polymer matrix and clay surface. This was already effectively demonstrated for polyurethanes; coupling reactions of organoclay surfactants with isocyanates [4, 24–26] or with polyols [27, 28] have been employed in the synthesis of thermoplastic polyurethane nanocomposites, resulting in exfoliation and increased mechanical properties.

The method described herein involves a coupling reaction of the hydroxyl groups of the organic surfactants with $-N=C=O$ functional groups of a polyfunctional isocyanate in order to intercalate the organoclay. Since the tethered isocyanate is also highly reactive toward the pCBT functional groups,

specifically toward carboxyl end groups as shown in [11], pCBT is expected to be grafted onto the isocyanate-modified organoclay. To the best of our knowledge, this has not been reported in literature to date.

2. Experimental Section
2.1. Materials
Cyclic butylene terephthalate oligomers combined with a catalyst (butyl tin chloride dihydroxide) were used in this work. The material was provided as granules by Cyclics Europe GmbH (Schwarzheide, Germany). The CBT was ground into a fine powder using a mortar and pestle and vacuum dried at 80°C for 8 h prior to processing. If not otherwise stated, one-component CBT oligomers (CBT160®) were used. For one sample two-component CBT oligomers (CBT100®) were used for melt blending. For initiation of the ROP, 0.45 wt% of Fascat® 4105 (with respect to CBT) was added to the molten oligomers. A polymeric methylene diphenyl diisocyanate, PMDI, was used for chemical modification of the organoclay as well as to toughen the pCBT nanocomposites. It was purchased from BASF Poliuretanos Iberia S.A. (Rubí, Spain) and was used as received. The PMDI was a brown, viscous liquid of grade IsoPMDI 92410. It was composed from 4,4″-methylenebis(phenyl isocyanate) and contained oligomers with an average functionality of ~2.7 and a NCO content of 31.8%.

A commercial montmorillonite modified with a quaternary ammonium salt (*i.e.* methyl, tallow, bis-2-hydroxyethyl, quaternary ammonium), namely Cloisite® 30B (referred to as Cl30B, Southern Clay Products, Inc., Gonzales, TX, USA) was chosen for reinforcement because the organic surfactant bears two hydroxyl groups which is a requirement for isocyanate coupling. Moreover, it was shown that this type of organoclay is compatible with poly(butylene terephthalate) (PBT) and capable of intercalation due to polar interactions between the PBT carboxyl groups and the surfactant hydroxyl groups [29, 30]. Additionally, this type was the preferred one in patent literature [14]. The organoclay was characterized by a density of 1.98 g/cm^3, a moisture content of <3% and a typical dry particle size d_{50} of <10 μm. The interlaminar distance d_{001} was 1.85 nm which was confirmed by other researchers [29, 30]. The organoclay was vacuum dried at 80°C for 12 h and stored in a desiccator over silica gel.

Analytical grade tetrahydrofuran (referred to as THF, purity = 99.5%; water content = 0.05%) was purchased from Panreac Química S.A. (Barcelona, Spain) and was used as received.

2.2. Organoclay modification
Cl30B was modified with PMDI as follows. A 500 mL flat bottom flask equipped with a Liebig condenser was charged with 200 mL THF and heated up to the boiling point. Five grams of organoclay and five grams of PMDI were added to the boiling THF under a constant stirring rate of 300 min^{-1} and under a stream of nitrogen gas. A relatively large PMDI excess of 150% was used in order to account for a possible reaction of PMDI with unbound or chemically bound water of the organoclay [31]. The reaction conditions were maintained for 8 h. The solution was then allowed to cool to room temperature and was filtered through a paper filter. The filtrate was washed thoroughly three times with fresh THF in order to remove unreacted isocyanate and was then vacuum dried at 60°C for 24 h and stored in a desiccator over silica gel. The isocyanate-grafted organoclay was referred to as PMDI-*g*-Cl30B.

2.3. Sample preparation
Two processing routes, melt blending (MB) and solvent blending (SB), were employed to prepare pCBT/Cl30B nanocomposites. The studied clay content was 1, 2 and 3 wt%. Two different groups of samples were prepared using each processing route, namely CBT/PMDI/Cl30B ternary blends (each containing 1 wt% of PMDI) and CBT/PMDI-*g*-Cl30B binary blends.

Melt blending was conducted in a lab-scale batch mixer (Brabender Plasti-Corder W50EHT, Brabender GmbH & Co. KG, Duisburg, Germany), equipped with a torque measuring system. Approximately 40 g of previously dried CBT and the corresponding amount of either organoclay or chain extender and organoclay were in situ polymerized in the batch mixer at a temperature of 230°C for 15 min, a rotor speed of 60 min^{-1} and under a protective nitrogen blanket. The materials were then collected from the mixing chamber, ground into granules, vacuum dried for 8 h at 80°C and subsequently compression moulded at a temperature of 250°C and a pressure of 4 MPa for 5 min in order to obtain flat samples for testing. Compression moulding was performed in an IQAP LAP PL-15 hot plate press equipped with

temperature- and pressure-controlled plates (IQAP Masterbatch group SL, Barcelona, Spain). The cooling rate of the cold stage of the hot plate press was previously determined to be approximately –50°C/min.

Solvent blending was used to homogeneously disperse either the organoclay or chain extender and organoclay in CBT prior to ROP. It was performed with approximately 20 g of CBT and organoclay dry blend in 50 mL THF at room temperature at a stirring speed of 300 min^{-1} for 1 h. The dispersions were then vacuum dried at 80°C for 8 h, ground into a fine powder using a mortar and pestle and again vacuum dried again at 80°C for at least 3 days to completely remove the THF. Approximately 13 g of the dried blends were in situ polymerized at a temperature of 230°C for 15 min during compression moulding in the previously mentioned hot plate press. All prepared films from both processing routes had dimensions of ca. 150×150×0.5 mm^3 and were used to extract samples for further characterization. In addition, pristine pCBT specimens were also prepared by both processing routes for comparison.

In addition to the previously mentioned groups of samples, another sample was prepared as follows. A ternary blend of two-component CBT100 (*i.e.* oligomers without catalyst), 1 wt% of PMDI and 3 wt% of Cl30B was melt blended at 200°C, 180 min^{-1} and N$_2$ atmosphere for 2 h. The temperature was then raised to 230°C, the rotor speed was reduced to 60 min^{-1} and the transesterification catalyst was added in order to initiate the ROP. The blend was allowed to polymerize for 15 min. This sample was referred to as pCBT100/PMDI/Cl30B 96/1/3. The purpose of this method was to take advantage of the low viscosity of the molten CBT oligomers in such way that they would swell the organoclay by diffusing into the clay galleries, causing exfoliation of the clay particles upon polymerization, as demonstrated by other researchers [13, 16]. Processing details of all prepared samples are compiled in Table 1.

2.4. Characterization

Isocyanate grafting onto the clay platelets was verified using FT-IR analysis. Infrared spectra were recorded on a Nicolet 6700 FT-IR/Attenuated Total Reflection spectrometer (Thermo Fisher Scientific, Waltham, MA, USA). Spectra were obtained in the wavenumber interval between 4000 and 400 cm^{-1} at a scan number of 32 scans and a resolution of 4 cm^{-1}. The degree of clay exfoliation was determined using X-ray diffraction (XRD) and transmission electron microscopy (TEM). XRD diffraction data was collected on a Bruker D4 Endeavor using Ni-filtered Cu K$_\alpha$ radiation ($\lambda = 1.54$ Å, $V = 40$ kV; $I = 40$ mA). XRD scattering patterns were recorded in the diffraction angle (2θ) range of $1.5° < 2\theta < 10°$ at a scanning rate of 8 s/step using steps of 0.02°. TEM analysis was performed on a Jeol JEM2011 transmission electron microscope (Jeol, Tokyo, Japan) using an acceleration voltage of 200 kV. Thin (60–100 nm) specimens were prepared at room temperature using an ultramicrotome (Leica EM UC6, Leica Microsystems GmbH, Wetzlar, Germany). The samples were further characterized using differential scanning calorimetry (DSC) on a Perkin-Elmer Pyris 1 device calibrated with indium. DSC was carried out under dry nitrogen atmosphere using a sample weight of 8–12 mg. Samples were heated from 30 to 250°C at a heating rate of 10°C/min, followed by an isothermal step of 3 minutes and then

Table 1. Overview over produced pCBT/organoclay nanocomposites

Sample designation	Processing	Temperature [°C]	Time [min]
pCBT/PMDI/Cl30B 98/1/1-MB	MB	230+250*	15+5*
pCBT/PMDI/Cl30B 98/1/1-SB	SB	230	15
pCBT/PMDI-*g*-Cl30B 1%-MB	MB	230+250*	15+5*
pCBT/PMDI-*g*-Cl30B 2%-MB	MB	230+250*	15+5*
pCBT/PMDI-*g*-Cl30B 3%-MB	MB	230+250*	15+5*
pCBT/PMDI-*g*-Cl30B 1%-SB	SB	230	15
pCBT/PMDI-*g*-Cl30B 2%-SB	SB	230	15
pCBT/PMDI-*g*-Cl30B 3%-SB	SB	230	15
pCBT100/PMDI/Cl30B 96/1/3-MB	MB	200+230+250	120+15+5

MB: melt blending; SB: solvent blending
*A temperature of 230+250°C and a time of 15+5 min indicate that the material was melt blended at 230°C for 15 min and then compression moulded at 250°C for 5 min.

cooled from 250 to 30°C at a rate of –10°C/min. The second heating run was performed in the same temperature range and at a heating rate of 10°C/min. The melting enthalpy, ΔH_m, of the first heating run was used to calculate the degree of crystallinity, X_C, of the samples according to Equation (1):

$$X_C = \frac{\Delta H_m}{\Delta H_m^0 (1 - W_f)} \cdot 100\%$$ (1)

where ΔH_m is the measured melting enthalpy, ΔH_m^0 is the melting enthalpy for a fully perfect crystalline PBT which is found in literature to be 142 J/g [8] and W_f is the weight fraction of the clay reinforcement. The nanocomposites were characterized by dynamic mechanical thermal analysis (DMTA) using a Q800 TA device (TA Instruments, New Castle, DE, USA) in tensile mode at a frequency of 1 Hz and a strain of 0.05%. The temperature range was set from 30 to 210°C at a heating rate of 2°C/min and samples had dimensions of ca. $27 \times 5 \times 0.5$ mm^3. The relative viscosity, η_{rel}, of samples dissolved in 1,1,1,3,3,3-hexafluoroisopropanol (referred to as HFIP, Apollo Scientific, Manchester, UK) at a concentration of 10 mg/mL was determined using a Cannon-Ubbelohde viscometer (Cannon Instrument Co., Pennsylvania, USA) operated at 25±0.1°C in a water bath. Three measurements were carried out for each reported value. Gel permeation chromatography (GPC) was performed on an Agilent Technologies 1200 Series modular system (Agilent Technologies, Santa Clara, CA, USA) which was comprised of an Agilent 1260 variable wavelength detector operated at a temperature of 35°C. A PL HFIPgel column from Agilent was used to perform separation. Mobile phase was HFIP stabilized with 2.72 g/L sodium fluoroacetate to prevent polyelectrolyte effect. A flow rate of 1.0 mL/min was employed. The pressure of the column was 75 bars. The injection volume was 100 µL of 1 mg/mL polymer solution. Low dispersed poly(methyl methacrylate) samples were used as internal standards. Molar mass data were calculated using Agilent Chemstation software. The mechanical properties were determined by tensile tests according to ISO 527 at room temperature and at a crosshead speed of 10 mm/min on a Galdabini Sun 2500 universal testing machine (Galdabini, Cardano al Campo, Italy), equipped with a video extensometer to measure strain. Type 1BA specimens were extracted from the above described sample films. A minimum of five specimens were tested for each reported value.

3. Results and discussion
3.1. PMDI/organoclay grafting
A grafting reaction between PMDI and the hydroxyl groups of the quaternary ammonium salt of the organoclay is proposed in Figure 1.

FT-IR spectra of pristine and PMDI-grafted Cl30B in Figure 2 exhibit the characteristic bands of montmorillonite due to Al–O stretching at 3630, 919, 850 and 624 cm^{-1}, Si–O stretching at 1048 cm^{-1}, and asymmetric and symmetric stretching of methylene groups in hydrocarbon chains of the quaternary ammonium salt at 2852 and 2925 cm^{-1}, respectively [4, 32, 33]. It can be seen that PMDI-grafted organoclay exhibited new absorption bands at wavenumbers of 1716 and 1536 cm^{-1} (*c.f.* insert in Figure 2) which were attributed to the stretching and deformation vibration of hydrogen bonded C=O and N–H, respectively [4, 34]. These absorption bands are characteristic of a urethane group, suggesting that PMDI had reacted with the quaternary ammonium salt of the organoclay.

Further evidence of a successful isocyanate grafting onto the clay surface is provided by XRD analysis; the diffraction patterns of pristine Cl30B and PMDI-*g*-Cl30B are illustrated in Figure 3. As mentioned in section 2.1, pristine Cl30B has a basal spacing of 1.85 nm according to the literature. The Cl30B used in this work exhibited a reflection at $2\theta = 5.2°$ which corresponds to a slightly lower basal spacing, namely 1.7 nm, most likely due to some agglomeration [3].

In contrast, the diffraction pattern of PMDI-*g*-Cl30B shows two reflections at $2\theta = 3.0$ and $6.4°$ which correspond to basal spacings of 2.9 and 1.4 nm, respectively. The reflection at $2\theta = 6.4°$ can be ascribed to the second diffraction order. This suggests that the PMDI intercalated into the clay galleries and was grafted onto the platelet surface. Consequently, the interlayer distance between clay galleries markedly increased and thus a weakening of the interlayer interactions with facilitated exfoliation during processing can be expected.

3.2. Optimization of processing parameters
In previous literature it was reported that the presence of organoclay can delay the ROP of CBT,
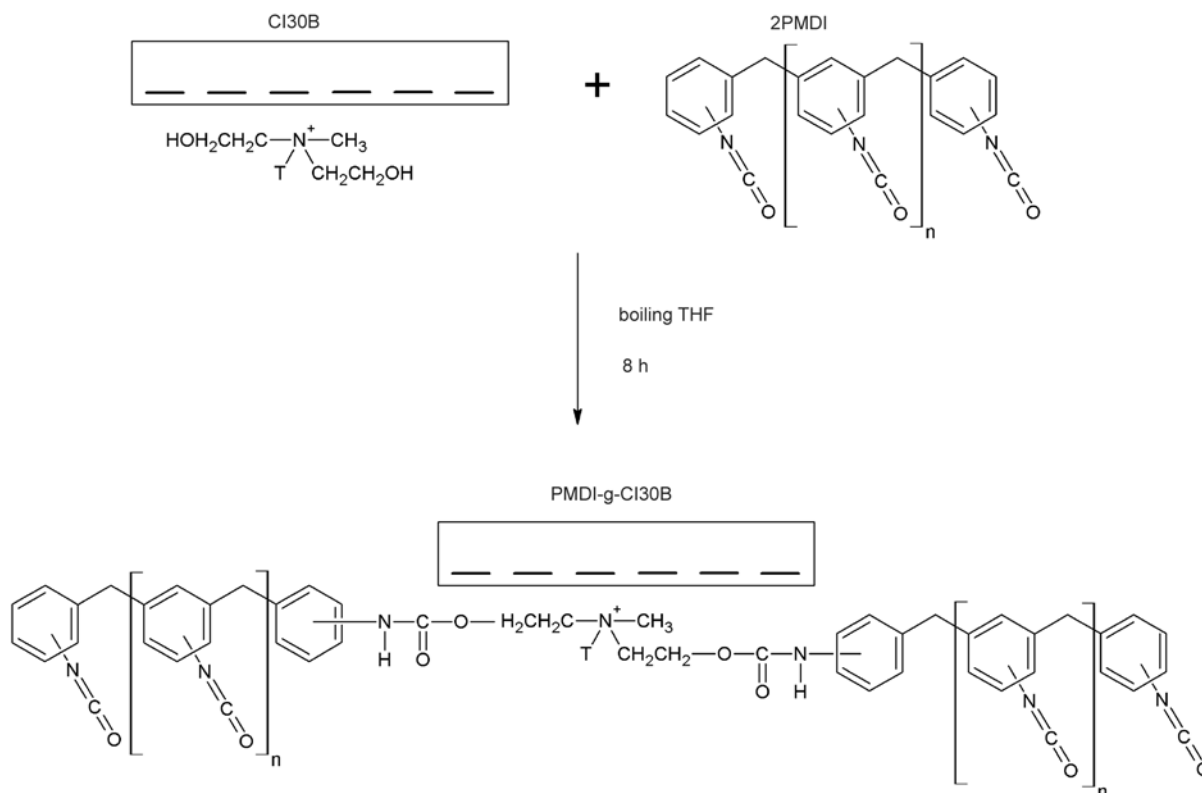
Figure 1. Chemical modification of Cl30B with PMDI. T is tallow (~65% C18; ~30% C16; ~5% C14).
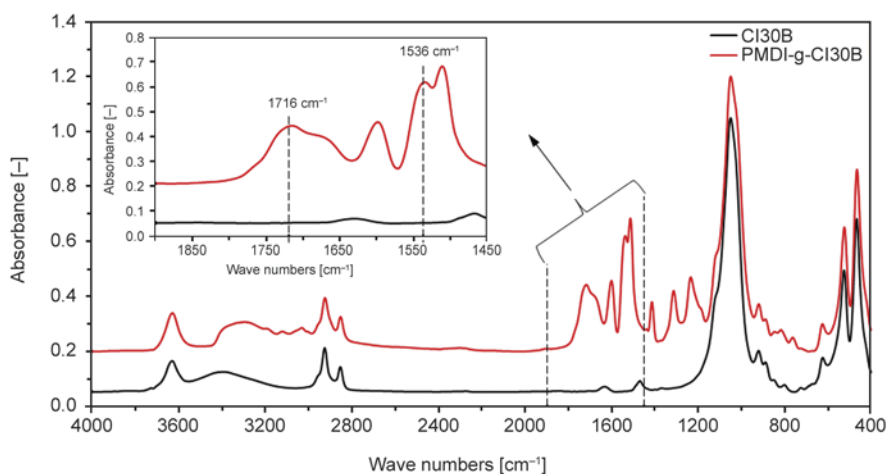

Figure 2. FT-IR spectra of unmodified Cl30B and PMDI-*g*-Cl30B in the wavenumber range 4000–400 cm^{-1} with inset in the wavenumber range 1900–1450 cm^{-1}

shifting the polymerization towards higher temperatures and affecting the conversion and molecular weight of the resulting pCBT [7, 16]. Therefore, prior to sample preparation, the optimum processing parameters were determined in order to achieve a fully converted high-molecular weight pCBT. This was achieved using preliminary torque versus time measurements in the batch mixer. In addition, a binary CBT/Cl30B blend containing 1 wt% of clay was prepared for comparison. Figure 4 depicts the torque curves of pristine CBT and a CBT blend of

each sample group with an organoclay content of 1 wt%.
The torque signal of pristine CBT was first detected after 3 min which was considered to be the onset of the ROP. Before this time, the melt viscosity of the molten CBT was below the detection limit of the measuring system. The torque curve reached a plateau after 9 min at ca. 6 Nm. It then slowly increased until it reached a maximum of 7 Nm after 30 min. The CBT/Cl30B blend showed a 3 min delayed torque onset and an overall lower torque
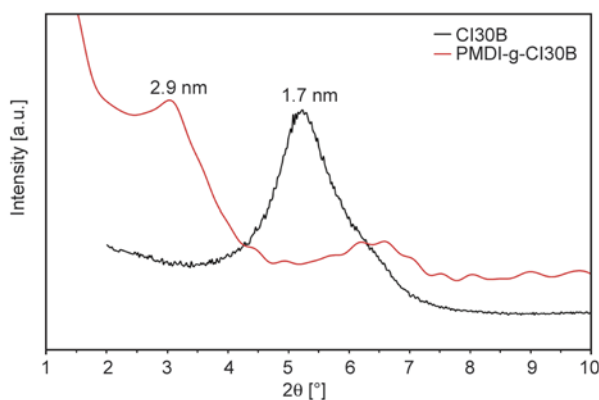
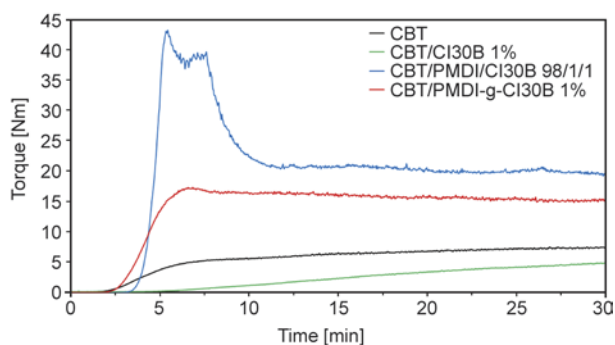**Figure 3.** XRD diffraction patterns of pristine Cl30B and PMDI-*g*-Cl30B

Figure 4. Torque versus time plots of CBT, CBT/Cl30B 1%, CBT/PMDI/Cl30B 98/1/1 and CBT/PMDI-*g*-Cl30B 1% blends polymerized at 230°C and 60 min^{-1} under nitrogen atmosphere

level relative to pristine CBT. This data confirms previous literature [7, 16] that the organoclay delays the ROP and affects the final molecular weight. A possible explanation is that bound crystal water of the clay may have affected the CBT catalyst activity [35] and also caused pCBT hydrolysis.

In comparison, the ternary blend exhibited less delay in the torque onset, reaching a maximum level of 43 Nm after 5 min due to the fast reaction between PMDI and growing pCBT chains [11]. The torque decreased and reached a stable plateau value of 20 Nm which is considerably higher than that of neat CBT, suggesting a relatively higher molecular

weight. Similarly, the CBT/PMDI-*g*-Cl30B blend showed a torque onset equal to pristine CBT, a maximum torque of 17 Nm after 7 min and essentially maintained this torque level until the end of the experiment.

On one hand, this demonstrates the reactivity of PMDI-*g*-Cl30B since no extra isocyanate was added, indicating that the organoclay modification was effective. It also shows that the addition of PMDI to CBT/Cl30B blends, as well as the addition of PMDI-grafted Cl30B to CBT, enhances the polymerization onset time and apparently the final molecular weight. It is noteworthy that the molten pCBT/PMDI-*g*-Cl30B blend was completely transparent after a 30 min mixing time, indicating clay exfoliation, whereas the pCBT/Cl30B blends were somewhat hazy, which became more noticeable when PMDI was present in the ternary blends. In light of the observed torque maxima, a polymerization time of 15 min was chosen for the ternary blends as well as for the binary blends containing PMDI-*g*-Cl30B.

3.3. Relative viscosity and GPC analysis

Relative viscosity measurements in combination with GPC data were used to estimate the molecular weights of some samples (*c.f.* Table 2). It is noteworthy that all samples were filtered prior to GPC analysis which was not the case for relative viscosity determination. Therefore, η$_{rel}$ values represent the samples in their entirety whereas GPC data only accounts for the soluble portion of the blend. In order to distinguish the influence of 'free' isocyanate in ternary blends in interaction with the organoclay on the molecular weight of pCBT, the melt blended sample pCBT/PMDI 1% is also listed in Table 2.

As mentioned in section 3.2, the presence of organoclay can delay the ROP of CBT and affect the conversion and molecular weight of the resulting pCBT. This effect can also be observed here when

Table 2. Relative viscosity and GPC data of pCBT/organoclay nanocomposites

Sample designation	Viscosity, η$_{rel}$ [–]	GPC		
		M_n [kg/mol]	M_w [kg/mol]	PDI [–]
pCBT-MB	2.33	28.7	62.4	2.2
pCBT/PMDI 1%*	3.86	41.1	137.6	3.3
pCBT/Cl30B 1%-MB	2.55	24.9	61.5	2.5
pCBT/PMDI/Cl30B 98/1/1-MB	3.26	31.9	100.3	3.1
pCBT/PMDI-*g*-Cl30B 1%-MB	2.43	28.8	68.1	2.4
pCBT/PMDI-*g*-Cl30B 1%-SB	2.60	30.8	75.0	2.4

*Gel content: 31.5%

comparing pristine pCBT-MB and pCBT/Cl30B 1%-MB. The latter sample exhibited a relatively lower molecular weight but also a higher viscosity. Therefore, this higher viscosity may be solely ascribed to the presence of the organoclay.

It can be seen that the addition of 1 wt% of PMDI to pCBT considerably increased both viscosity and molecular weight of the pCBT. Moreover, this composition resulted in a gel content of 31.5% [11] which is indicative of successful chain extension. A similar, though less pronounced, increase in η_{rel}, M_n and M_w was found for the ternary blend. In contrast, binary blends with PMDI-grafted organoclay showed little improvement in both viscosity and molecular weight. This can be explained by the fact that no 'free' isocyanate was present in these samples and only a small amount of PMDI grafted to the clay platelets was available for chain extension. Nevertheless, binary blends with PMDI-*g*-Cl30B showed a slight increase in molecular weight as compared to pCBT/Cl30B 1%-MB.

The polydispersity index (PDI) of pCBT was close to the theoretical PDI of 2.0, typical for ring-opening polymerizations [6, 36]. The PDI increased with increasing degree of chain extension. As such, the highest PDI values were found for samples with 'free' isocyanate, *i.e*. pCBT/PMDI 1% and pCBT/PMDI/Cl30B 98/1/1-MB. This demonstrates that PMDI and PMDI-*g*-Cl30B improve the molecular weight of pCBT/Cl30B nanocomposites.

3.4. XRD analysis

The degree of exfoliation of the various pCBT/organoclay composites was studied using XRD analysis; the diffraction patterns are illustrated in Figures 5 and 6.
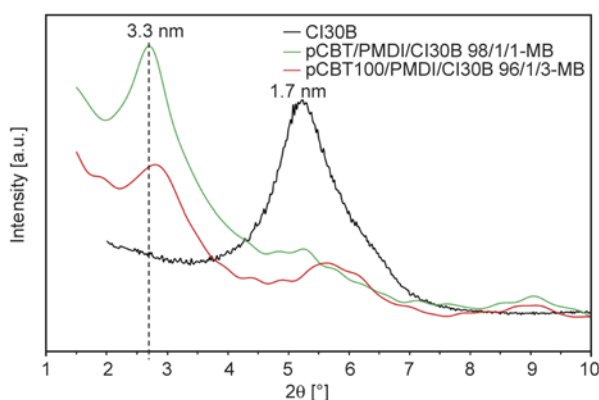
The diffraction patterns of the two pCBT nanocomposites in Figure 5 are quite similar to each other but different from the one of pristine Cl30B. They show two reflections at $2\theta = 2.7°$ and $5.2–5.4°$ which correspond to basal spacings of 3.3 nm and 1.7–1.64 nm. The first reflection suggests that most of the organoclay was intercalated by pCBT, whereas the reflection at higher diffraction angles again can be attributed to the second diffraction order. Overall, an intercalated-flocculated structure can be deduced [3]. The weak peak around $2\theta = 9°$ is the (001) reflection of pCBT and is also present in WAXS diffraction patterns, as seen for instance in [8]. These samples represent two groups; pCBT/PMDI/Cl30B ternary blends and the sample pCBT100/PMDI/Cl30B 96/1/3 which was melt blended for 2 h in order to swell the organoclay prior to ROP. Moreover, these samples also represent the studied organoclay content range. It can be concluded that within the studied range melt blending produces an intercalated-flocculated nanocomposite structure, regardless of clay content. The presence of PMDI or swelling the organoclay in molten low-viscous CBT oligomers apparently did not affect the basal spacing.

The diffraction patterns of PMDI-grafted organoclay and the corresponding melt blended and solvent blended nanocomposites are depicted in Figure 6. No reflections can be observed in the melt blended sample, suggesting that the organoclay was largely exfoliated and true nanocomposites were formed. The weak reflection around $2\theta = 6°$ in the solvent blended sample suggests that part of the clay was agglomerated. Nevertheless, the peak intensity is very low; indicating that an insignificant amount of agglomeration was present, probably due
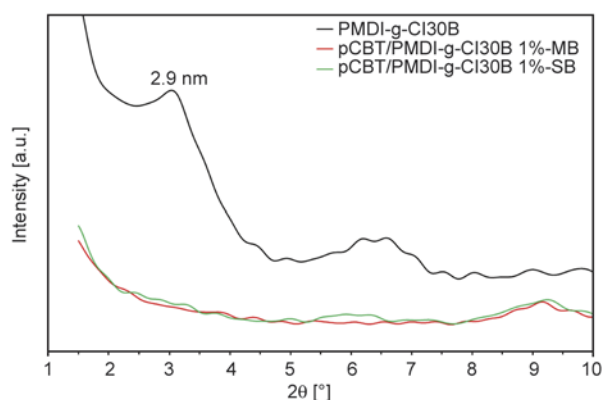

Figure 5. XRD diffraction patterns of Cl30B and the corresponding melt blended pCBT nanocomposites

Figure 6. XRD diffraction patterns of PMDI-*g*-Cl30B and the corresponding melt blended and solvent blended pCBT nanocomposites

to clay platelet reorganization during ROP in the absence of shear flow. Again, the weak reflection around $2\theta = 9°$ originates from pCBT, as previously mentioned.

These results suggest that the PMDI-grafted organoclay was able to be largely exfoliated and randomly dispersed in the pCBT matrix because the clay was previously intercalated with PMDI. Moreover, because PMDI was grafted onto the organoclay surface it is very likely that pCBT end groups reacted with the PMDI and therefore facilitated clay exfoliation.

3.5. TEM analysis

The TEM micrographs of ternary blends and PMDI-grafted binary blends are depicted in Figure 7. The effect of the clay modification is best observed at a larger scale when comparing Figures 7a and 7c, whereas Figures 7b and 7d represent high magnification details of the two samples. It can be noticed that ternary blends (*c.f.* Figure 7a and 7b) exhibited micron-sized clay tactoids, confirming an intercalated-flocculated structure. Nevertheless, a partial clay intercalation with increased *d* spacing is apparent in Figure 7b for this sample.
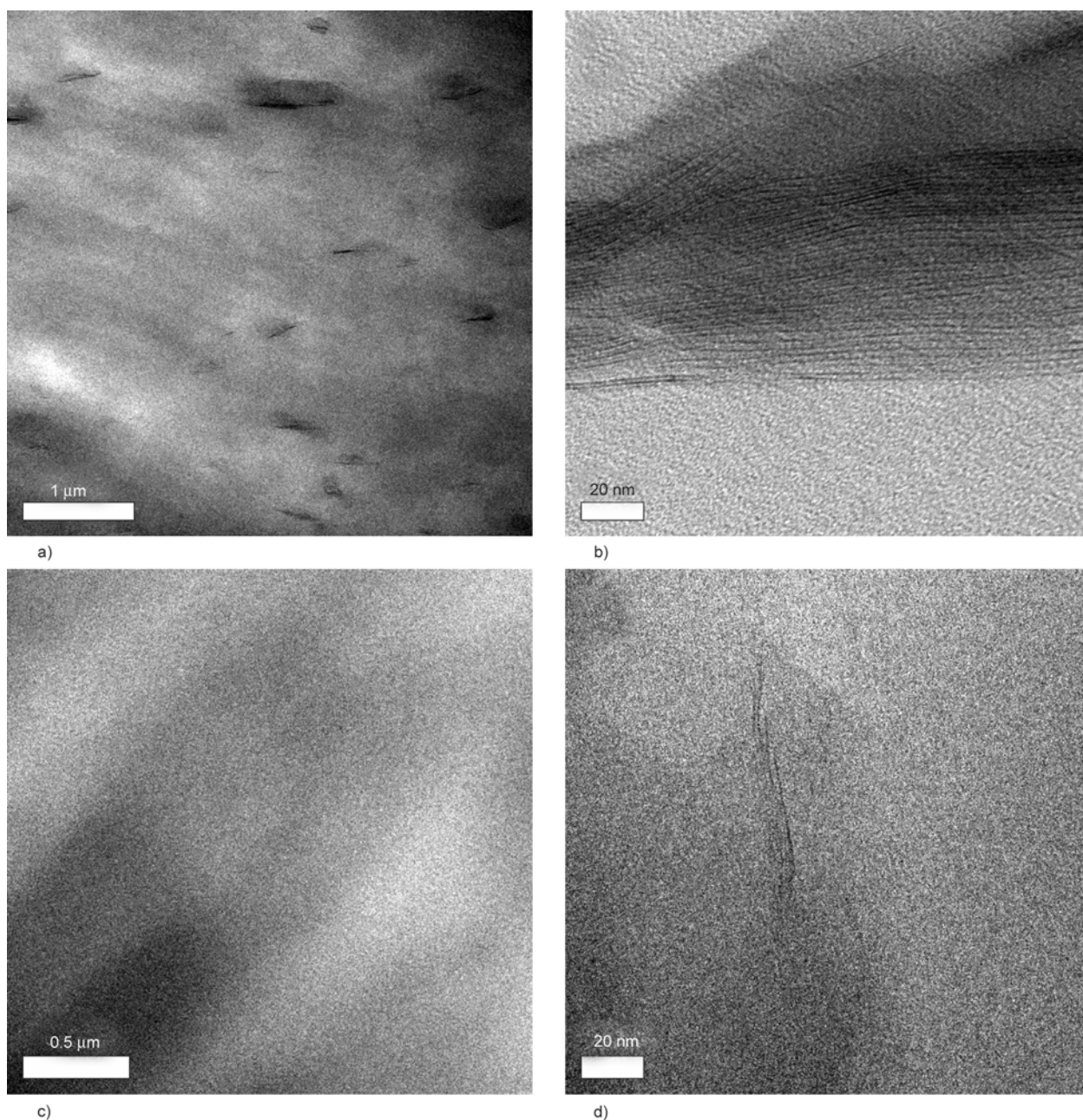

Figure 7. TEM micrographs of melt blended pCBT/PMDI/Cl30B 98/1/1 (a) and (b), and pCBT/PMDI-*g*-Cl30B 1% (c) and (d)

On the other hand, pCBT/PMDI-*g*-Cl30B 1%-MB in Figure 7c did not exhibit any sign of clay agglomeration. This sample exhibited a largely exfoliated structure as confirmed by XRD analysis, although some small stacks of a few clay platelets can be seen at high magnification in Figure 7d. Therefore, the chemical modification of organoclay is a useful method to achieve clay exfoliation.

3.6. DSC analysis

The 'as moulded' thermal properties of melt blended and solvent blended pCBT/organoclay nanocomposites are collected in Table 3. Since the processing routes used slightly alter the thermal properties, both melt blended and solvent blended pristine pCBT are shown as reference in the table so that the nanocomposites could be compared to their respective host polymer, depending on the processing route.

The first heating scans of melt blended and solvent blended pCBT/PMDI-*g*-Cl30B are shown in Figure 8a and 8b, respectively. As expected, no significant difference between melt and solvent blended binary blends was found due to equal thermal histories (melt crystallized at ca. –50°C/min in the cold stage of the hot plate press). All samples exhibited a small amount of cold crystallization in the range of 200–210°C with a crystallization enthalpy of –1 to –2 J/g. Moreover, all samples showed a pronounced low-temperature melting peak in the temperature range of 222–224°C and a high-temperature shoulder around 228°C. The latter was ascribed to the recrystallization phenomenon [7]. As can be seen from the graphs, melting temperatures as well as melting enthalpies of the nanocomposites slightly decreased with clay content, which is in agreement with published data [7, 16]. The resulting range of crystallinity was 27–36%. One may expect a relatively tougher behaviour for samples with lower crystal fraction. This was indeed the case for ternary blends, as will be shown later. Nevertheless, the binary samples with low clay loading exhibited a crystal fraction similar to their respective host polymer but showed a considerably higher toughness. This indicates that the degree of crystallinity cannot be solely responsible for the pCBT brittleness.

Table 3. 'As moulded' thermal properties of melt and solvent blended samples, heating and cooling at 10°C/min

| Sample	First heating		First cooling	
	T_m [°C]	ΔH_m [J/g]	T_c [°C]	χ_c [%]
pCBT-MB	224.2	51.3	193.1	36.1
pCBT-SB	221.6	45.3	187.2	31.9
pCBT/PMDI/Cl30B 98/1/1-MB	221.3	37.8	190.9	26.6
pCBT/PMDI/Cl30B 98/1/1-SB	220.5	37.7	188.2	26.5
pCBT/PMDI-*g*-Cl30B 1%-MB	222.4	47.4	193.5	33.4
pCBT/PMDI-*g*-Cl30B 2%-MB	221.5	47.0	192.4	33.1
pCBT/PMDI-*g*-Cl30B 3%-MB	221.9	46.2	193.2	32.5
pCBT/PMDI-*g*-Cl30B 1%-SB	221.4	46.7	190.7	32.9
pCBT/PMDI-*g*-Cl30B 2%-SB	220.9	44.0	190.4	31.0
pCBT/PMDI-*g*-Cl30B 3%-SB	220.9	39.4	189.7	27.7
pCBT100/PMDI/Cl30B 96/1/3-MB	221.6	39.2	193.4	27.6
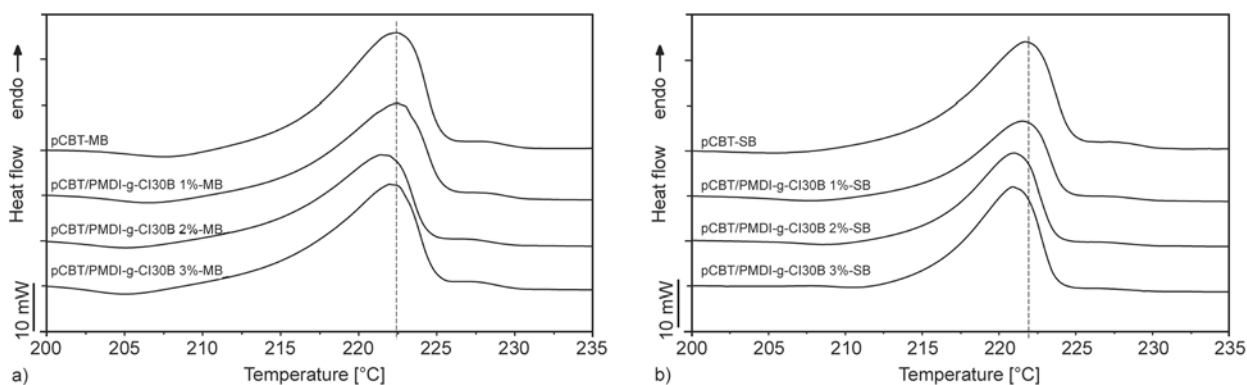
Figure 8. DSC first heating scan of pCBT and pCBT/PMDI-*g*-Cl30B prepared by (a) melt blending and (b) solvent blending; heating and cooling rate of 10°C/min

Although the clay slightly acts as a nucleation agent, it most likely also confines the polymer chain segments and thus hinders the segmental rearrangement during crystallization and restricts the formation of perfect crystals in the polymer matrix [37]. The enthalpy decrease is more prominent in the ternary blends which can be partially attributed to the effect of chain extension when PMDI was present in the blend (*c.f.* Table 3).

It was shown that the organoclay used suppresses the cold crystallization when the CBT/Cl30B blend was polymerized in a DSC apparatus during the first heating scan. However, pCBT/Cl30B blends [7, 16] as well as PBT/Cl30B blends [29] exhibited a nucleation effect during melt crystallization. This was also found for solvent blended pCBT/PMDI-*g*-Cl30B blends (ΔT = 3–4°C). When the latter were melt blended, no nucleation effect was observed. Ternary pCBT/PMDI/Cl30B blends did not show a clear tendency due to an antagonistic effect of clay-induced nucleation and PMDI-induced reduction of T_c [11]. In light of the 6°C difference in pCBT crystallization temperature, due to different processing routes or the addition of 1 wt% of PMDI, the observed nucleation effect (ΔT = 3–4°C) is not relevant. This also becomes apparent when considering the fact that Cl30B was reported to increase T_c by 12–18°C in conventional PBT [29].

3.7. DMTA analysis

The dynamic mechanical properties of pCBT/organoclay nanocomposites were determined; the dynamic storage modulus curves as a function of temperature are shown in Figure 9. It should be noted that PMDI-grafted pCBT is more flexible than pCBT [11]. Therefore, the nanocomposites were compared
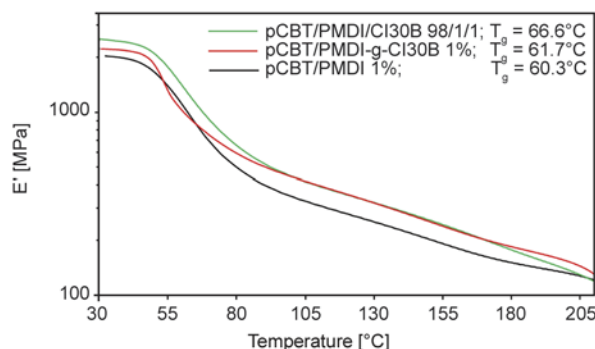

Figure 9. DMTA storage moduli versus temperature of melt blended pCBT/PMDI 1%, pCBT/PMDI/Cl30B 98/1/1 and pCBT/PMDI-*g*-Cl30B 1% nanocomposites

to melt blended pCBT/PMDI 1% instead of pCBT to account for this decreased stiffness.

The nanocomposites exhibited an enhanced stiffness both in the glassy and in the rubbery state as compared to the unreinforced sample. The nanocomposites exhibited a similar thermo-mechanical performance, although pCBT/PMDI/Cl30B ternary blend showed a slightly better performance as compared to the binary blend in the range of the glass transition. The clay modification resulted in a relative stiffness decrease in the glassy state as compared to the ternary blend. Nevertheless, pCBT/PMDI-*g*-Cl30B showed a reinforcing effect similar to that of the ternary blend in the rubbery state.

3.8. Tensile properties

The tensile properties of the prepared nanocomposites, of neat pCBT-MB and of pCBT-SB are compiled in Table 4 for comparison. It should be noted that pristine pCBT is inherently brittle, irrespective of the different processing routes used herein.

Table 4. Tensile properties of pCBT/organoclay nanocomposites

Sample	Tensile modulus [GPa]	Tensile strength [MPa]	Elongation at break [%]
pCBT-MB	2.9±0.3	60±2	8±1
pCBT-SB	3.0±0.2	63±4	9±2
pCBT/PMDI/Cl30B 98/1/1-MB	3.0±0.4	58±1	81±77
pCBT/PMDI/Cl30B 98/1/1-SB	3.7±0.5	62±2	20±15
pCBT/PMDI-*g*-Cl30B 1%-MB	3.2±0.4	61±3	15±13
pCBT/PMDI-*g*-Cl30B 2%-MB	3.2±0.2	63±2	9±3
pCBT/PMDI-*g*-Cl30B 3%-MB	3.3±0.2	66±1	7±1
pCBT/PMDI-*g*-Cl30B 1%-SB	3.0±0.2	58±1	56±21
pCBT/PMDI-*g*-Cl30B 2%-SB	2.6±0.1	53±1	21±9
pCBT/PMDI-*g*-Cl30B 3%-SB	2.4±0.2	50±6	4±2
pCBT100/PMDI/Cl30B 96/1/3-MB	3.2±0.2	66±1	16±10

As expected, pCBT/PMDI/Cl30B ternary blends exhibited a semi-ductile deformation behaviour with yielding and unstable necking (also indicated by the large standard deviation of the elongation at break in Table 4) along with a stiffness and strength similar to that of pristine pCBT. The solvent blended sample showed a 23% higher stiffness as well as a moderately increased toughness.

Similarly, melt blended pCBT/PMDI-*g*-Cl30B nanocomposites showed increasing modulus and strength but also decreasing toughness with PMDI-*g*-Cl30B loading. Stiffness and strength were ca. 10% higher for a clay loading of 3 wt% as compared to the reference. Contrary to these mechanical properties, solvent blending had a negative effect; the mechanical properties markedly decreased with clay loading. At present it is difficult to explain why solvent blending degrades the mechanical properties. A possible explanation might be clay segregation during the compression moulding step due to the low viscosity of molten CBT prior to ROP and the absence of shear flow during/after polymerization. On the other hand, decreased mechanical properties could be related to THF. THF may have partially remained in the CBT blends after solvent blending, which can be explained by the fact that its chemical structure is similar to the one of the diol-derived portion in pCBT. It was shown that THF can lead to a pCBT with increased ductility but decreased stiffness and strength [38]. Finally, the sample pCBT100/PMDI/Cl30B 96/1/3-MB showed a stiffness and strength increase of ca. 10%, respectively, whereas failure strain increased by 100%.

The mechanical properties of the herein prepared samples were compared to literature values from conventional PBT/Cl30B blends and also from pCBT/organoclay composites. In case of PBT nanocomposites, a clay loading of 3 wt% resulted in 23–39% stiffness increase, 6–24% strength increase and 58–98% decrease in failure strain [18, 29]. Regarding pCBT nanocomposites, Wan *et al*. [20] used 2 wt% of clay loading and found an increase in stiffness and strength of 13 %, respectively, while failure strain was not reported. Hong and co-workers [15] showed that the strength of pCBT/Cl30B 1% nanocomposites increased by 13%, while a content of 3 wt% resulted in only 2% strength improvement. However, stiffness increased by ca. 10% when the organoclay content was 3 wt%. No information on failure strain

of the pCBT nanocomposites is available but it can be assumed that they were brittle due to the above mentioned pCBT brittleness. Regarding PBT nanocomposites, it is clear that already 1 wt% of clay loading leads to severe embrittlement with a failure strain below 5% of the otherwise ductile PBT [18, 29].

The herein reported increase in stiffness and strength is slightly lower as compared to the one described in literature for both pCBT and PBT blends. This is due to the lower stiffness of chain extended pCBT [11]. On the other hand, a semi-ductile behaviour was observed in most of our nanocomposites due to the toughening effect of the isocyanate, either as additive in ternary blends or grafted onto the clay platelets. This demonstrates that the mechanical properties of pCBT/Cl30B nanocomposites can be tailored in a fairly wide range from high stiffness and strength to moderate toughness by adding PMDI or using the proposed clay modification.

4. Conclusions

Organically modified montmorillonite was used to prepare isocyanate-toughened pCBT nanocomposites *via* melt and solvent blending. The organoclay was further modified by tethering the isocyanate to the clay surfactant in order to improve matrix compatibility. Ternary blends of pCBT/PMDI/Cl30B showed an intercalated-flocculated structure which resulted in a higher toughness, but also led to a stiffness and strength similar to that of neat pCBT due to an antagonistic effect of organoclay reinforcement and isocyanate toughening. The organoclay modification with isocyanate resulted in an increased interlaminar distance. When this isocyanate-grafted organoclay was reacted with pCBT, clay exfoliation and random dispersion occurred in the pCBT matrix during polymerization. Thermal properties and stabilities were not significantly altered by the organoclay, although some nanocomposites showed a decreased degree of crystallinity. It was demonstrated that the mechanical properties of these nanocomposites can be tailored from high stiffness and strength to moderate toughness using PMDI and the proposed clay modification.

References

[1] Alexandre M., Dubois P.: Polymer-layered silicate nanocomposites: Preparation, properties and uses of a new class of materials. Materials Science and Engineering R: Reports, **28**, 1–63 (2000).
DOI: 10.1016/S0927-796X(00)00012-7

[2] Kiliaris P., Papaspyrides C. D.: Polymer/layered silicate (clay) nanocomposites: An overview of flame retardancy. Progress in Polymer Science, **35**, 902–958 (2010).
DOI: 10.1016/j.progpolymsci.2010.03.001

[3] Sinha Ray S., Okamoto M.: Polymer/layered silicate nanocomposites: A review from preparation to processing. Progress in Polymer Science, **28**, 1539–1641 (2003).
DOI: 10.1016/j.progpolymsci.2003.08.002

[4] Pattanayak A., Jana S. C.: Synthesis of thermoplastic polyurethane nanocomposites of reactive nanoclay by bulk polymerization methods. Polymer, **46**, 3275–3288 (2005).
DOI: 10.1016/j.polymer.2005.02.081

[5] Mohd Ishak Z. A., Gatos K. G., Karger-Kocsis J.: On the *in-situ* polymerization of cyclic butylene terephthalate oligomers: DSC and rheological studies. Polymer Engineering and Science **46**, 743–750 (2006).
DOI: 10.1002/pen.20486

[6] Brunelle D. J., Bradt J. E., Serth-Guzzo J., Takekoshi T., Evans T. L., Pearce E. J., Wilson P. R.: Semicrystalline polymers *via* ring-opening polymerization: Preparation and polymerization of alkylene phthalate cyclic oligomers. Macromolecules, **31**, 4782–4790 (1998).
DOI: 10.1021/ma971491j

[7] Karger-Kocsis J., Shang P. P., Mohd Ishak Z. A., Rösch M.: Melting and crystallization of *in-situ* polymerized cyclic butylene terephthalates with and without organoclay: A modulated DSC study. Express Polymer Letters, **1**, 60–68 (2007).
DOI: 10.3144/expresspolymlett.2007.12

[8] Parton H., Baets J., Lipnik P., Goderis B., Devaux J., Verpoest I.: Properties of poly(butylene terephthatlate) polymerized from cyclic oligomers and its composites. Polymer, **46**, 9871–9880 (2005).
DOI: 10.1016/j.polymer.2005.07.082

[9] Wunderlich B.: Crystallization during polymerization. Angewandte Chemie International Edition in English, **7**, 912–919 (1968).
DOI: 10.1002/anie.196809121

[10] Yu T., Wu C. M., Chang C. Y., Wang C. Y., Rwei S. P.: Effects of crystalline morphologies on the mechanical properties of carbon fiber reinforcing polymerized cyclic butylene terephthalate composites. Express Polymer Letters, **6**, 318–328 (2012).
DOI: 10.3144/expresspolymlett.2012.35

[11] Abt T., Martínez de Ilarduya A., Bou J. J., Sánchez-Soto M.: Isocyanate toughened pCBT: Reactive blending and tensile properties. Express Polymer Letters, **7**, 172–185 (2013).
DOI: 10.3144/expresspolymlett.2013.16

[12] Abt T., Sánchez-Soto M., Martínez de Ilarduya A.: Toughening of *in situ* polymerized cyclic butylene terephthalate by chain extension with a bifunctional epoxy resin. European Polymer Journal, **48**, 163–171 (2012).
DOI: 10.1016/j.eurpolymj.2011.10.017

[13] Berti C., Binassi E., Colonna M., Fiorini M., Zuccheri T., Karanam S., Brunelle D. J.: Improved dispersion of clay platelets in poly(butylene terephthalate) nanocomposite by ring-opening polymerization of cyclic oligomers: Effect of the processing conditions and comparison with nanocomposites obtained by melt intercalation. Journal of Applied Polymer Science, **114**, 3211–3217 (2009).
DOI: 10.1002/app.30957

[14] Dion R., Bank D., Beebe M., Walia P., LeBaron P., Oelberg J., Barger M., Paquette M., Read M.: Polymerized macrocyclic oligomer nanocomposite compositions. U.S. Patent 20050059768A1, USA (2005).

[15] Hong Y., Yoon H., Lim S.: Preparation of PBT/clay nanocomposites using supercritical process. International Journal of Precision Engineering and Manufacturing, **10**, 115–118 (2009).
DOI: 10.1007/s12541-009-0055-7

[16] Lanciano G., Greco A., Maffezzoli A., Mascia L.: Effects of thermal history in the ring opening polymerization of CBT and its mixtures with montmorillonite on the crystallization of the resulting poly(butylene terephthalate). Thermochimica Acta, **493**, 61–67 (2009).
DOI: 10.1016/j.tca.2009.04.004

[17] Lee S-S., Ma Y. T., Rhee H-W., Kim J.: Exfoliation of layered silicate facilitated by ring-opening reaction of cyclic oligomers in PET–clay nanocomposites. Polymer, **46**, 2201–2210 (2005).
DOI: 10.1016/j.polymer.2005.01.006

[18] McLauchlin A., Bao X., Zhao F.: Organoclay polybutylene terephthalate nanocomposites using dual surfactant modified montmorillonite prepared by the masterbatch method. Applied Clay Science, **53**, 749–753 (2011).
DOI: 10.1016/j.clay.2011.07.006

[19] Tripathy A. R., Burgaz E., Kukureka S. N., MacKnight W. J.: Poly(butylene terephthalate) nanocomposites prepared by *in-situ* polymerization. Macromolecules, **36**, 8593–8595 (2003).
DOI: 10.1021/ma021364+

[20] Wan C., Zhao F., Bao X., Kandasubramanian B., Duggan M.: Surface characteristics of polyhedral oligomeric silsesquioxane modified clay and its application in polymerization of macrocyclic polyester oligomers. The Journal of Physical Chemistry B, **112**, 11915–11922 (2008).
DOI: 10.1021/jp805259q

[21] Wu F. M., Yang G. S.: Poly(butylene terephthalate)/organoclay nanocomposites prepared by *in-situ* bulk polymerization with cyclic poly(butylene terephthalate). Materials Letters, **63**, 1686–1688 (2009).
DOI: 10.1016/j.matlet.2009.05.011

[22] Huang X., Lewis S., Brittain W. J., Vaia R. A.: Synthesis of polycarbonate-layered silicate nanocomposites *via* cyclic oligomers. Macromolecules, **33**, 2000–2004 (2000).
DOI: 10.1021/ma991709x

[23] González-Vidal N., Muñoz-Guerra S., Martínez de Ilarduya A., Benali S., Peeterbroeck S., Dubois P.: Poly(hexamethylene terephthalate)–layered silicate nanocomposites. European Polymer Journal, **46**, 156–164 (2010).
DOI: 10.1016/j.eurpolymj.2009.10.018

[24] Cao X., James Lee L., Widya T., Macosko C.: Polyurethane/clay nanocomposites foams: Processing, structure and properties. Polymer, **46**, 775–783 (2005).
DOI: 10.1016/j.polymer.2004.11.028

[25] Wang H-H., Chen K-V.: A novel synthesis of reactive nano-clay polyurethane and its physical and dyeing properties. Journal of Applied Polymer Science, **105**, 1581–1590 (2007).
DOI: 10.1002/app.25955

[26] Xu Z-B., Kong W-W., Zhou M-X., Peng M.: Effect of surface modification of montmorillonite on the properties of rigid polyurethane foam composites. Chinese Journal of Polymer Science, **28**, 615–624 (2010).
DOI: 10.1007/s10118-010-9111-0

[27] Esposito Corcione C., Prinari P., Cannoletta D., Mensitieri G., Maffezzoli A.: Synthesis and characterization of clay-nanocomposite solvent-based polyurethane adhesives. International Journal of Adhesion and Adhesives, **28**, 91–100 (2008).
DOI: 10.1016/j.ijadhadh.2006.12.004

[28] Indennidate L., Cannoletta D., Lionetto F., Greco A., Maffezzoli A.: Nanofilled polyols for viscoelastic polyurethane foams. Polymer International, **59**, 486–491 (2010).
DOI: 10.1002/pi.2726

[29] Chang Y-W., Kim S., Kyung Y.: Poly(butylene terephthalate)–clay nanocomposites prepared by melt intercalation: Morphology and thermomechanical properties. Polymer International, **54**, 348–353 (2005).
DOI: 10.1002/pi.1686

[30] Li X., Kang T., Cho W-J., Lee J-K., Ha C-S.: Preparation and characterization of poly(butyleneterephthalate)/organoclay nanocomposites. Macromolecular Rapid Communications, **22**, 1306–1312 (2001).
DOI: 10.1002/1521-3927(20011101)22:16<1306::aid-marc1306>3.0.co;2-i

[31] Kim Y., White J. L.: Formation of polymer nanocomposites with various organoclays. Journal of Applied Polymer Science, **96**, 1888–1896 (2005).
DOI: 10.1002/app.21581

[32] Berti C., Fiorini M., Sisti L.: Synthesis of poly(butylene terephtahlate) nanocomposites using anionic clays. European Polymer Journal, **45**, 70–78 (2009).
DOI: 10.1016/j.eurpolymj.2008.09.039

[33] Xiao J., Hu Y., Wang Z., Tang Y., Chen Z., Fan W.: Preparation and characterization of poly(butylene terephthalate) nanocomposites from thermally stable organic-modified montmorillonite. European Polymer Journal, **41**, 1030–1035 (2005).
DOI: 10.1016/j.eurpolymj.2004.11.025

[34] Yin L., Shi D., Liu Y., Yin J.: Toughening effects of poly(butylene terephthalate) with blocked isocyanate-functionalized poly(ethylene octene). Polymer International, **58**, 919–926 (2009).
DOI: 10.1002/pi.2613

[35] Brunelle D. J.: Cyclic oligomer chemistry. Journal of Polymer Science Part A: Polymer Chemistry, **46**, 1151–1164 (2008).
DOI: 10.1002/pola.22526

[36] Hall A. J., Hodge P.: Recent research on the synthesis and applications of cyclic oligomers. Reactive and Functional Polymers, **41**, 133–139 (1999).
DOI: 10.1016/S1381-5148(99)00036-X

[37] Pavlidou S., Papaspyrides C. D.: A review on polymer–layered silicate nanocomposites. Progress in Polymer Science, **33**, 1119–1198 (2008).
DOI: 10.1016/j.progpolymsci.2008.07.008

[38] Abt T., Sánchez-Soto M., Illescas S., Aurrekoetxea J., Sarrionandia M.: Toughening of in situ polymerized cyclic butylene terephthalate by addition of tetrahydrofuran. Polymer International, **60**, 549–556 (2011).
DOI: 10.1002/pi.2977